High-refractive index particles in counter-propagating optical tweezers — manipulation and forces —

High-refractive index particles in counter-propagating optical tweezers
— manipulation and forces —
Astrid van der Horst, Ph. D. thesis Utrecht University, September 2006
ISBN-10: 90-393-4346-2
ISBN-13: 978-90-393-4346-3

A digital version of this thesis can be downloaded from *www.amolf.nl* and from *www.colloid.nl*. Printed copies can by obtained by request via e-mail to *library@amolf.nl* or by addressing the library at the FOM Institute for Atomic and Molecular Physics (AMOLF), Kruislaan 407, 1098 SJ Amsterdam, The Netherlands.

High-refractive index particles in counter-propagating optical tweezers — manipulation and forces —

Hoge-brekingsindex deeltjes in een optisch pincet van twee kanten — manipulatie en krachten —

(met een samenvatting in het Nederlands)

Proefschrift

ter verkrijging van de graad van doctor aan de Universiteit Utrecht op gezag van de rector magnificus, prof. dr. W. H. Gispen, in gevolge het besluit van het college voor promoties in het openbaar te verdedigen op maandag 25 september 2006 des middags te 2.30 uur

door

Astrid van der Horst

geboren op 30 maart 1972 te Amsterdam

Promotoren: Prof. dr. A. van Blaaderen
Prof. dr. M. Dogterom

Dit werk werd mede mogelijk gemaakt door financiële steun van de Stichting voor Fundamenteel Onderzoek der Materie (FOM) en de Nederlandse organisatie voor Wetenschappelijk Onderzoek (NWO).

“ I’ve come a long way
I’ve come a long way
I’ve gone 500 miles today ”

— Michelle Shocked —

CONTENTS

1. Introduction 1
1.1 General introduction 2
1.2 Theory of optical trapping 3
1.2.1 Force measurements 7
1.3 High forces in biophysics 7
1.4 Optical tweezers in colloid and interface science 8
1.5 This thesis 9

2. Optical tweezers setup for independent 3D manipulation and imaging 13
2.1 Introduction 14
2.2 Experimental setup and details 16
2.2.1 Arrays of tweezers in more than one plane using one objective 19
2.2.2 Imaging modes 20
2.2.3 Quadrant photodiode position detection 21
2.2.4 Colloidal dispersions 21
2.3 Dynamic arrays of optical tweezers 23
2.4 Optical trapping and decoupled confocal imaging 25
2.5 Arrays of tweezers in more than one plane using one objective . . 26
2.6 Manipulation of (core-shell) particles in a concentrated dispersion 27
2.7 Counter-propagating tweezers 29
2.8 Discussion and outlook 30

3. Spherical aberrations due to refractive-index mismatch 37
3.1 Introduction 38
3.2 Spherical aberrations 39
3.2.1 Spherical aberrations and 3D confocal imaging 43
3.2.2 Spherical aberrations and optical trapping 43
3.3 Experimental setup and methods 44
3.4 Results and discussion 47
3.5 Conclusions 51
3.6 Outlook 52

4. Improving the accuracy of long-range patterning of colloidal particles . 57
4.1 Introduction 58
4.2 Experimental setup and methods 58
4.2.1 Feedback control of the piezo stage 60

4.2.2 Colloidal dispersions . . . 61
4.2.3 Image analysis . . . 62
4.3 Results and discussion . . . 62
4.3.1 Patterning with feedback control . . . 64
4.4 Conclusions and outlook . . . 67

5. High-refractive index particles in dynamic counter-propagating optical tweezers . . . 71
5.1 Introduction . . . 72
5.2 Experimental methods . . . 73
5.2.1 Experimental setup . . . 73
5.2.2 Creating dynamic arrays of counter-propagating tweezers 73
5.2.3 Sample cell . . . 73
5.3 Results and discussion . . . 74
5.4 Conclusion and outlook . . . 76

6. Three-dimensional trapping and manipulation of high-refractive index nanorods . . . 81
6.1 Introduction . . . 82
6.2 Experimental setup and details . . . 82
6.2.1 Optical tweezers setup . . . 82
6.2.2 Rod dispersions and sample cells . . . 83
6.3 Results and discussion . . . 84
6.4 Conclusions and outlook . . . 86
6.5 Appendix — Reduced axial trap stiffness in line tweezers . . . 89

7. Optical tweezers setup for force measurements in counter-propagating traps . . . 97
7.1 Introduction . . . 98
7.2 Force measurements with quadrant photodiode position detection 99
7.2.1 Trap stiffness κ . . . 99
7.2.2 Quadrant photodiode measurements . . . 100
7.2.3 Detector sensitivity β . . . 100
7.3 Experimental setup and methods . . . 101
7.3.1 Counter-propagating optical tweezers setup . . . 101
7.3.2 Quadrant photodiode position detection using a second laser beam . . . 103
7.4 Results and discussion . . . 104
7.5 Conclusions and outlook . . . 110

8. Forces exerted on high-index particles in counter-propagating optical tweezers . . . 115
8.1 Introduction . . . 116
8.2 Experimental setup and methods . . . 117
8.2.1 Calculation of forces in optical tweezers . . . 117
8.2.2 Experimental setup . . . 119
8.2.3 Colloidal dispersions . . . 120

8.3 Results and discussion 120
8.3.1 Refractive-index dependence of the trap stiffness 120
8.3.2 Size dependence of the trap stiffness 123
8.3.3 Trap alignment dependence of the trap stiffness 124
8.3.4 Numerical aperture dependence of the trap stiffness . . . 126
8.4 Conclusions and outlook 128
8.5 Appendix — Determining the parameters γ and ω_0 130

Summary 137

Samenvatting 139

Dankwoord 143

Curriculum vitae 145

List of publications 146

1. INTRODUCTION

The concept of being able to grab onto a particle with light, and manipulate it in three dimensions, is very exciting. In recent years, the exploration of the possibilities of optical tweezers in the fields of (bio-)physics, chemistry and colloid physics, has only added to that excitement. The applications are numerous, as both manipulation of dielectric and metal particles, and force measurements employing them, have been demonstrated. Possibilities seem endless, but there are of course also some limitations. In this introductory Chapter, we will shed light on the optical forces involved in trapping, and will show that high-refractive index particles cannot be trapped in a single-beam gradient trap. In addition, the forces that can be applied using a single beam are currently limited to ∼100 pN. By using counter-propagating beams in which the destabilizing scattering forces are cancelled, high-refractive index particles can be confined. We take a look at how the trapping of these high-index particles can extend the possibilities in the fields of biophysics, to exert higher forces, and colloid physics, to pattern surfaces. We will end with an overview of what can be expected in the remainder of this thesis.

1.1 General introduction

Light has the ability to exert a force. Photons carry momentum, and when a particle suspended in a medium has a different index of refraction than the medium, an incident light ray will be refracted at the interface; the momentum of the photons is changed, as they change direction. Satisfying conservation of momentum, this change in momentum of the photons is transferred to the particle and the particle experiences a force.

In 1969 Arthur Ashkin realized that the force one photon exerts was small, but that the many photons in a laser beam generated a total force in the piconewton range — large enough to accelerate a micrometer-sized particle [1]. A year later, in 1970, Ashkin reported the trapping and manipulation of micron-sized dielectric particles in liquid and of water droplets in air, employing two counter-propagating laser beams and, in addition, predicted the extension of optical manipulation to atoms and molecules [2]. With this, he had established the basis for a new technique, and in 1986, Ashkin and colleagues demonstrated what later became known as optical tweezers: the method to manipulate particles using a single, tightly-focused, laser beam.

The details of how a single beam can hold a particle in its place are discussed in Section 1.2. First, we will mention several of the many applications that optical tweezers brought into reach and that have been explored since the pioneering work of Ashkin and colleagues.

A nice example of exploiting the optical properties of a material forms the work of Dharmadhikari and colleagues [3], who selected malaria-infected cells using optical tweezers. Red blood cells, approximately 7 μm in diameter, can be held in optical tweezers, due to the refractive index contrast they have with aqueous media. As Dharmadhikari *et al.* showed, inside the optical trap the red blood cells changed from their usual disk-like shape to a rod, under the influence of the optical forces. Rods infected with malaria rotated in the linearly polarized light, while uninfected cells did not, thus making it possible to distinguish between infected and uninfected cells.

In other experiments, the material under investigation is not trapped itself. Smith *et al.* [4] attached two microspheres to either side of a DNA strand, of which one was held with a micropipette, while the other sphere was pulled using optical tweezers. Using this configuration, Smith *et al.* were able to measure the 65-pN-force needed to overstretch a DNA molecule. In the work of Brower-Toland and colleagues [5], the DNA was in its nucleosomal form, the level of organization at which it is wrapped around histone protein units. With one end of the DNA attached to the microscope glass and the other to a polystyrene microsphere, the DNA was stretched and pulled loose from the histones. By accurately measuring the position of the trapped particle, the binding positions

were recorded, revealing the wrapping configuration of the DNA around the histones with sub-nanometer precision.

These examples illustrate several of the aspects of the non-invasive technique of optical trapping. Microscopic particles can be trapped and used as handles to manipulate even smaller macromolecules, such as 2-nm-wide DNA molecules [4, 5], or 25-nm-diameter microtubules [6]. Step sizes as small as 0.1 nm can be measured in real time [7] and, in addition, forces in the picoNewton range can be exerted on a trapped particle, and determined by doing position detection on that same particle. Different kinds of particles can be held in optical tweezers, from dielectric particles (like polystyrene [5] and silica) and metal particles, such as gold [8] and silver, to biological particles, including viruses [9], bacteria [9], yeast cells [10, 11], red blood cells [3, 12], and chromosomes [13]. These particles — with a wide variety of shapes ranging from spheres, rods [9], dumbbells [14], disks [3, 15], doughnuts [16], and cylinders [17], to rotors and other arbitrary shapes created e.g. by polymerization of a resin [18] — are used in biophysics, and in the fields of colloid physics, chemistry, and microrheology [19], to name a few.

The applications are many-fold, and the possibilities virtually endless. There are, however, certain limitations to the technique. Micrometer-sized particles with a very high refractive-index contrast, such as silicon and titania, and large metal particles, cannot be trapped in single-beam gradient tweezers. In addition, the forces exerted with optical tweezers have so far been limited to typically 100 pN, keeping a range of applications out of reach. The work described in this thesis focuses on these two aspects. By using a second, opposing, trapping beam [2], we confine and manipulate high-refractive index particles. Moreover, we investigate the possibilities to use this configuration to extend the level of force beyond its current limitations.

In the remainder of this Introduction, we examine the optical forces exploited in optical tweezers, and discuss the trapping of high-index particles in counter-propagating traps. We elaborate on the use of optical tweezers in colloid physics and on the purpose of high-force exertion in biophysics, after which we end with an overview of the work presented in the other Chapters in this thesis.

1.2 Theory of optical trapping

The optical forces exerted on a particle originate from the momentum change of the photons impinging on the particle. These forces have traditionally been decomposed into two components [20]: the gradient force and the scattering force. The scattering force acts, for a symmetric beam, in the propagation direction of the beam, pushing the particle along, while the gradient force on a particle with an index higher than that of the surrounding medium, is directed towards the region of highest light intensity.

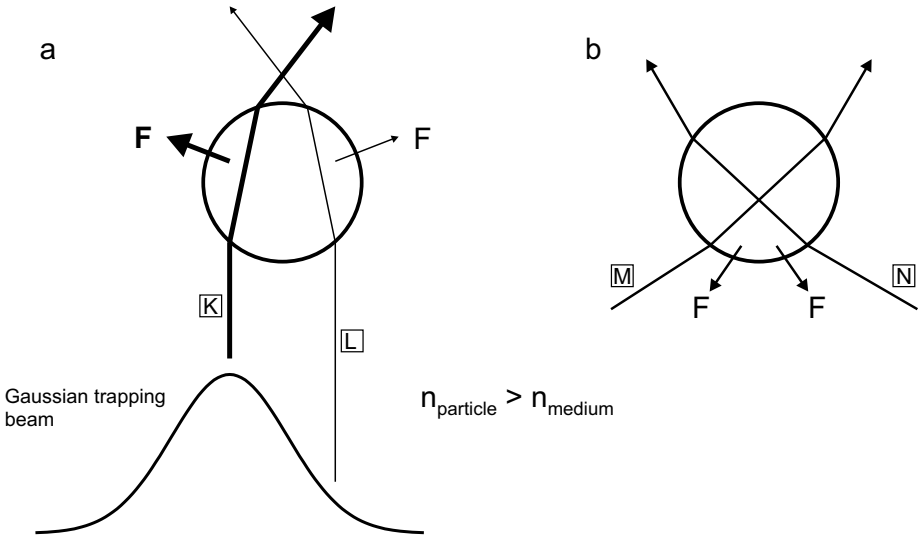

Fig. 1.1: Schematic of the Geometrical Optics (GO) description of the gradient force for a particle with an index of refraction higher than the one of the medium. (a) For a lateral intensity gradient, the resulting force, due to the refraction of the light at the interface, has a component towards the highest intensity. (b) In a focused laser beam, the axial force is always directed towards the focus.

To get a feeling for the origin of the gradient force, we will use geometric optics (GO) — valid for particles much larger than the wavelength — in which the light is treated as a collection of rays obeying the laws of reflection and refraction. In Figure 1.1a, light rays are refracted at the interface of a particle and the medium it is suspended in, for which the refractive index n_p of the particle is larger than the index n_m of the medium. The photons of light ray K are refracted towards the right, resulting in a force on the particle towards the left. Similarly, light ray L yields a force to the right. As the intensity of ray K exceeds the intensity of ray L, the resulting force has a component to the left; the particle is drawn to the region of highest light intensity.

The particle, however, is also propelled forward, in part by the reflections of the beam at the surface (not drawn). To compensate for this destabilizing force component and confine the particle in three dimensions, Ashkin used in his first experiments two counter-propagating beams with low numerical aperture [2]. Later he demonstrated the levitation trap, where the laser beam was directed upwards and the gravitational force counter-acted the scattering force [21]. The most used method to create a stable three-dimensional (3D) potential well, however, is to tightly focus the trapping laser beam using a high-numerical aperture (NA) objective.

Such a single-beam gradient trap, or optical tweezers, is depicted in Figure 1.1b. In this Figure, the particle is displaced along the beam axis with respect to the focus. The focused light rays M and N are refracted upward, resulting in a force down, supplying the restoring force in the direction of the focus. Similarly, when the particle is positioned below the focus, it will experience a force upward. For a focused Gaussian laser beam, as is often used in optical trapping, these effects result in a gradient force which is always directed towards the focus of the laser beam. Stable trapping — due to the axial component of the scattering force always just beyond the focus — will occur when the potential well of the trap is deep enough compared to the thermal energy of the particle.

To form an idea of what determines the optical forces, we will use the Rayleigh approximation, valid for particles much smaller than the wavelength of the trapping beam. The particle is regarded as a dipole interacting with the light field, and we can write for the gradient force F_{grad}:

$$F_{grad} = \frac{2\pi r^3}{c}\left(\frac{m^2-1}{m^2+2}\right)\nabla I_0, \tag{1.1}$$

with r the radius of the particle, c the speed of light, and I_0 the intensity. The effective refractive index m is the ratio between the index of the particle and the index of the medium: $m = n_p/n_m$. The scattering force is given by:

$$F_{scat} = \frac{n_m}{c}\frac{128\pi^5 r^6}{3\lambda^3}\left(\frac{m^2-1}{m^2+2}\right)^2 I_0, \tag{1.2}$$

where λ is the wavelength of the light.

As the gradient of the intensity is proportional to the intensity, we see that the scattering force, as well as the gradient force, are proportional to the intensity of the laser light. In addition, both force contributions depend on the radius r and on the index ratio m. The scattering force, however, depends stronger on both r and m. This indicates that for certain size and refractive index, the scattering force cannot be compensated by the axial gradient force: there is a limit to the size and index of a particle to be trapped. And, as a consequence, a limit is set to the force per laser power in a single-beam gradient trap.

So far, we have utilized GO and the Rayleigh approximation to discuss the optical forces in laser tweezers. With trapping light in the visible or near-infra red, however, many colloidal particles are neither much larger, nor much smaller than the wavelength. Therefore, to calculate the trapping forces in a more quantitative way, we use an explicit partial-wave (Lorenz-Mie) representation, as presented by Mazolli *et al.* [22]. With this method, the three-dimensional force field for a particle in a tightly-focused Gaussian laser beam can be calculated. For the purpose of this Introduction, however, we will only take a look at the force along the optical axis.

Figure 1.2a shows the calculated axial force curves for a silica particle (refractive index $n = 1.45$) and a ZnS particle ($n = 2.0$), both 1 μm in diameter, in a single-beam gradient trap in water ($n = 1.33$). At the stable trapping position of the silica particle, indicated by the arrow, the force is zero. To both sides, the microsphere experiences a restoring force: a negative force for displacements in the propagation direction of the beam, and a positive force for displacement against the beam direction. As mentioned before, due to the axial scattering force the stable axial trapping position lies just beyond the focus of the beam ($z = 0$). The force curve for the titania particle, however, is positive along the whole beam axis; the particle is only pushed forward and cannot be stably trapped. By adding an opposing trapping beam, like Ashkin did in his first experiments [2], the destabilizing scattering forces are cancelled. Figure 1.2b depicts the force curve for the titania particle in such a counter-propagating trap, showing a stable trapping position at $z = 0$, where the two foci overlap. Also shown are the curves for the two individual beams, with 50% of the power in each beam.

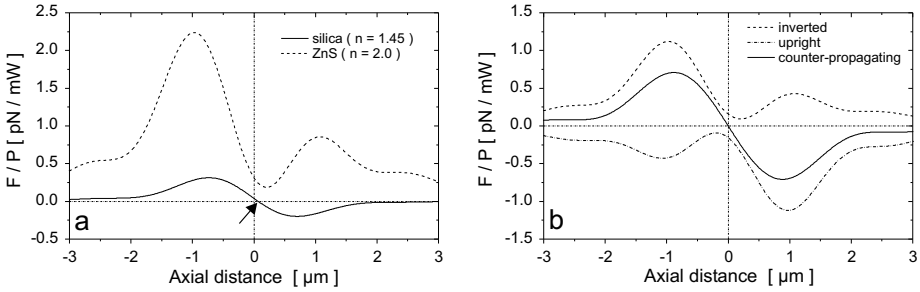

Fig. 1.2: Force per Watt laser power along the beam axis. (a) Curves for a silica particle (n = 1.45) and a ZnS (n = 2.0) particle, both 1 µm in diameter, trapped in water (n = 1.33) in a single-beam trap. The silica particle is trapped close to the laser focus, but the ZnS particle has no stable trapping position. (b) Curve for a 1-µm-diameter ZnS particle trapped in counter-propagating traps (solid line). The particle is trapped at the overlapping foci of the beams (z = 0). The individual two beams coming from either side (with half the laser power each) are also shown.

Besides Ashkin [2], others have also used the configuration of opposing trapping beams to overcome the scattering force [23, 24]. In the work presented in this thesis, however, we combine counter-propagating trapping with tightly focusing the laser beams — increasing the intensity gradient — and exert high forces on high-refractive index particles that otherwise cannot be trapped.

1.2.1 Force measurements

Optical tweezers are suitable to trap micrometer-sized particles, but also enable force measurements on those trapped particles.

In the potential well of the trap, a particle will, for a displacement to either side, experience a restoring force keeping it in the well. For small displacements, the potential can be regarded as harmonic: the force is proportional to the displacement. The force per displacement is called the stiffness κ of the system, similar to the stiffness of a spring. And just as for a spring, after calibration of the stiffness, the displacement of the particle away from the equilibrium position will yield the force.

Calibration is done by applying a known force and measure the displacement [25, 26]. For the optical trap, this force can, for example, be the drag force on a trapped microsphere, applied by moving the medium relative to the particle. The drag force on the particle is then determined by the radius of the sphere, the viscosity of the medium, and the speed. Calibration can also be done by observing the Brownian motion of the particle. This motion is due to the constant bombardment of the surrounding molecules of the medium. Also when confined by optical tweezers does a particle display Brownian motion. For spheres, the motion due to this thermal energy is characterized, and the stiffness — typically in the order of 10 to 50 pN/μm — can be obtained.

In conclusion, accurate nanometer-level position detection, usually done using microscopy image analysis [27] or quadrant photodiode detection [28, 29], plays a key role in force measurements using optical tweezers.

1.3 High forces in biophysics

The possibility to exert and measure picoNewton-level forces in a non-invasive manner, make optical tweezers a suitable tool in the field of bio-physics [30]. Optical trapping has been used to determine material properties at the (macro-)molecular level. Also, the forces generated by motormolecules, such as the flagellar motor of a bacterium [31] and the packaging motor of a bacteriophage [32], have been measured as well.

However, while the forces in single-molecule experiments are typically of the order of a few to several tens of picoNewtons, phenomena on the cellular level, with many molecules involved, quickly exceed the limit of ∼100 pN obtainable by single-beam optical tweezers. Forces exerted during cell division, for example, have so far been out of reach for optical trapping. Other techniques that have been used to exert forces in biophysical studies include atomic force microscopy (AFM), micropipettes, and magnetic tweezers. With AFM, forces of 10 – 10.000 pN can be exerted, and the technique can be applied in aqueous media. AFM is, however, like the use of micropipettes, an invasive technique, and not all experiments are suited for this. Magnetic tweezers, able to exert forces up to

200 pN, are not locally applicable.

Optical tweezers are non-invasive and locally applicable, and many more experiments will get into reach when they can exert higher forces. The possibilities to pursuit these higher forces are, however, limited. The trapping force is proportional to the laser power. Apart from the higher costs for high-power lasers, the main restriction is heating of the sample and photodamage resulting from absorption of light. Especially when handling biological material, laser damage plays a role, even though the absorption is limited by the use of infra red light [10]. In addition, for biophysical experiments in general aqueous media are used, fixing the refractive index to $n = 1.33$.

The parameters that are left to optimize, are the size and refractive index of the particle, and the shape of the trapping beam. The influence of these parameters on the trap stiffness is discussed and investigated in this thesis.

1.4 Optical tweezers in colloid and interface science

A colloid or colloidal dispersion is a system of small particles stably dispersed in a medium. Examples of a colloidal dispersion are milk (consisting of liquid droplets in another liquid), and paint, in which solid particles are dispersed in a liquid. Colloidal particles, with sizes ranging from a few nanometers up to several micrometers, display Brownian motion. Due to this thermal motion, they show phase transitions such as crystallization and melting, just like atomic and molecular systems. However, contrary to atoms and most molecules, their sizes enable imaging using light microscopy. In addition, the properties and geometry of colloidal particles can be tuned, and the synthesis of dielectric particles and metallo-dielectric particles, with sphere, core-shell, core-half shell, plate, rod, and dumbbell-geometry, has been demonstrated. These properties make colloids well suited to function as a model system for atomic and molecular interactions. Moreover, combined with fluorescence confocal microscopy, fluorescently-labeled core-shell particles enable 3D imaging of individual particles in dense colloidal structures [33].

Optical tweezers are used in the study of hydrodynamic interactions [34], pair potentials [35], and three-body interactions [36]. The applications we focus on in this work, however, are the patterning of surfaces and the manipulation of individual particles in the bulk of a colloid.

Patterned surfaces can be used to direct the crystallization of a concentrated colloidal dispersion. With this technique, called colloidal epitaxy or template directed growth, crystals can be grown into desired orientations and even the growth of metastable crystals has been demonstrated. Patterning is usually done by self-organization, for example controlled drying, but optical tweezers offer the possibility of manipulation on single-particle level [37]. Also, particles can be patterned on top of an existing layer [37]. By two-step self-assembly,

high-refractive index particles can be incorporated in 3D colloidal structures, enabling the manipulation of defects in photonic crystals.

1.5 This thesis

In this thesis, we developed optical trapping techniques with certain applications in mind, for biophysics experiments where forces higher than 100 pN are expected and for the controlled patterning and manipulation of multi-component colloidal systems. For this, several new features were necessary, and we describe those features and show how they can be applied.

In the experimental setups developed by us, two opposing high-NA objectives were used. In Chapter 2, this configuration enabled trapping with one objective and simultaneous 3D fluorescent confocal imaging using the other. Particles with a high-index core were trapped inside a bulk of index-matched particles to induce colloidal crystallization. The effects of the trapped structure on the surrounding particles were imaged in 3D. When there is a mismatch in the refractive index between the objective immersion fluid and the medium in which we trap, the laser focus is distorted. In Chapter 3 we look at the origin of these spherical aberrations, and discuss the consequences for both trapping and imaging.

By splitting the laser beam, the setup could also be used to create counter-propagating optical tweezers in which high-refractive index particles could be stably confined in 3D. In Chapter 4 this was applied to pattern surfaces with mixtures of particles, including high-index particles. The colloids were selected from a separate reservoir, and moved to the patterning region with long-range motorized actuators. By using a high-accuracy piezo stage in a feedback loop with video microscopy position detection to reposition the sample, the drift in the system was compensated for and large areas could be patterned with mixtures of particles.

In Chapter 5, the trapping of multiple high-refractive index particles in dynamic arrays of counter-propagating tweezers was demonstrated, and in Chapter 6 those dynamic counter-propagating traps were used to create counter-propagating line tweezers in which high-refractive index ZnO rods were trapped. This enabled full 3D translational and in-plane rotational control of the semiconducting nanorods, expanding the possibilities to position individual rods in complex geometries.

In Chapter 7, a setup is presented in which counter-propagating trapping with two high-numerical aperture objectives was combined with quadrant photodiode position detection. This enabled force measurements employing high-index particles. The enhancement of trap stiffness that can be expected for the use of high-index particles was demonstrated and calculated in Chapter 8.

BIBLIOGRAPHY

[1] A. Ashkin. Optical trapping and manipulation of neutral particles using lasers. *Proc. Natl. Acad. Sci. USA*, 94(10):4853–4860, 1996.

[2] A. Ashkin. Acceleration and trapping of particles by radiation pressure. *Phys. Rev. Lett.*, 24(4):156–159, 1970.

[3] J. A. Dharmadhikari, S. Roy, A. K. Dharmadhikari, S. Sharma, and D. Mathur. Torque-generating malaria-infected red blood cells in an optical trap. *Opt. Express*, 12(6):1179–1184, 2004.

[4] S. B. Smith, Y. Cui, and C. Bustamante. Overstretching B-DNA: the elastic response of individual double-stranded and single-stranded DNA molecules. *Science*, 271:795–799, 1996.

[5] B. D. Brower-Toland, C. L. Smith, R. C. Yeh, J. T. Lis, C. L. Peterson, and M. D. Wang. Mechanical disruption of individual nucleosomes reveals a reversible multistage release of DNA. *Proc. Natl. Acad. Sci. USA*, 99(4):1960–1965, 2002.

[6] J. W. J. Kerssemakers, M. E. Janson, A. van der Horst, and M. Dogterom. Optical trap setup for measuring microtubule pushing forces. *Appl. Phys. Lett.*, 83(21):4441–4443, 2003.

[7] L. Nugent-Glandorf and T. T. Perkins. Measuring 0.1-nm motion in 1 ms in an optical microscope with differential back-focal-plane detection. *Opt. Lett.*, 29(22):2611–2613, 2004.

[8] P. M. Hansen, V. K. Bhatia, N. Harrit, and L. Oddershede. Expanding the optical trapping range of gold nanoparticles. *Nanoletters*, 5(10):1937–1942, 2005.

[9] A. Ashkin and J. M. Dziedzic. Optical trapping and manipulation of viruses and bacteria. *Science*, 235(4795):1517–1520, 1987.

[10] A. Ashkin, J. M. Dziedzic, and T. Yamane. Optical trapping and manipulation of single cells using infrared laser beams. *Nature*, 330:769–771, 1987.

[11] M. Goksør, J. Enger, and D. Hanstorp. Optical manipulation in combination with multiphoton microscopy for single-cell studies. *Appl. Opt.*, 43(25):4831–4837, 2004.

[12] R. W. Applegate Jr., J. Squier, T. Vestad, J. Oakey, and D. W. M. Marr. Optical trapping, manipulation, and sorting of cells and colloids in microfluidic systems with diode laser bars. *Opt. Express*, 12(19):4390–4398, 2004.

[13] J. F. Ojeda, C. Xie, Y.-Q. Li, F. E. Bertrand, J. Wiley, and T. J. McConnell. Chromosomal analysis and identification based on optical tweezers and Raman spectroscopy. *Opt. Express*, 14(12):5385–5393, 2006.

[14] V. Bingelyte, J. Leach, J. Courtial, and M. J. Padgett. Optically controlled three-dimensional rotation of microscopic objects. *Appl. Phys. Lett.*, 82(5):829–831, 2003.

[15] Z. Cheng, P. M. Chaikin, and T. G. Mason. Light streak tracking of optically trapped thin microdisks. *Phys. Rev. Lett.*, 89(10):108303, 2002.

[16] E. Higurashi, O.Ohguchi, and H. Ukita. Optical trapping of low-refractive-index

microfabricated objects using radiation pressure exerted on their inner walls. *Opt. Lett.*, 20(19):1931–1933, 1995.

[17] R. C. Gauthier, M. Ashman, A. Frangioudakis, H. Mende, and S. Ma. Radiation-pressure-based cylindrically shaped microactuator capable of smooth, continuous, reversible, and stepped rotation. *Appl. Opt.*, 38(22):4850–4860, 1999.

[18] P. Galajda and P. Ormos. Rotors produced and driven in laser tweezers with reversed direction of rotation. *Appl. Phys. Lett.*, 80(24):4653–4655, 2002.

[19] M. Atakhorrami, J. I. Sulkowska, K. M. Addas, G. H. Koenderink, J. X. Tang, A. J. Levine, F. C. MacKintosh, and C. F. Schmidt. Correlated fluctuations of microparticles in viscoelastic solutions: Quantitative measurement of material properties by microrheology in the presence of optical traps. *Phys. Rev. E*, 73(6):061501, 2006.

[20] A. Ashkin. Observation of a single-beam gradient force optical trap for dielectric particles. *Opt. Lett.*, 11(5):288–290, 1986.

[21] A. Ashkin and J. M. Dziedzic. Optical levitation by radiation pressure. *Appl. Phys. Lett.*, 19(8):283–285, 1971.

[22] A. Mazolli, P. A. Maia Neto, and H. M. Nussenzveig. Theory of trapping forces in optical tweezers. *Proc. R. Soc. Lond. A*, 459:3021–3041, 2003.

[23] W. Grange, S. Husale, H.-J. Güntherodt, and M. Hegner. Optical tweezers system measuring the change in light momentum flux. *Rev. Sci. Instrum.*, 73(6):2308–2316, 2002.

[24] S. B. Smith, Y. Cui, and C. Bustamante. Optical-trap force transducer that operates by direct measurement of light momentum. *Methods in Enzymology*, 361:134–162, 2003.

[25] M. Capitanio, G. Romano, R. Ballerini, M. Giuntini, F. S. Pavone, D. Dunlap, and L. Finzi. Calibration of optical tweezers with differential interference contrast signals. *Rev. Sci. Instrum.*, 73(4):1687–1696, 2002.

[26] A. Buosciolo, G. Pesce, and A. Sasso. New calibration method for position detector for simultaneous measurements of force constants and local viscosity in optical tweezers. *Opt. Comm.*, 230:357–368, 2004.

[27] J. C. Crocker and D. G. Grier. Methods of digital video microscopy for colloidal studies. *J. Colloid Interface Sci.*, 179:298–310, 1996.

[28] K. Visscher, S. P. Gross, and S. M. Block. Construction of multiple-beam optical traps with nanometer-resolution position sensing. *IEEE J. Sel. Top. Quant. Electronics*, 2(4):1066–1076, 1996.

[29] M. W. Allersma, F. Gittes, M. J. deCastro, R. J. Stewart, and C. F. Schmidt. Two-dimensional tracking of ncd motility by back focal plane interferometry. *Biophys. J.*, 74:1074–1085, 1998.

[30] M. J. Lang and S. M. Block. Laser-based optical tweezers. *Am. J. Phys.*, 71(3):201–215, 2003.

[31] S. M. Block, D. F. Blair, and H. C. Berg. Compliance of bacterial flagella measured with optical tweezers. *Nature*, 338:514–518, 1989.

[32] D. E. Smith, S. J. Tans, S. B. Smith, S. Grimes, D. L. Anderson, and C. Bustamante. The bacteriophage $\phi 29$ portal motor can package DNA against a large internal force. *Nature*, 413:748–752, 2001.

[33] A. van Blaaderen and P. Wiltzius. Real-space structure of colloidal hard-sphere glasses. *Science*, 270:1177–1179, 1995.

[34] S. Henderson, S. Mitchell, and P. Bartlett. Position correlation microscopy: probing single particle dynamics in colloidal suspensions. *Colloids and Surfaces A*,

190:81–88, 2001.

[35] M. Brunner, C. Bechinger, W. Strepp, V. Lobaskin, and H. H. von Grünberg. Density-dependent pair interactions in 2D colloidal suspensions. *Europhys. Lett.*, 58(6):926–932, 2002.

[36] J. Dobnikar, M. Brunner, H.-H. von Grünberg, and Clemens Bechinger. Three-body interactions in colloidal systems. *Phys. Rev. E*, 69(3):031402, 2004.

[37] J. P. Hoogenboom, D. L. J. Vossen, C. Faivre-Moskalenko, M. Dogterom, and A. van Blaaderen. Patterning surfaces with colloidal particles using optical tweezers. *Appl. Phys. Lett.*, 80(25):4828–4830, 2002.

2. OPTICAL TWEEZERS SETUP FOR INDEPENDENT THREE-DIMENSIONAL MANIPULATION AND IMAGING

An optical tweezers setup is described, in which the use of two high-numerical aperture objectives, one above and one below the sample, enables imaging to be completely decoupled from trapping. By combining a Pockels cell and polarizing beam splitters, two trapping planes were created at different depths in the sample, in which arrays of optical traps could be manipulated independently, and a three-dimensional structure could be trapped. A mixture of refractive-index-matched particles and high-index particles was used to trap several of the high-index particles inside the bulk of the non-trappable index-matched particles. The dispersion was imaged in three dimensions using confocal microscopy, to investigate the influence of the trapped particles on the configuration of particles in the bulk.

2.1 Introduction

Since the invention of optical tweezers by Ashkin and co-workers [1, 2], optical tweezers have found widespread use in fields like biology, physical chemistry, and (bio-) physics [3–6]. An optical trap can be created by focusing a laser beam to a diffraction-limited spot using a high-numerical aperture (NA) objective. The strong light gradient near the focus creates a potential well, in which a particle with a refractive index higher than that of the surrounding medium is trapped. The forces on a particle can be decomposed into a "gradient force" in the direction of increasing light intensity and a "scattering force" directed along the optical axis. The particle is trapped at the point where these two force contributions balance, if the maximal restoring force of the trap is large enough to overcome the effective weight and thermal fluctuations of the particle. The general calculation of the optical forces on a particle in a trap is a challenging problem [7]. This task is simpler in the regimes where a particle is either much smaller (Rayleigh) [8] or much larger (geometrical optics (GO)) [9] than the wavelength of the light used for trapping. Dielectric particles, small metal particles, as well as living materials, with sizes ranging from several nanometers to tens of micrometers, can be trapped and manipulated in a single-beam gradient trap as long as the scattering force is not too large. If there is no difference in refractive index between the particle and its surroundings, no direct optical forces are exerted on the particle. If the refractive index of the particle is lower than that of the medium, the particle is expelled from the trapping beam. However, alternative schemes such as rapid beam scanning [10] and the use of light beams with a phase singularity [11], have been invented to manipulate particles in this situation. Recent developments have broadened the kind of forces that can be exerted onto small objects to include bending [12], torque [13, 14], and stretching [15].

To manipulate more than one particle at once, a number of methods have been developed to create and manipulate planar arrays of optical traps using galvano [16] or piezoelectric [17] scanning mirrors, acousto-optic deflectors (AODs) [3], (computer-generated) diffractive optical elements [18–21], interference of specially designed light beams [22, 23], or the generalized phase contrast method [24].

At around the same time the single-beam optical tweezers were pioneered, the confocal microscope was reinvented after it was first demonstrated at the end of the 1950s [25, 26]. At present, confocal fluorescence microscopy is widely used in biology and medicine, and its use in chemistry, physics, and materials science is on the rise [27–29]. In confocal microscopy, the sample is illuminated with a diffraction-limited spot while detection occurs by imaging the focal region with the same objective onto a pinhole aperture. Only a thin section of the sample contributes to the signal, thus out-of-focus stray light is efficiently reduced by

the detection pinhole. By scanning the beam in the sample, a three-dimensional image can be built up. Besides the sectioning capability, the use of pinholes also leads to an increase in resolution compared to conventional microscopy [30].

Because of their tunability, in size, shape, as well as chemical composition, and their ability to self-organize, colloids find their applications in the development of advanced materials like photonic crystals [31]. In addition, colloidal systems are used as a model system in condensed matter [32–34]. Colloids have, like atoms, a well-defined thermodynamical temperature, their interaction potential is tunable, and the time and length scales involved are experimentally accessible. Recent developments in particle synthesis and labeling of particles with fluorescent dyes opened up the possibility to perform quantitative three-dimensional analysis using confocal microscopy on a single particle level [35]. Examples are experiments investigating the glass transition [36] and nucleation and growth of crystals [34, 37] in colloidal dispersions. Optical tweezers have been used to manipulate colloidal particles, to pattern substrates with two- and three-dimensional structures [38, 39], and to measure double layer repulsions [40], depletion [41], and hydrodynamic interactions [42]. However, as selective manipulation in a concentrated dispersion was not possible until now, all applications have been limited to systems that were either (almost) two-dimensional [32, 43] or had a very low particle concentration [23, 44].

Combining the powerful techniques of optical tweezers and confocal microscopy opens up series of new experiments. For example, three-dimensional structures can be created with optical tweezers and can be imaged and studied in detail in three dimensions. In addition, their effect on other particles that are not trapped, can be analyzed in three dimensions. The simplest way of combining optical tweezers with a confocal microscope is by using the same objective to image and to trap. However, this makes it impossible to use the three-dimensional scanning ability, and only one plane is imaged [45]. Hoffmann and co-workers implemented optical trapping and three-dimensional imaging using one objective and fast scanning compensating optics to keep the tweezers at a fixed position [46]. The use of two independent microscope objectives for trapping and imaging was pioneered by Visscher and co-workers [12, 47], although trapping was limited to a two-dimensional plane.

In Section 2.2 we describe the use of two microscope objectives, one above and one below the sample, to decouple imaging and trapping completely. Samples could be imaged quantitatively in three dimensions without affecting the optical trapping performance. AODs were used to create large two-dimensional arrays of traps that could be changed dynamically. Three-dimensional arrays of traps were created by fast switching between two beam paths using AODs, a Pockels cell, and polarizing beam splitters.

Here we extend the use of optical tweezers in soft condensed matter systems to an individual particle level in concentrated dispersions using core-shell parti-

cles. We induced crystallization in a concentrated dispersion and demonstrate that selective trapping of core-shell particles inside a concentrated dispersion of index-matched particles in combination with three-dimensional imaging is possible. Some preliminary results were described in Ref. [33]. In addition, using counter-propagating beams [1, 48] we trapped high-refractive index particles that were not stably trapped in a single-beam gradient trap.

2.2 Experimental setup and details

In this optical tweezers setup (see Figure 2.1) we use a diode-pumped Nd:YVO_4 laser (Spectra Physics, Millennia IR, 10 W cw) with a wavelength of 1064 nm and a TEM_{00} mode profile. The wavelength was chosen such that it is well separated from the excitation and emission wavelengths of the fluorescent dyes used in the confocal microscopy modes. This wavelength also minimizes absorption and scattering in biological materials. This infrared (IR) laser beam is expanded 6× using a beam expander (*EXP*, Melles Griot). The beam is attenuated using a polarizing beam splitter cube (*C1*) in combination with a half-lambda zero-order wave plate (*W1*, Newport), which rotates the vertically polarized laser light. The horizontally polarized fraction is directed into a beam dump.

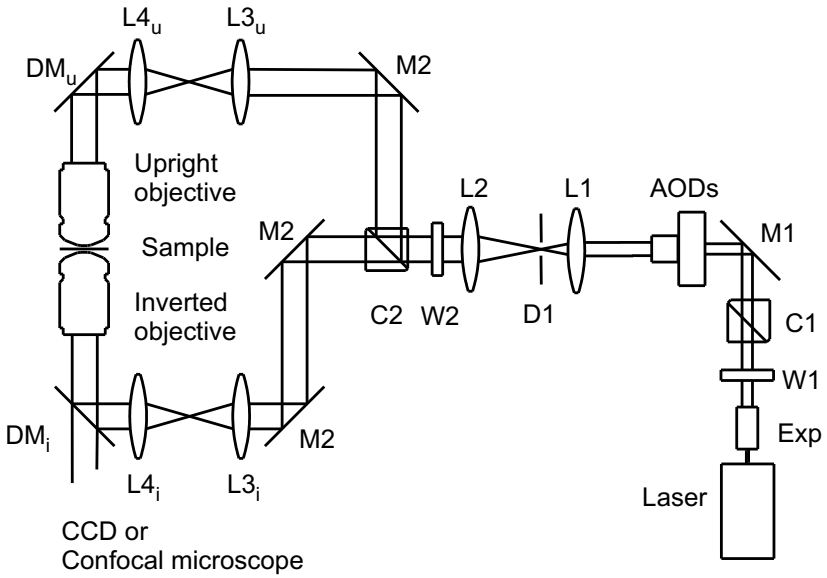

Fig. 2.1: Schematic diagram of the setup in which the use of two objectives allows imaging to be completely decoupled from trapping. Rotation of waveplate W2 selects between inverted, upright, and counter-propagating trapping. AODs were used for beam-steering and the creation of arrays of traps.

Using gimbaled mirror (*M1*), the vertically polarized beam is coupled into a pair of orthogonal AODs (IntraAction Corp., DTD-276HB6, 6×6 mm^2 aperture). In the TeO_2 crystals of the AODs, a diffraction grating is set up by a propagating sound wave. The laser beam is deflected at specific angles and intensities that depend on the frequency and the amplitude of the sound wave in the crystal, respectively. We corrected, if needed, for the diffraction efficiency of the AODs not being constant over the frequency range, either by adjusting the amplitude of the signal to the AODs or by changing the relative time spent by the laser beam at a certain frequency.

A synthesizer board and amplifier (both IntraAction Corp.) allow for fast and accurate control over the position as well as over the stiffness of the optical trap. The synthesizer board was controlled using a *LabVIEW* (National Instruments) program, which addressed a *C++* program when faster switching was needed. Using the AODs, the beam is scanned quickly from point to point in the sample to create arrays of tweezers with great control over the position of the traps. We also used Direct Digital Synthesizers (DDS, Novatech Instruments Inc., DDS8m 100 MHz) to create multiple traps without time-sharing the laser beam. Two frequencies were applied simultaneously to one of the AODs, resulting in a corresponding number of diffracted beams. With this procedure, the beams are not time-shared and can be modulated independently. Later, the synthesizer board was replaced by the DDSs for all control of the AODs, including time-sharing, and a new *LabVIEW* program was written.

The two AODs are each fitted on a four-axis kinematic stage (New Focus, 9071-M) for better alignment. As the AODs diffract the incoming laser into multiple beams, a diaphragm (*D1*) is used to select the (1,1)-order for trapping. By careful alignment of the AODs with respect to the incoming laser beam, up to 60% of the light of the original undiffracted beam can be transferred into the (1,1)-order.

The deflected beam is expanded further using a telescope with lenses *L1* ($f = 120$ mm) and *L2* ($f = 250$ mm). All lenses are Melles Griot achromatic doublets, while the mirrors and beam-splitting cubes were obtained from Newport. All components have an antireflection coating for 1064 nm. The combination of the telescope and the beam expander broadens the laser beam approximately 12 times to a width of $2\omega_0 = 5.6$ mm, filling the back aperture of the 100× objective.

Switching between different trapping modes is done using a half-lambda wave plate *W2* combined with a polarizing beam splitter cube *C2*. Rotation of the wave plate determines the fraction of the beam diverted to the upper or the lower beam paths, thereby switching between inverted and upright trapping modes. When both paths are used at the same time, inverted and upright single beam optical traps can be created at different heights in the sample. Dual-beam counter-propagating optical tweezers can be created when the inverted

and upright tweezers are aligned on top of each other.

Mirrors (*M2*) and the 1:1-telescope lenses ($L3_{i,u}$ and $L4_{i,u}$, all $f = 80$ mm) guide the beam to the microscope. The lenses $L3_{i,u}$ are placed on xyz-stages fitted with micromanipulators. The lenses $L3_{i,u}$, as well as the AODs, are positioned in planes conjugate to the back focal planes of the objectives. This allows for manipulation of the optical traps in the front focal planes of the objectives by changing the angles at which the beams enter the back apertures of the microscope objectives. The lenses $L3_{i,u}$ are achromatic doublet lenses to minimize aberrations. Also, the displacement of these lenses from the optical axis is small, and we have not seen any notable change in trap efficiency when lenses $L3_{i,u}$ were moved. For optimal two-dimensional position control, the AODs are aligned such that the plane between the two AODs is conjugate to the back focal planes of the two objectives. The distance between the centers of the AODs is 32 mm.

Two dichroic mirrors ($DM_{i,u}$, Chroma Technology Corp.) are attached to the body of an inverted microscope (Leica, DM IRB). The mirrors reflect the 1064 nm laser beam into the back apertures of the objectives while they allow imaging in the visible. The revolver of the microscope is replaced with a block holding the inverted objective placed on a piezo microscope objective scanner (Physik Instrumente, Pifoc P-721.20), and the condenser is replaced by the upper microscope objective. This upright objective is mounted on an xyz-translation stage fitted with microscrews (Newport) for manipulation and alignment. The upright objective can be used as a condenser for imaging as well as for trapping. We used 100×(1.4-0.7 NA), 63×(1.4 NA), and 40×(1.25-0.75 NA) oil immersion objectives and a 20×(0.7 NA) air objective. All objectives were plan apochromats obtained from Leica.

The maximum displacement of the trap in the sample is determined by the maximum deflection angle of the beam at the AODs, by the optics in the setup, and by the magnification of the microscope objective used. For the (1,1)-order order, a center frequency of 25 MHz on the AODs deflects the beam 45 mrad with respect to the zeroth-order undiffracted beam. The accessible frequency interval ranges from 16 to 34 MHz corresponding to a deflection between -15 and $+15$ mrad of the beam at the AODs. The deflection angle at the back aperture of the objectives was reduced by a factor of 2.1 because of the telescope behind the AODs. The resulting maximum displacement of the optical traps in the sample was found to be 28, 45, and 71 μm in both the x- and y-direction for the 100×, 63×, and 40× objectives, respectively.

A high-resolution xy-piezo stage (Physik Instrumente, P-730.4C, accuracy better than 0.5 nm when operated in a closed-loop circuit) provided the ability to move the sample with high accuracy, and was mounted on a modified stage (Rolyn, 750-MS) with motorized actuators (Newport, 850G-LS, low speed closed-loop motorized actuators) for long-range displacements. Later, the piezo

stage was replaced by an xyz-piezo stage (Physik Instrumente, P-563.3CD) with a range of $300\times300\times300$ μm^3.

The power of the laser was measured using a broadband power meter (Melles Griot) and the setup was built on a vibration-isolation table (Melles Griot).

2.2.1 Arrays of tweezers in more than one plane using one objective

To create multiple traps in different planes and image the sample in three dimensions simultaneously, the laser beam was split into two beams, which were recombined after changing their relative divergence (Figure 2.2). As the position of the trapping plane is determined by the divergence (or convergence) of the beam at the back focal plane of the objective, we were able to create traps in two different planes in the sample. Addressing these planes can be done using a polarizing beam splitting cube in combination with a Pockels cell, an electro-optic modulator in which the strength of an electric field over a crystal determines the birefringence of that crystal. By choosing the right electric field strengths, we can switch the linearly polarized laser beam between horizontally and vertically polarized, and with that, between the two beam paths. Synchronizing the Pockels cell with the AODs creates independent arrays of optical tweezers in the two planes.

A mirror (*M3*) after the AODs reflects the beam into a 1:1-telescope formed by two lenses (*L5* and *L6*, both $f = 120$ mm). A polarizing beam splitting cube (*C3*) is placed in front of the Pockels cell (Conoptics, 360-50 LA) to remove any horizontal component of the polarization introduced by the AODs. A personal computer with an analog output board (NuDAQ PCI-6208V) controls the Pockels cell. The computer also contains the synthesizer board that generates the acoustic signals for the AODs. Both boards are controlled and synchronized using a *LabVIEW* program to create independent arrays in each trapping plane. For increased speed, the *LabVIEW* program calls a *C++* program to write the data to the two boards.

After the Pockels cell and a mirror (*M4*), the lenses *L7* and *L8* ($f = 65$ and 140 mm, respectively) expand the beam to an $1/e^2$-diameter of 5.6 mm, to fill the back aperture of the ($100\times$, 1.4 NA) objective (exit pupil diameter 5.6 mm). A polarizing beam splitter cube (*C4*) splits the beam path into two separate paths. In each of these paths, the beam passes through a 1:1-telescope formed by a pair of lenses ($L9_{a,b}$ and $L10_{a,b}$, all $f = 90$ mm). The lenses $L9_{a,b}$ are positioned in a plane conjugate to the back focal plane of the upright objective. The lens $L9_a$ is mounted on an xyz-translation stage allowing displacement of the traps created in the sample with path a with respect to the traps created with path b. After recombination of the two beams at polarizing beam splitter cube *C5*, the combined beam is coupled into the microscope with the mirrors *M5*, *M6*, and lenses $L3_u$ and $L4_u$. A movement of lens $L3_u$ results in a collective displacement of the traps created with paths a and b. The lenses $L3_u$ and $L9_{a,b}$,

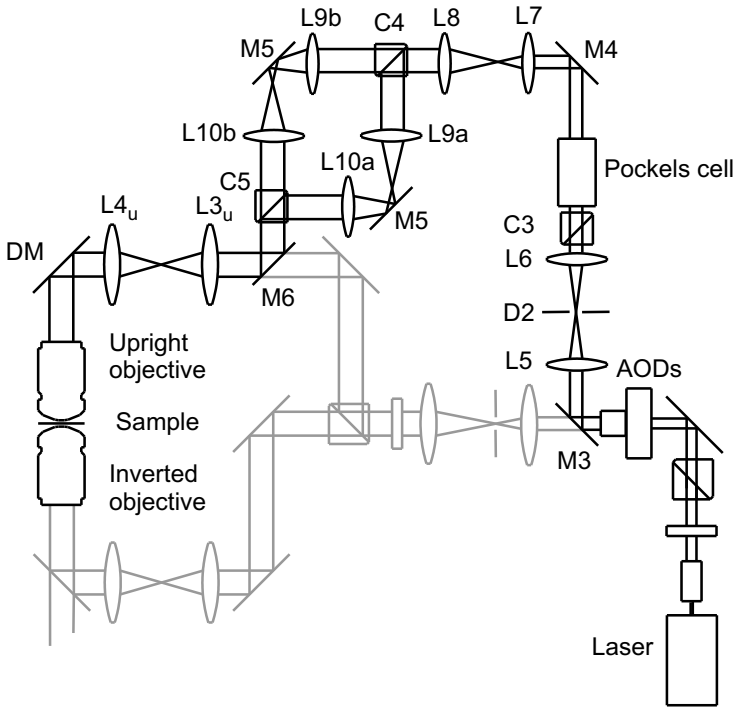

Fig. 2.2: Setup for the creation of arrays of tweezers in two trapping planes. A Pockels cell and beam splitting cubes (C4 and C5) were used to switch between the planes. The Pockels cell and the AODs were synchronized to create independent configurations of traps in each plane. The upright objective was used for trapping, while the inverted objective was used for imaging. The part of the setup drawn in light gray was not used when two trapping planes were created.

as well as the Pockels cell and the AODs, are in planes conjugate to the back focal plane of the upright objective. Because of the length of the Pockels cell (75 mm) and the small aperture (5×5 mm^2), the modulator is placed with its center at a plane conjugate to the back focal plane of the objective. The mirrors *M3* and *M6* are placed on flippers (New Focus) to move them out of the beam path when this part of the setup is not in use.

2.2.2 Imaging modes

The inverted objective is used for imaging while both the inverted and upright objectives can be used for trapping. The sample can be imaged in brightfield, differential interference contrast (DIC), epifluorescence, and reflection microscopy using mercury or halogen light sources. For DIC imaging, a polarizer and Wollaston prism are placed below the inverted objective, in addition to an analyzer

and a prism placed above the upright objective. The sample is imaged with a Charge Coupled Device (CCD) camera (UNIQ, UP-600), which is read out by a home-built frame grabber using a programmable coprocessor (SiliconSoftware, microEnable). The images (540×480 pixels, 10 bit grayscale) can be stored digitally on an array of hard disks at a rate of 20 Hz for full images and up to 50 Hz for smaller regions. For position detection in real time, the frame grabber is programmed to determine the gray-value center of mass of particles separated by at least a line of pixels on the CCD. An IR filter (Schott) is used to block the trapping beam from the CCD camera.

For confocal imaging we use a commercial confocal scan head (Leica, TCS NT) attached to the side port of the microscope. The confocal microscope excites the sample using a mixed-gas Kr/Ar laser, and the fluorescence is detected using photomultiplier tubes. To image the sample in three dimensions, either the sample is scanned using a z-scanner (Leica), or the inverted objective, mounted on the piezo microscope objective scanner operated in closed-loop mode, is scanned while the sample is kept stationary. The software of the confocal microscope controls the piezo driver electronics. For imaging of the fluorescently labeled silica particles described in the next section, the 488 nm line of the Kr/Ar laser was used in combination with cut-off filters. The silica-coated polystyrene particles were imaged in reflection mode using a second photomultiplier tube. Only in the upright trapping mode and at high powers was the trapping laser detected by the photomultiplier tubes. In that case, an IR filter in the filter wheel was used to block the trapping laser from the imaging channels that were used in the visible. Image analysis was done using routines similar to those described in Refs. [35] and [49].

2.2.3 Quadrant photodiode position detection

For quadrant photodiode (QPD) position detection of trapped particles [50, 51], the IR trapping laser light is used. The back focal plane of the upright objective can be imaged onto a QPD, which is placed in the beam path between DM_u and $L4_u$. In this scheme, however, only inverted trapping is possible. For position detection during upright or counter-propagated trapping, the small percentage of the IR light leaking through the lower dichroic mirror DM_i is imaged onto a QPD placed at the front camera port of the microscope. For simultaneous imaging onto the camera, an IR filter is placed directly in front of the camera. During QPD position detection, the objectives need to stay at a fixed distance from each other, inhibiting simultaneous 3D imaging of the sample.

2.2.4 Colloidal dispersions

Colloidal silica particles with a core-shell geometry were synthesized using the so-called Stöber growth process, modified to incorporate a fluorescent dye and

followed by a seeded growth. This method and the particle characterization are described in more detail elsewhere [52–54]. We used two sizes of silica particles with average diameters of 1384 and 1050 nm and polydispersities of 1.5% and 3%, respectively. The diameters of the silica cores were determined to be 386 and 400 nm, respectively, and the cores were labeled with the fluorescent dye fluorescein isothiocyanate (FITC). We will refer to the fluoresceine labeled silica particles as FITC-SiO_2. The ZnS particles were synthesized following a procedure described elsewhere [55], and had an average diameter of 500 nm with a polydispersity of 10%. The index of refraction of the ZnS particles was estimated [55] to be $n_D^{20} = 2.0$.

Recently, we developed a method to synthesize core-shell particles with a polystyrene core and a silica shell [56]. Polyvinyl pyrrolidone (PVP) was adsorbed onto polystyrene (PS) particles with a diameter of 772 nm (estimated refractive index $n_D^{20} = 1.6$), and then a silica shell was grown onto the PVP-coated PS particles in several growth steps. The final diameter of the particles was determined to be 975 nm with a polydispersity of less than 3%. We will refer to the polystyrene-silica core-shell particles as PS-SiO_2. The densities of the particles used are not important for the trapping experiments in this article, as the optical forces exceed the gravitational forces by far. The densities of the particles used are stated in the references cited.

The particles were dispersed in ethanol (Merck, analytical grade), dimethyl formamide (DMF) (Merck, analytical grade), or a mixture of DMF and dimethylsulfoxide (DMSO) (Merck, analytical grade). All chemicals were used as received.

In order to match the refractive index of the FITC-SiO_2 particles, we made a series of solvent mixtures with different relative composition of DMF and DMSO but with a constant concentration of silica particles. For each mixture the transmission was measured at a wavelength of 1064 nm using a spectrometer (Perkin Elmer). A mixture with a volume ratio of DMF:DMSO = 18%:82% was found to index-match the particles at 1064 nm. Using an Abbe refractometer (Atago, 3T), the refractive index of the matching mixture was measured to be $n_D^{20} = 1.4675$. For the trapping experiments on particles in a concentrated dispersion, a small amount of PS-SiO_2 particles was added to a concentrated dispersion of FITC-SiO_2 particles. The mixture was then transferred to a refractive index matching mixture of DMF and DMSO in several centrifugation (not exceeding 120 g) and redispersion steps.

In this Chapter, the samples with a thickness of 10–15 μm were made by sandwiching a drop of dispersion between a larger and a smaller microscope cover slide (Chance or Menzel, No. 1, thickness 170 μm). The samples were sealed with candle wax. Thin samples were clamped on all sides to prevent them from bending when the objectives were moved. Thicker samples consisted of $0.1 \times 2 \times 50$ mm^3 capillaries (VitroCom, wall thickness 100 μm), which were

closed by melting. The optical quality of the microscope cover slides is better than that of the capillaries.

2.3 Dynamic arrays of optical tweezers

Figure 2.3 shows an array of 20×20 time-shared optical traps holding 1.4-μm-diameter FITC-SiO_2 particles. The inverted objective (63×; 1.4 NA) was used for trapping as well as for imaging. The AODs scanned the array at a frequency of 96 Hz. The particles were dispersed in ethanol in a 100-μm-thick capillary. The tweezers array was shifted up slightly with respect to the imaging plane. The untrapped particles next to the array were situated just below the imaging plane. Some traps held more than one particle, while several traps on the edge of the pattern were not filled. The total laser power used to create the 400 traps was 1.0 W at the back focal plane of the trapping objective.

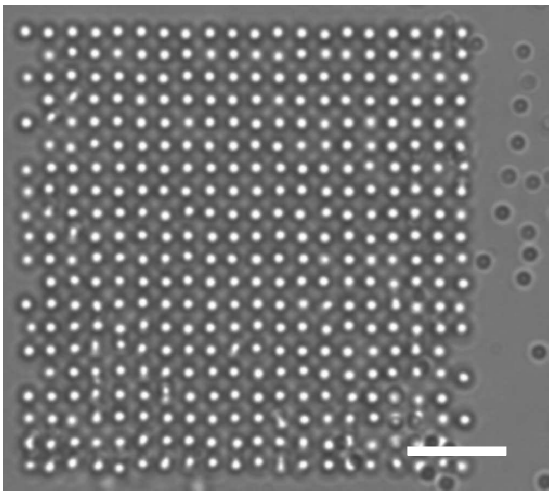

Fig. 2.3: Transmission microscopy image of 1.4-μm-diameter FITC-SiO_2 particles in ethanol, trapped in an array of 400 time-shared optical traps. The inverted objective was used for trapping as well as for imaging. Using the AODs, the array was scanned at 96 Hz, well above the roll-off frequency of the particles in the traps. The particles on the right of the image were not trapped, and were located below the imaging plane. The scale bar is 10 μm.

When time-sharing a laser beam, the beam has to be scanned fast enough over the different positions in the sample for a particle to behave like it would when trapped in a non-time-shared optical trap. To determine the necessary speed, we measured, using a QPD, the roll-off frequency f_c to be 10 Hz for a 1.4-μm-diameter silica particle trapped in a single optical trap with 2.5 mW laser power at the back focal plane of the trapping objective. This is well below

the 96 Hz at which the array in Figure 2.3 was scanned. Already hundreds of traps can be created by time-sharing the AODs in a low viscosity solvent like ethanol for micron-size particles; increasing the viscosity, and thus lowering f_c, would allow for even larger arrays. However, to keep a particle trapped, the particle should not be able to wander too far from the central trap position during the *off*-time of that trap. Also, the *on*-time of the time-shared trap should be long enough to bring the particle back to the central position. This sets a limit to the *on*/*off*-ratio of each trap, and as a consequence, to the number of traps that can be created. This *on*/*off*-ratio is independ of the viscosity of the medium, but a higher trap stiffness will increase the number of possible traps. Both considerations have to be taken into account in setting the time-sharing frequency and/or the number of traps in the array.

Figure 2.4a shows 25 FITC-SiO_2 particles (1.4-μm-diameter) dispersed in ethanol and trapped in a 5×5 square symmetric pattern using the inverted microscope objective (100×; 1.4 NA). The pattern was then changed in a few seconds, without losing particles from the trap, via intermediate stages (Figure 2.4b and c) into the triangular pattern shown in Figure 2.4d.

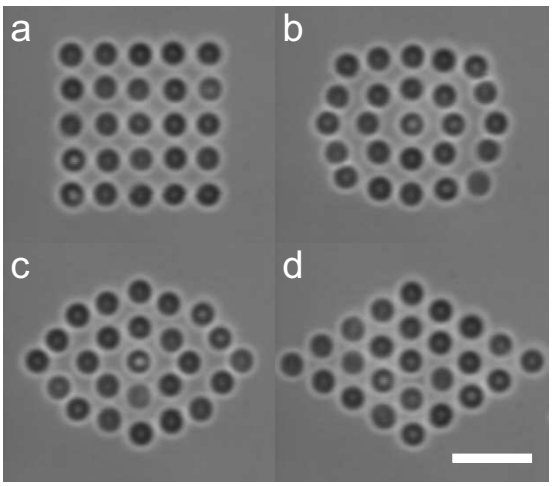

Fig. 2.4: (a) Transmission microscopy image of 1.4-μm-diameter FITC-SiO_2 particles trapped in an array of 25 time-shared optical traps with squared symmetry. The inverted objective was used for trapping as well as for imaging. Using the AODs, the pattern was dynamically changed in a few seconds without losing particles, via intermediate patterns (b) and (c) to an array with triangular symmetry (d). The scale bar is 5 μm.

Compared to other techniques of time-sharing optical tweezers, for example scanning mirrors [16], AODs are fast and flexible. Even mirrors mounted on piezo scanners [17] have a scan rate of no more than a few kHz, while the

AODs can be used at more than 100 kHz. Other techniques that intensity-share the beam, like diffractive optical elements [18, 19] in combination with computer addressed spatial light modulators [20, 21], are very flexible, although their computational process is complex and time-consuming. Multiple tweezers generated with the generalized phase contrast method [24] are much faster than holographic optical tweezers, but they only trap in two dimensions.

The AODs can also be used to create multiple tweezers without time-sharing the laser beam. We used digital synthesizers to generate two frequency signals, which were combined as input for one of the AODs, while the other AOD had a single frequency as input. The laser beam was diffracted at two different angles, creating two optical traps in the sample. Arrays of tweezers are possible using this approach, although the intensities of the beams are interrelated, and higher-order frequencies might appear.

2.4 Optical trapping and decoupled confocal imaging

The use of two microscope objectives, one on each side of the sample, allows for optical trapping and simultaneous three-dimensional imaging in the sample. To demonstrate this independent trapping and imaging, we created a three-dimensional structure of colloidal particles. On the setup, the upright objective (100×; 1.4 NA) was used to create an array of eight optical traps. Each trap was filled with two 1.4-μm-diameter FITC-SiO_2 particles. The pairs of particles in each trap were distributed along the propagation direction of the beam and formed a three-dimensional structure. This method was demonstrated – although not by imaging in three dimensions – by MacDonald and co-workers [23]. Using the inverted objective (63×; 1.4 NA), we imaged the sample in confocal mode. Starting below the structure and ending above it, we scanned through the two layers of particles.

Figure 2.5a shows a plane below the structure with almost no fluorescence signal detected. Moving upwards, the eight particles in the lower plane were imaged (Figs. 2.5b and c). Between the two planes of particles (Figs 2.5d and e) some fluorescence was detected. Moving further upwards, the particles in the second layer were imaged (Fig. 2.5f). Finally, Figure 2.5h shows a plane just above the structure. Because the particles have a fluorescent core and a non-fluorescent shell, only the cores were imaged. The separation between the imaging planes in Figure 2.5 was determined to be 546 nm [57]. From the confocal images we determined the three-dimensional coordinates of the particles, which we used to computer-generate an image of the structure created by the optical traps (Figure 2.5i).

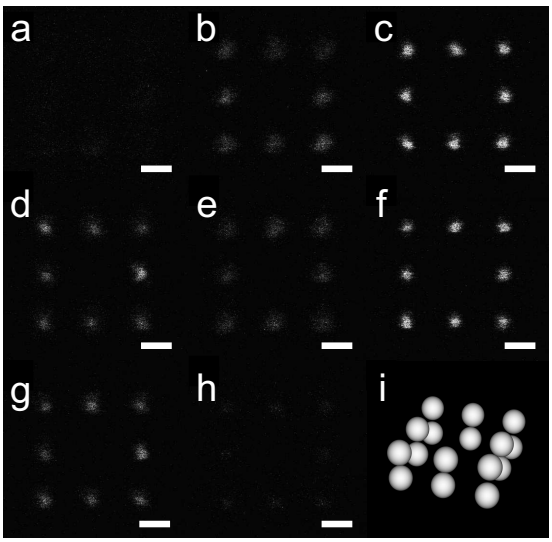

Fig. 2.5: (a)-(h) Fluorescence confocal images of a three-dimensional structure of colloidal particles created with a two-dimensional array of time-shared optical tweezers. Eight time-shared optical traps held two 1.4-µm-diameter FITC-SiO_2 particles each. The particles aligned on top of each other in the propagation direction of the laser beam. The height difference between each subsequent image was 546 nm with (a) below and (h) above the structure. The upright objective was used for trapping, while the inverted objective was used for imaging. Only the fluorescent cores of the particles were imaged and image (i) was computer-generated after determination of the particle coordinates from the confocal images. The scale bars are 2 µm.

2.5 Arrays of tweezers in more than one plane using one objective

Using the setup as described in Section 2.2.1, we created two trapping planes using the upright objective (100×; 1.4 NA). In each plane, a different configuration of traps was created by synchronizing the Pockels cell and the AODs. This three-dimensional array was then filled with 1.4-μm-diameter FITC-SiO_2 particles. The particles were dispersed in ethanol in a 10-μm-thick sample. The lower objective (100×; 1.4 NA) was used for imaging. Figure 2.6a shows a confocal image of the upper plane in which six particles were trapped, while the nine particles in the lower plane are shown in Figure 2.6b. The distance between the trapping planes was determined to be 1.7 μm [57]. When the confocal microscope was focused between the two trapping planes, fluorescence from both the upper and the lower plane was visible (Figure 2.6c). From the confocal images we determined the position coordinates of the particles in the trapping array and generated an artificial image of the three-dimensional structure created (Figure 2.6d).

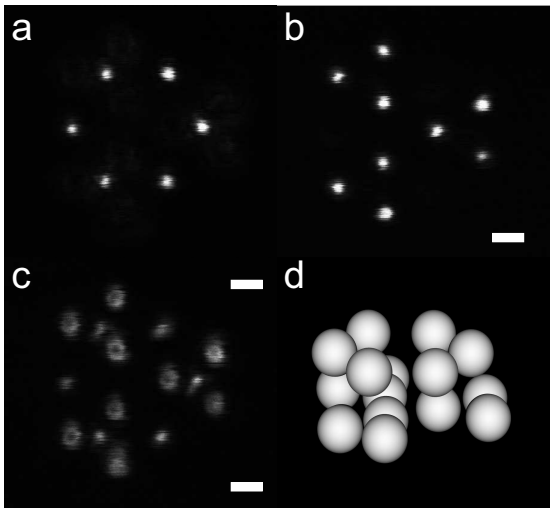

Fig. 2.6: Fluorescence confocal images of particles trapped in a three-dimensional array of tweezers created by synchronizing the Pockels cell and the AODs. (a) Six particles were trapped in the upper plane and (b) nine in the lower plane. (c) Between the two trapping planes fluorescence from particles in both planes was detected. The height difference between the two trapping planes was 1.7 μm. The upright objective was used for trapping while the inverted objective was used for imaging. The 1.4-μm-diameter FITC-SiO_2 particles were dispersed in ethanol, and only their fluorescent cores were imaged. (d) An image was computer generated on the basis of the confocal data. The scale bars are 1 μm.

2.6 Manipulation of (core-shell) particles in a concentrated dispersion

To demonstrate selective optical trapping in a concentrated dispersion, we dispersed a mixture of PS-SiO_2 and FITC-SiO_2 particles in a solvent mixture of DMF and DMSO with the same refractive index as SiO_2 at 1064 nm. The diameters of the particles were 975 and 1050 nm, respectively. The concentration of the samples was chosen such that, after the dispersion had sedimented in the 100-μm-thick capillary, a thin sediment formed, which was either liquid-like or crystalline in the bottom layer. We created a 3×3 square array of optical tweezers, with varying spacings between the traps, in the bottom layer of the dispersion. Eight traps were filled with PS-SiO_2 particles, and one trap was left empty. The upright objective (63×; 1.4 NA) was used for trapping, while the inverted objective (100×; 1.4 NA) was used for imaging.

Figure 2.7 shows combined fluorescence and reflection confocal images of the eight trapped particles surrounded by non-trappable FITC-SiO_2 particles. The

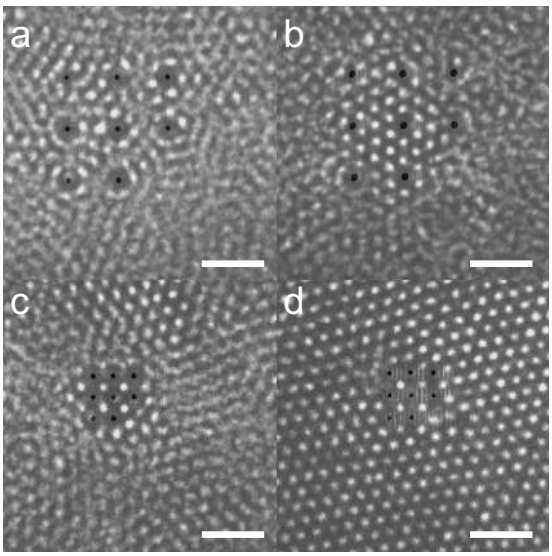

Fig. 2.7: Combined confocal and fluorescence images of a mixture of PS-SiO_2 (black) and FITC-SiO_2 particles (light gray). The mixture was dispersed in a fluid matching the refractive index of the FITC-SiO_2 particles. The PS-SiO_2 particles were trapped in a 3×3 array of optical tweezers. The upright objective was used for imaging. The lattice spacing of the templates was (a) 4.1 μm, (b) 4.1 μm, (c) 1.6 μm, and (d) 1.8 μm. The template of trapped particles induced structure in the dispersion of FITC-SiO_2 particles. Images were averaged over (a) 20, (b) 10, (c) 10, and (d) 4 images with 1.7 s between the frames. Immobile particles were imaged sharply, while moving particles became blurred. Only the cores of the particles were imaged. Note that only eight of the nine traps were occupied and that no FITC-SiO_2 particles are drawn towards, nor expelled from, the empty trap, demonstrating that optical forces on these particles are negligible. The scale bars are 5 μm.

trapped particles are displayed in black, while the FITC-SiO_2 particles are displayed in light gray. The images were averaged over multiple frames with a time step of 1.7 s between the frames. Because of the averaging, mobile particles were blurred in the images, while particles that were not moving were imaged sharply. Figure 2.7a was averaged over 20 images and shows an open structure with a separation between the traps of 4.1 μm. The concentration of the surrounding FITC-SiO_2 particles was below the freezing point, and they were thus in the liquid state. Within the array of trapped particles, the FITC-SiO_2 particles showed some ordering, but did not crystallize. Figure 2.7b (averaged over ten frames) shows an array with the same trap separation as in Figure 2.7a, but here the FITC-SiO_2 spheres crystallized with a hexagonal symmetry within the array of trapped particles. The particles surrounding the array were still clearly liquid-

like. Figures 2.7c and d (averaged over ten and four frames, respectively) show arrays with smaller trap separations of 1.6 and 1.8 μm. In Figure 2.7c, FITC-SiO_2 spheres penetrate the array of PS-SiO_2 particles, resulting in an ordered structure with square symmetry, while the surrounding FITC-SiO_2 spheres were still liquid-like. Figure 2.7d shows that also in a crystalline layer the PS-SiO_2 particles can be trapped in an array that is incommensurate with the crystal lattice. The hexagonal layer incorporated the different symmetry of the trapped structure, although some defect lines originate from the trapped structure. At the position of the empty trap in the 3×3 array can be seen that the force on the FITC-SiO_2 particles was negligible compared to their thermal energy. If the FITC-SiO_2 particles were either under- or over-matched by the solvent mixture, the optical forces on these particles would either pull them towards or expel them from the trap.

The high-index core of the PS-SiO_2 particles allowed them to be manipulated in a concentrated dispersion of refractive index-matched FITC-SiO_2 particles. The core-shell morphology of the PS-SiO_2 particles has several other advantages. Because the shell of the core-shell particles is of the same material as the FITC-SiO_2 particles, all particles in the mixture have the same surface properties and thus the same interparticle interaction. Furthermore, the optically induced forces, present between non-time-shared multiple trapped particles, will be decreased, as only the cores are trapped, and these forces decay strongly with interparticle distance [22, 58]. Finally, the core-shell geometry is advantageous for trapping in three-dimensional arrays of optical traps (as in Sections 2.4 and 2.5) as the scattering unit of a particle is smaller, thus causing less distortion of the laser field behind the particle.

2.7 Counter-propagating tweezers

Counter-propagating optical tweezers1 [48], have the advantage over single beam traps in that they can trap strongly scattering particles. The scattering force on a particle is cancelled due to symmetry of the two beams along the optical axis. At the same time, the gradient force is added resulting therefore in stronger confinement of the particle in all directions compared to a single-beam trap.

To demonstrate such a counter-propagating trap, we trapped a 0.5-μm-diameter ZnS particle ($n_D^{20} = 2.0$) dispersed in ethanol. The large difference in refractive index meant that the particle could not be trapped in a conventional single-beam gradient trap. Figure 2.8a shows on the left the ZnS particle in a counter-propagating trap. The trap was created using both the inverted and upright objective (both 100×; 1.4 NA), and the laser power was divided equally between both beam paths. The particle on the right in Figure 2.8a is a 1.4-μm-diameter FITC-SiO_2 particle stuck to the lower sample wall. To demonstrate that the ZnS particle was indeed trapped in three dimensions in

the counter-propagating trap, we moved the stage down in Figures 2.8b and c As can be seen, the ZnS particle stayed in focus while the FITC-SiO_2 particle moved out of focus. It was possible to shift the position of the ZnS particle with respect to the imaging plane by changing the relative power in the upright and inverted beam paths.

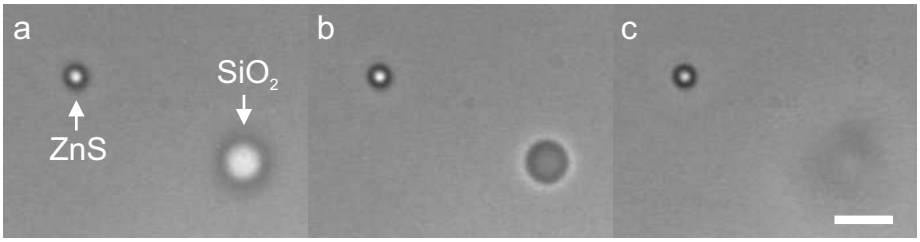

Fig. 2.8: A 0.5-µm-diameter ZnS particle (left) trapped in counter-propagating optical tweezers next to a 1.4-µm-diameter FITC-SiO_2 particle (right) that was stuck to the surface of the sample cell. The ZnS particle was trapped in three dimensions, as can be seen in (b) and (c), where the sample was moved down with respect to the trapping plane; the ZnS particle was trapped and therefore stayed in focus, while the FITC-SiO_2 particle moved out of the focal plane. It was not possible to trap the ZnS particle using single-beam optical tweezers. The scale bar is 2 µm.

2.8 Discussion and outlook

The setup described in this Chapter was developed to both manipulate and image individual colloidal particles in three dimensions in concentrated colloidal dispersions. We have shown that the combination of confocal microscopy and time-shared optical tweezers allows independent three-dimensional imaging and manipulation of the dispersion.

By choosing AODs to time-share the laser beam we have shown that it is possible to create large arrays of hundreds of optical traps and change them dynamically, due to the high scan rate of the AODs. These arrays of tweezers were used to create two-dimensional and three-dimensional structures of particles. Arrays of traps in two planes were created using a Pockels cell combined with polarizing beam splitters. Such an approach does not enable full three-dimensional control over the trapped particles, but is one of the fastest methods to create and dynamically change the symmetry of two independent two-dimensional arrays of optical tweezers.

In addition, we have shown that selective trapping and manipulation of individual particles is possible if a concentrated system of a mix of index-matched and non-matched particles is used. The non-matched particles can be trapped

and manipulated without exerting forces on the index-matched particles. Because both species have an index-matched shell, all particles in the mixture have the same surface properties. By fluorescently labeling the (cores of the) particles, it is possible to follow the effects of the trapped spheres on the bulk dispersion on a single particle level in three dimensions.

In combination with the use of the earlier mentioned arrays of tweezers we plan to study crystal nucleation. With our setup, the umbrella-sampling scheme that uses a local potential to probe unlikely events such as crystal nucleation in computer simulations [59], can now be implemented experimentally.

Finally, by using counter-propagating traps, high-refractive index particles could be manipulated that could not be trapped in three dimensions with conventional single-beam optical tweezers.

Acknowledgements

The major part of the work in this Chapter is published in Ref. [60], to which Dirk L.J. Vossen and I contributed equally. I would like to acknowledge Dirk Vossen for synthesis of the core-shell particles, Krassimir Velikov for the ZnS particles, and Jacob Hoogenboom for the silica particles. I am grateful to Koen Visscher for the opportunity to develop the trapping in two planes in his lab at the University of Arizona, from November 2001 until March 2002.

BIBLIOGRAPHY

[1] A. Ashkin. Acceleration and trapping of particles by radiation pressure. *Phys. Rev. Lett.*, 24(4):156–159, 1970.

[2] A. Ashkin. Observation of a single-beam gradient force optical trap for dielectric particles. *Opt. Lett.*, 11(5):288–290, 1986.

[3] K. Visscher, S. P. Gross, and S. M. Block. Construction of multiple-beam optical traps with nanometer-resolution position sensing. *IEEE J. Sel. Top. Quant. Electronics*, 2(4):1066–1076, 1996.

[4] D. G. Grier. Optical tweezers in colloid and interface science. *Curr. Opin. Colloid Interface Sci.*, 2:264–270, 1997.

[5] K. Dholakia, G. Spalding, and M. MacDonald. Optical tweezers: the next generation. *Phys. World*, 15:31–35, 2002.

[6] D. G. Grier. A revolution in optical manipulation. *Nature*, 424:810–816, 2003.

[7] P. A. Maia Neto and H. M. Nussenzveig. Theory of optical tweezers. *Europhys. Lett.*, 50(5):702–708, 2000.

[8] Y. Harada and T. Asakura. Radiation forces on a dielectric sphere in the Rayleigh scattering regime. *Opt. Commun.*, 124:529–541, 1996.

[9] A. Ashkin. Forces of a single-beam gradient laser trap on a dielectric sphere in the ray optics regime. *Methods in Cell Biology*, 55:1–27, 1998.

[10] K. Sasaki, M. Koshioka, H. Misawa, N. Kitamura, and H. Masuhara. Optical trapping of a metal particle and a water droplet by a scanning laser beam. *Appl. Phys. Lett.*, 60(7):807–809, 1992.

[11] H. He, M. E. J. Friese, N. R. Heckenberg, and H. Rubinsztein-Dunlop. Direct observation of transfer of angular momentum to absorptive particles from a laser beam with a phase singularity. *Phys. Rev. Lett.*, 75(5):826–829, 1995.

[12] K. Visscher and G. J. Brakenhoff. Micromanipulation by "multiple" optical traps created by a single fast scanning trap integrated with the bilateral confocal scanning laser microscope. *Cytometry*, 14(2):105–114, 1993.

[13] M. E. J. Friese, T. A. Nieminen, and N. R. Heckenberg. Optical alignment and spinning of laser-trapped microscopic particles. *Nature*, 394:348–350, 1998.

[14] L. Paterson, M. P. MacDonald, J. Arlt, W. Sibbett, P. E. Bryant, and K. Dholakia. Controlled rotation of optically trapped microscopic particles. *Science*, 292:912–914, 2001.

[15] J. Guck, R. Ananthakrishnan, T. J. Moon, C. C. Cunningham, and J. Käs. Optical deformability of soft biological dielectrics. *Phys. Rev. Lett.*, 84(23):5451–5454, 2000.

[16] K. Sasaki, M. Koshioka, H. Misawa, N. Kitamura, and H. Masuhara. Pattern formation and flow control of fine particles by laser-scanning micromanipulation. *Opt. Lett.*, 16(19):1463–1465, 1991.

[17] C. Mio, T. Gong, A. Terray, and D. W. M. Marr. Design of a scanning laser optical trap for multiparticle manipulation. *Rev. Sci. Instrum.*, 71(5):2196–2200,

2000.

[18] J.-M. Fournier, M. M. Burns, and J. A. Golovchenko. Writing diffractive structures by optical trapping. *Proc. SPIE*, 2406:101–111, 1995.

[19] E. R. Dufresne and D. G. Grier. Optical tweezer arrays and optical substrates created with diffractive optics. *Rev. Sci. Instrum.*, 69(5):1974–1977, 1998.

[20] Y. Hayasaki, M. Itoh, T. Yatagai, and N. Nishida. Nonmechanical optical manipulation of microparticle using spatial light modulator. *Opt. Rev.*, 6:24–27, 1999.

[21] J. Liesener, M. Reicherter, T. Haist, and H. J. Tiziani. Multi-functional optical tweezers using computer-generated holograms. *Opt. Commun.*, 185:77–82, 2000.

[22] M. M. Burns, J.-M. Fournier, and J. A. Golovchenko. Optical matter: Crystallization and binding in intense optical fields. *Science*, 249(4970):749–754, 1990.

[23] M. P. MacDonald, L. Paterson, K. Volke-Sepulveda, J. Arlt, W. Sibbett, and K. Dholakia. Creation and manipulation of three-dimensional optically trapped structures. *Science*, 296:1101–1103, 2002.

[24] R. L. Eriksen, P. C. Mogensen, and J. Glückstad. Multiple-beam optical tweezers generated by the generalized phase-contrast method. *Opt. Lett.*, 27(4):267–269, 2002.

[25] M. Minsky. Microscopy apparatus. *U.S. Patent No. 301467*, 1961.

[26] J. K. Stevens, L. R. Mills, and J. E. Trogadis. *Three-dimensional Confocal Microscopy: Volume Investigation of Biological Systems*. Academic, San Diego, CA, 1994.

[27] M. H. Chestnut. Confocal microscopy of colloids. *Curr. Opin. Colloid Interface Sci.*, 2:158–161, 1997.

[28] A. van Blaaderen. Quantitative real-space analysis of colloidal structures and dynamics with confocal scanning light microscopy. *Prog. Colloid Polym. Sci.*, 104:59–65, 1997.

[29] A. D. Dinsmore, E. R. Weeks, V. Prasad, A. C. Levitt, and D. A. Weitz. Three-dimensional confocal microscopy of colloids. *Appl. Opt.*, 40(24):4152–4159, 2001.

[30] J. B. Pawley. *Handbook of Biological Confocal Microscopy*. Plenum, New York, 1995.

[31] A. van Blaaderen, K. P. Velikov, J. P. Hoogenboom, D. L. J. Vossen, A. Yethiraj, R. P. A. Dullens, T. van Dillen, and A. Polman. *Photonic crystals and light localization in the 21st century*, pages 239–251. Edited by C. M. Soukoulis (Kluwer, Dordrecht), 2001.

[32] M. Brunner, C. Bechinger, W. Strepp, V. Lobaskin, and H. H. von Grünberg. Density-dependent pair interactions in 2D colloidal suspensions. *Europhys. Lett.*, 58(6):926–932, 2002.

[33] A. van Blaaderen, J. P. Hoogenboom, D. L. J. Vossen, A. Yethiraj, A. van der Horst, K. Visscher, and M. Dogterom. Colloidal epitaxy: playing with the boundary conditions of colloidal crystallization. *Faraday Discussions*, 123:107–119, 2003.

[34] A. Yethiraj and A. van Blaaderen. A colloidal model system with an interaction tunable from hard sphere to soft and dipolar. *Nature*, 421:513–517, 2003.

[35] A. van Blaaderen and P. Wiltzius. Real-space structure of colloidal hard-sphere glasses. *Science*, 270:1177–1179, 1995.

[36] W. K. Kegel and A. van Blaaderen. Direct observation of dynamical heterogeneities in colloidal hard-sphere suspensions. *Science*, 287:290–293, 2000.

[37] U. Gasser, E. R. Weeks, A. Schofield, P. N. Pusey, and D. A. Weitz. Real-space imaging of nucleation and growth in colloidal crystallization. *Science*, 292:258–

262, 2001.

[38] J. P. Hoogenboom, D. L. J. Vossen, C. Faivre-Moskalenko, M. Dogterom, and A. van Blaaderen. Patterning surfaces with colloidal particles using optical tweezers. *Appl. Phys. Lett.*, 80(25):4828–4830, 2002.

[39] D. L. J. Vossen, J. P. Hoogenboom, K. Overgaag, and A. van Blaaderen. Building two and three-dimensional structures of colloidal particles on surfaces using optical tweezers and critical point drying. *Materials Research Society Symposium Proceedings, edited by L. Merhari, Boston*, 705:y6.8.1–6.8.6, 2002.

[40] J. C. Crocker and D. G. Grier. Microscopic measurement of the pair interaction potential of charged-stabilized colloid. *Phys. Rev. Lett.*, 73(2):352–355, 1994.

[41] J. C. Crocker, J. A. Matteo, A. D. Dinsmore, and A. G. Yodh. Entropic attraction and repulsion in binary colloids probed with a line optical tweezer. *Phys. Rev. Lett.*, 82(21):4352–4355, 1999.

[42] S. Henderson, S. Mitchell, and P. Bartlett. Position correlation microscopy: probing single particle dynamics in colloidal suspensions. *Colloids and Surfaces A*, 190:81–88, 2001.

[43] P. T. Korda and D. G. Grier. A colloidal model system with an interaction tunable from hard sphere to soft and dipolar. *J. Chem. Phys.*, 114(17):7570–7573, 2001.

[44] J. Leach, G. Sinclair, P. Jordan, J. Courtial, and M. J. Padgett. 3D manipulation of particles into crystal structures using holographic optical tweezers. *Opt. Express*, 12(1):220–226, 2004.

[45] A. Resnick. Design and construction of a space-borne optical tweezer apparatus. *Rev. Sci. Instrum.*, 72(11):4059–4065, 2001.

[46] A. Hoffmann, G. M. Z. Hörste, G. Pilarczyk, S. Monajembashi, V. Uhl, and K. O. Greulich. Optical tweezers for confocal microscopy. *Appl. Phys. B*, 71(5):747–753, 2000.

[47] K. Visscher and G. J. Brakenhoff. Single beam optical trapping integrated in a confocal microscope for biological applications. *Cytometry*, 12(6):486–491, 1991.

[48] S. B. Smith, Y. Cui, and C. Bustamante. Overstretching B-DNA: the elastic response of individual double-stranded and single-stranded DNA molecules. *Science*, 271:795–799, 1996.

[49] J. C. Crocker and D. G. Grier. Methods of digital video microscopy for colloidal studies. *J. Colloid Interface Sci.*, 179:298–310, 1996.

[50] M. W. Allersma, F. Gittes, M. J. deCastro, R. J. Stewart, and C. F. Schmidt. Two-dimensional tracking of ncd motility by back focal plane interferometry. *Biophys. J.*, 74:1074–1085, 1998.

[51] F. Gittes and C. F. Schmidt. *Signals and noise in micromechanical measurements*, volume 55, pages 129–156. Edited by M. P. Sheetz (Academic, San Diego), 1998.

[52] A. van Blaaderen and A. Vrij. Synthesis and characterization of colloidal dispersions of fluorescent, monodisperse silica spheres. *Langmuir*, 8(12):2921–2931, 1992.

[53] N. A. M. Verhaegh and A. van Blaaderen. Dispersions of rhodamine-labeled silica spheres: synthesis, characterization, and fluorescence confocal scanning laser microscopy. *Langmuir*, 10(5):1427–1438, 1994.

[54] H. Giesche. Synthesis of monodispersed silica powders II. Controlled growth reaction and continuous production process. *J. Eur. Ceram. Soc.*, 14(3):205–214, 1994.

[55] K. P. Velikov and A. van Blaaderen. Synthesis and characterization of monodisperse core-shell colloidal spheres of zinc sulfide and silica. *Langmuir*, 17(16):4779–

4486, 2001.

[56] C. Graf, D. L. J. Vossen, A. Imhof, and A. van Blaaderen. A general method to coat colloidal particles with silica. *Langmuir*, 19(17):6693–6700, 2003.

[57] S. W. Hell and E. H. K. Stelzer. *Lens aberrations in confocal fluorescence microscopy*, pages 347–353. Edited by J. B. Pawley (Plenum Press, New York and London), 1995.

[58] M. I. Antonoyiannakis and J. B. Pendry. Mie resonances and bonding in photonic crystals. *Europhys. Lett.*, 40(6):613–618, 1997.

[59] S. Auer and D. Frenkel. Prediction of absolute crystal-nucleation rate in hard-sphere colloids. *Nature*, 409:1020–1023, 2001.

[60] D. L. J. Vossen, A. van der Horst, M. Dogterom, and A. van Blaaderen. Optical tweezers and confocal microscopy for simultaneous three-dimensional manipulation and imaging in concentrated colloidal dispersions. *Rev. Sci. Instrum.*, 75(9):2960–2970, 2004.

3. SPHERICAL ABERRATIONS DUE TO REFRACTIVE-INDEX MISMATCH — INFLUENCE ON OPTICAL TRAPPING AND CONFOCAL IMAGING

When there is a refractive index mismatch between the immersion fluid and the specimen, the focal depth of a light ray focused by a microscope objective, depends on the radial distance of this ray to the optical axis. As a result, the point spread function is distorted. Due to these so-called spherical aberrations, the width of the focus increases and the maximum intensity decreases, for increasing focal depth. In addition, the actual focus position is moved along the optical axis. The effects on confocal imaging and on optical trapping are manifold, including a decrease in image resolution and in trap stiffness for increasing depth; these effects are more pronounced in the axial than in the lateral direction. Furthermore, when confocal data are used to reconstruct 3D configurations, the axial scaling has to be taken into account. In this Chapter, we discuss the effects of spherical aberrations on confocal imaging and optical trapping. As a demonstration, we determined the axial scaling factor for an oil immersion objective in ethanol by using a particle with two fluorescently-labeled cores as an in situ *measuring stick. We used the results to make a reconstruction of the 3D configuration of three particles in a single beam trap.*

3.1 Introduction

The effects of a difference between the index of refraction n_1 of the immersion fluid and the index n_2 of the specimen are of interest in quantitative three-dimensional (3D) light microscopy, such as confocal microscopy and two-photon excitation microscopy. Due to the refractive-index contrast — for example when using an oil immersion objective in water — the focal depth of a light ray of a laser beam focused by a microscope objective depends on the radial distance of this ray to the optical axis. As a consequence, the point spread function (PSF) of the focus is distorted [1–4], introducing spherical aberrations. For increasing depth in the sample, the axial and lateral resolution are degraded and the detected light intensity is decreased. In addition, the position of the focus is shifted [5, 6], causing axial distances to be either overestimated (for $n_1 > n_2$) or underestimated (for $n_1 < n_2$). This scaling in the axial direction is of specific importance when microscopy data is used for three-dimensional (3D) reconstruction of scanned objects [7–9]. Various methods have been explored to minimize the distortion of the PSF due to spherical aberrations, for example by changing the illumination beam to compensate for spherical aberrations [3], or by deconvolution restoration of the image afterwards [4].

In the field of optical trapping, spherical aberrations due to a refractive-index mismatch have recently attracted an increasing amount of attention [10–13]. As a consequence of the depth dependence of the PSF distortion, the trap stiffness in both axial and radial direction depend on the trapping depth in the sample. The possibilities to correct for spherical aberrations in trapping have been investigated. In these cases, the input beam was altered using a deformable mirror [12, 14], or by changing the tube length by inserting extra lenses in the optical path of the laser [10, 15]. Several groups have investigated the effect of spherical aberrations on the trap stiffness, in the lateral direction [10], the axial direction [11], or both [13, 16]. When not taken into account in calculations [17, 18], spherical aberrations are a source of discrepancy between calculations and measurements.

Three-dimensional configurations of multiple particles in optical traps are of interest in creating extended 3D structures of colloidal particles [19]. Such structures can be used as a nucleus to induce colloidal crystallization [20]. When trapping multiple particles in close proximity to each other, the trapping positions will be influenced by the other particles and other trapping beams. For example, Gauthier and Ashman [21] used an enhanced ray optics approach to calculate configurations of multiple particles in a trap, and showed for certain particle sizes and index contrast conditions, that three particles will not all three be trapped exactly on the beam axis. Such deviations are of importance in creating 3D structures, and can be studied by 3D imaging of trapped structures. The optical sectioning ability of confocal microscopy offers the pos-

sibility to determine the 3D particle coordinates for reconstruction of their 3D configuration [22]. However, care has to be taken in the analysis of particle coordinates [23].

In this Chapter, we use geometric optics (GO) to derive a simple representation of the origin of spherical aberrations, and we discuss the influence of these aberrations on optical trapping, as well as on confocal imaging. As a demonstration, we measured the axial scaling due to spherical aberrations when using an oil-immersion objective for confocal fluorescence microscopy in ethanol, exploiting a particle with two fluorescently labeled cores as an *in situ* measuring stick. The results were used to determine the 3D configuration of three fluorescently-labeled particles in a single optical trap.

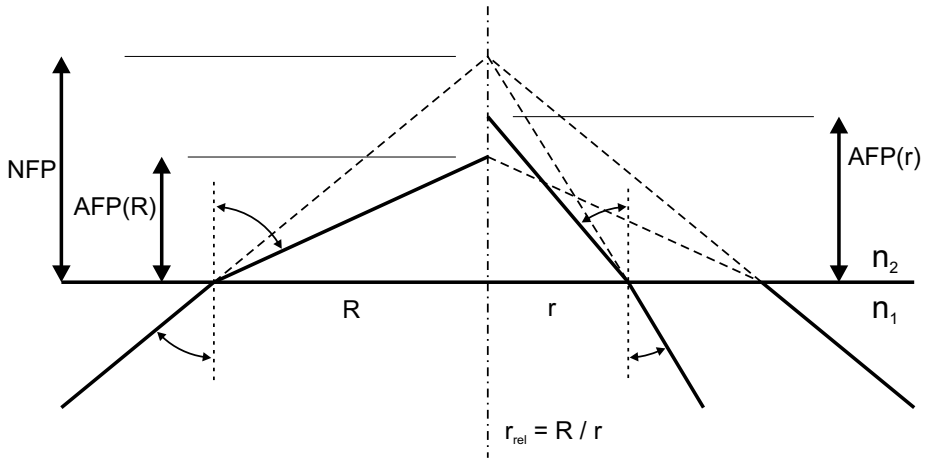

Fig. 3.1: Geometric optics representation of the refraction of a light beam focused through a refractive index interface with $n_2 < n_1$. The actual focus position (AFP) compared to the nominal focal position (NFP) of a ray depends on the distance $0 < r < R$ to the optical axis, introducing spherical aberrations of the point spread function of the focus. R is the radial distance of the outer rays at the interface.

3.2 Spherical aberrations

High-numerical aperture (NA) objectives used in microscopy are designed for use in a medium with a certain refractive index n_1; only then does the light focus to a diffraction-limited spot, with the opening angle θ_1 of the beam given by:

$$\theta_1 = \arcsin\left(\frac{\mathrm{NA}}{n_1}\right). \tag{3.1}$$

In the case of a mismatch in refractive index n_1 of the immersion fluid and the index n_2 of the specimen, the light is refracted at the interface (see Figure 3.1). For each light ray, the angle of refraction ϑ_2 depends on the angle of incidence ϑ_1, and Snell's law of refraction describes this dependence as:

$$n_1 \sin \vartheta_1 = n_2 \sin \vartheta_2. \tag{3.2}$$

We will use geometric optics (GO) to determine the actual focal position (AFP) for certain nominal focal position (NFP); the NFP is equivalent to the depth of focus when no refraction occurs. It should be noted that GO is too simple a theory to describe the PSF of a laser beam focused by a high-numerical aperture objective, with or without spherical aberrations. Here, however, we will use the theory to gain understanding of the origin of spherical aberrations due to a refractive-index mismatch, and to get a first approximation of how these aberrations affect the position and shape of the PSF.

Because the absolute radial distance r of a ray at the interface depends on the NFP, we express the AFP as a function of the relative radial distance $r_{\mathrm{rel}} = r/R$:

$$\mathrm{AFP}(r_{\mathrm{rel}}) = \frac{r_{\mathrm{rel}} R}{\tan \vartheta_2}, \tag{3.3}$$

with, using Eq. (3.2), the angle of refraction ϑ_2 given by:

$$\vartheta_2(r_{\mathrm{rel}}) = \arcsin\left(\frac{n_1}{n_2} \sin \vartheta_1\right), \tag{3.4}$$

and the angle of incidence ϑ_1 by:

$$\vartheta_1(r_{\mathrm{rel}}) = \arctan\left(\frac{r_{\mathrm{rel}} R}{\mathrm{NFP}}\right). \tag{3.5}$$

The expression (3.3) for the actual focus position can now be rewritten to:

$$\mathrm{AFP}(r_{\mathrm{rel}}) = \frac{r_{\mathrm{rel}} R}{\tan\left(\arcsin\left(\frac{n_1}{n_2} \sin\left(\arctan\left(\frac{r_{rel} R}{\mathrm{NFP}}\right)\right)\right)\right)}. \tag{3.6}$$

For the maximum radius R of the light cone at the interface, we find:

$$R = \mathrm{NFP} \tan \theta_1, \tag{3.7}$$

with θ_1 the opening angle of the beam given by Eq. (8.14).
This yields, for the actual focus position AFP as a function of the relative radius $0 < r_{\mathrm{rel}} < 1$ of the beam at the interface:

$$\mathrm{AFP}(r_{\mathrm{rel}}) = \mathrm{NFP} \frac{r_{\mathrm{rel}} \tan(\arcsin(\frac{\mathrm{NA}}{n_1}))}{\tan(\arcsin(\frac{n_1}{n_2} \sin(\arctan(r_{\mathrm{rel}} \tan(\arcsin(\frac{\mathrm{NA}}{n_1}))))))}. \tag{3.8}$$

Because of this dependence of the focal depth on the radial distance of the light rays, the effects of the refractive index interface on the PSF are *spherical* aberrations.
Note that for the outer rays, at $r = R$, Eq. (3.8) collapses to:

$$\mathrm{AFP}(1) = \mathrm{NFP}\frac{\tan\left(\arcsin\left(\frac{\mathrm{NA}}{n_1}\right)\right)}{\tan\left(\arcsin\left(\frac{\mathrm{NA}}{n_2}\right)\right)}. \tag{3.9}$$

With Eq. (3.8) we see a linear dependence of the AFP on the NFP, and we can define an axial scaling factor (ASF) as:

$$\mathrm{ASF}(r_{\mathrm{rel}}) = \frac{\mathrm{AFP}(r_{\mathrm{rel}})}{\mathrm{NFP}} \tag{3.10}$$

$$= \frac{r_{\mathrm{rel}}\tan\left(\arcsin\left(\frac{\mathrm{NA}}{n_1}\right)\right)}{\tan(\arcsin(\frac{n_1}{n_2}\sin(\arctan(r_{\mathrm{rel}}\tan(\arcsin(\frac{\mathrm{NA}}{n_1}))))))}, \tag{3.11}$$

with NA the numerical aperture of the objective, n_1 the index of refraction of the immersion fluid, and n_2 the index of the specimen.

In Figure 3.2, the calculated ASF is plotted as a function of the radial distance r, for 1.3 NA and 1.4 NA oil immersion objectives ($n_1 = 1.515$) used in water ($n_2 = 1.33$), in ethanol (1.36), and in a silica-matching solution (1.45). The graph clarifies many aspects of the index-interface-induced aberrations. As can be seen, for small radial distance r, the ASF does not change much, but in water and in ethanol, the decrease in ASF for large r is dramatic. For the dispersion with $n = 1.45$, the decrease is considerably less. The curve is plotted for NFP = 50 μm; the NPF does not influence the shape of the curve — as the ASF is independent of NPF — but it does determine the maximum radius R of the light cone at the interface. Due to a larger opening angle θ_1, R is larger for the 1.4 NA objective ($R = 0.121$ mm for NFP = 50 μm) than for the 1.3 NA objective ($R = 0.084$ mm). However, when the NA of the objective is larger than the index n_2 of the specimen, part of the rays will undergo total internal reflection at the interface; their angle of incidence ϑ_1 exceeds the critical angle θ_c, given by $\theta_c = \arcsin(n_1/n_2)$. This lowers the effective NA of the objective.

To approximate the over-all ASF, Eq. (3.10) has to be integrated over the area of illumination. Furthermore, Viana *et al.* [24] showed that the transmittance of the objective is a function of the radial distance. In addition, the illumination of the exit pupil can depend on r, for example when using a Gaussian beam. Therefore, for a good approximation of the ASF, both the transmittance, and the illumination of the objective have to be taken into account.

With the ASF different for different r, the broadening of the PSF depends on the NFP: the deeper into the specimen, the wider the focus becomes in

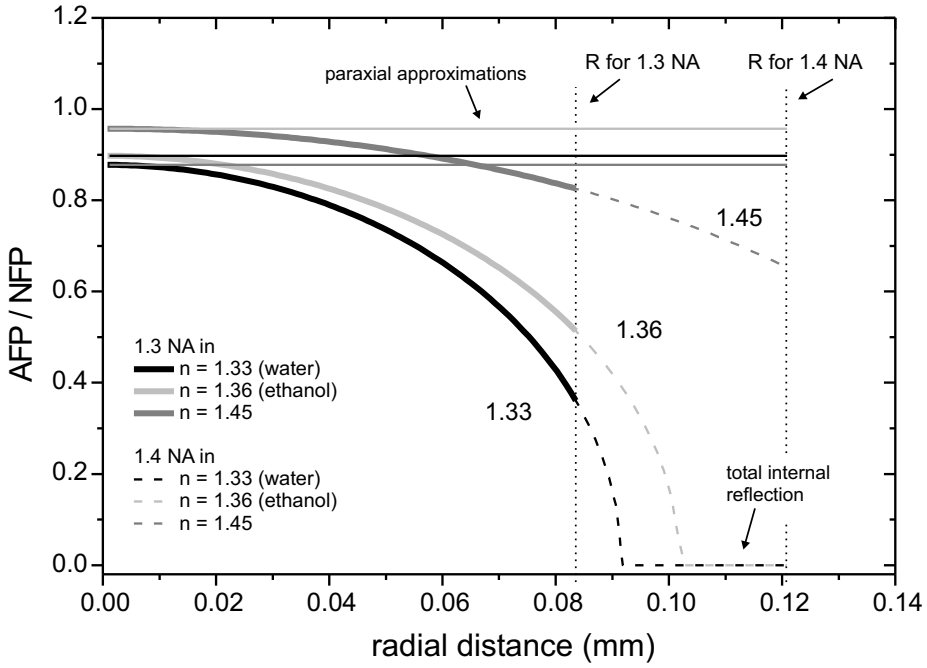

Fig. 3.2: The axial scaling factor ASF = AFP / NFP as a function of the radial distance r, calculated with GO, for 1.3 NA and 1.4 NA oil immersion ($n_1 = 1.515$) objectives in water ($n_2 = 1.33$), in ethanol ($n_2 = 1.36$), and in a silica-matching solution ($n_2 = 1.45$). The used NFP is 50 μm, which determines the maximum radial distance R for each objective. For the 1.4 NA objective, the NA exceeds n_2. Therefore, light rays for which $\vartheta_1 > \theta_c$ will undergo total internal reflection. For the three refractive-index mismatches, the paraxial approximation ASF = n_1/n_2) is also plotted.

axial and lateral direction. All these effects are more pronounced for a larger refractive-index mismatch.

Although GO gives too simple an approximation, the linear dependence of the AFP on the NFP was also found by Kuypers *et al.* [5], who used a theoretical model based on diffraction theory, and it has been confirmed experimentally in several studies [1, 4, 5]. The paraxial approximation ASF = (n_2/n_1) [25, 26] is also plotted in Figure 3.2 for the three specimen indices. This approximation, however, underestimates the effect of the spherical aberrations on the AFP. The deviations are limited for small NA, but rapidly increase for larger NA.

In this GO description, we only used a single refractive-index interface, not taking the presence of a cover glass into account. For an oil immersion objective, with n_1 equal to the index of refraction of the cover slide, this is correct. For a water immersion objective, however, the formulas have to be derived for the case of two index interfaces, which will yield a somewhat more complex relation

for the ASF.

Moreover, in this derivation, we only considered illumination of the objective by a beam parallel to the optical axis, giving a focal spot in the center of the field of view. For trapping or imaging away from this central spot, the results will differ.

3.2.1 Spherical aberrations and 3D confocal imaging

In confocal scanning laser fluorescence microscopy (CSLM) [27], the specimen is illuminated point-by-point with a laser beam focused by an objective lens. The fluorescence in the specimen is detected by the same objective, after which a spatial filter in the form of a pinhole eliminates all out-of-focus light. As a result, the confocal PSF is the product of the illumination PSF and detection PSF [28], resulting in an improved resolution and enabling optical sectioning of the sample.

The PSFs for illumination and for detection are not necessarily equal. The filling of the exit pupil, for example by a Gaussian scanning laser beam, is of influence on the illumination PSF [5]. In addition, a Gaussian-shaped dependence of the transmittance of high-NA objectives on the radial distance from the optical axis has been reported [24], influencing both the illumination and the detection PSF.

When focusing into a specimen with a refractive-index mismatch compared to the immersion fluid of the objective, both the illumination PSF and the detection PSF are affected by spherical aberrations. As a result, the lateral and the axial resolution, as well as the maximum intensity, decrease for increasing NFP. The effect on the axial resolution is stronger than on the lateral resolution [5, 6]. The reduction in maximum intensity for an oil immersion objective can be as much as 40% between 10 and 20 μm NFP in water [1]. In addition to the decrease in resolution, the axial distance is scaled. These effects of spherical aberrations affect the ability to reconstruct a 3D image of a scanned specimen.

As already mentioned in Section 3.1, the possibility to compensate for the spherical aberrations by changing the illumination profile at the exit pupil has been investigated theoretically [3], predicting good results in the recovery of resolution and signal.

Correction for the spherical aberrations afterwards has been done by deconvolution of the image [4]. The axial scaling cannot be compensated for. It has to be determined, and corrected for, with a calculated or an experimentally determined factor for the used experimental setup.

3.2.2 Spherical aberrations and optical trapping

The forces exerted by optical tweezers onto a particle, depend on the intensity gradient in the focal spot of the trapping laser [29]. A change in the PSF will

therefore affect the trapping forces on the particle.

As stated before, the PSF depends on the transmittance of the objective and on the filling of the exit pupil, in optical trapping usually by a truncated Gaussian beam. A mismatch in refractive index will distort the PSF, which translates directly to the trapping potential: broadening of the focal spot yields a smaller trap stiffness. Because the broadening is worse in the axial direction, also the effect on the axial stiffness is largest [16]. And, as the broadening of the focus depends on the NFP, also the trap stiffness depends on the NFP in the case of a refractive-index mismatch.

In quadrant photodiode (QPD) position detection [30], the momentum change of the light is measured, which is a direct measure for the trapping force [31]. A smaller stiffness (force per displacement) therefore corresponds to a smaller detector sensitivity (detector signal per displacement). Hence, the sensitivity β will depend on the NFP [32], even when a separate detection beam is used. As a consequence, β has to be calibrated at the depth in the specimen where the QPD measurements are performed.

In optical trapping, the potential well is assumed to be harmonic over a limited range around the trapping position. Due to the changes in the PSF in the case of a refractive-index mismatch, the potential of the trap possibly deviates from the harmonic approximation on a shorter range [11, 16]. This can introduce an additional error in the interpretation of force measurement data.

Most calculations of optical trapping forces assume a diffraction-limited spot and do not take spherical aberrations into account. Without correction for spherical aberrations, the calculated values will deviate more from the measured values for increasing refractive-index difference. Recently, Viana *et al.* [33] presented calculations corrected for spherical aberrations. Their results, without adjustable parameters, were in good agreement with their experimental work. The ASF, also present for optical trapping, is often not an issue, as the imaging is affected by axial scaling as well, although the scaling factors are not necessarily the same.

3.3 Experimental setup and methods

To combine optical trapping with 3D confocal microscopy, we used an inverted microscope (Leica, DM-IRB) in which the condenser was replaced by a second objective. This objective was used to focus an infrared laser beam (Spectra Physics, Millennia IR, 1064 nm, 10 W cw) into the specimen for trapping, while the opposing inverted objective was used for independent confocal imaging (both objectives: Leica, 100× 1.4 NA, oil immersion). This inverted objective was mounted on a piezo microscope objective scanner (Physik Instrumente, Pifoc P-721.20) for displacement along the beam axis. By moving the objective, different z-planes were imaged, which were combined to a 3D representation of

the specimen. Acousto-optic deflectors (AODs) were used to time-share the laser beam over two positions in the specimen at a time-scale fast enough compared to the Brownian motion of the particles in the trap [34]. By moving the upper objective along the optical axis with respect to the sample cell, the trapping plane was moved within the specimen. The setup is described in more detail in Section 2.2.

We used a mixture of single and dumbbell silica particles [35] dispersed in ethanol (n = 1.36). The 1.4-μm-diameter SiO_2 (n = 1.45) particles had a 0.4-μm-diameter SiO_2 core labeled with the fluorescent dye fluorescein isothiocyanate (FITC). The sample cell consisted of two cover slides (Menzel, No. 1) glued together with candle wax and filled with a diluted dispersion of the single-dumbbell mixture. The 488 nm laser line of the confocal microscope was used for illumination, and only the FITC-labeled cores of the particles were imaged.

The index of refraction of a material depends on the temperature and on the wavelength of the light used. Due to this latter feature, the indices of the immersion oil, of the dispersion medium and of the silica particles are different for the trapping laser light (1064 nm) than for the imaging laser light (488 nm).

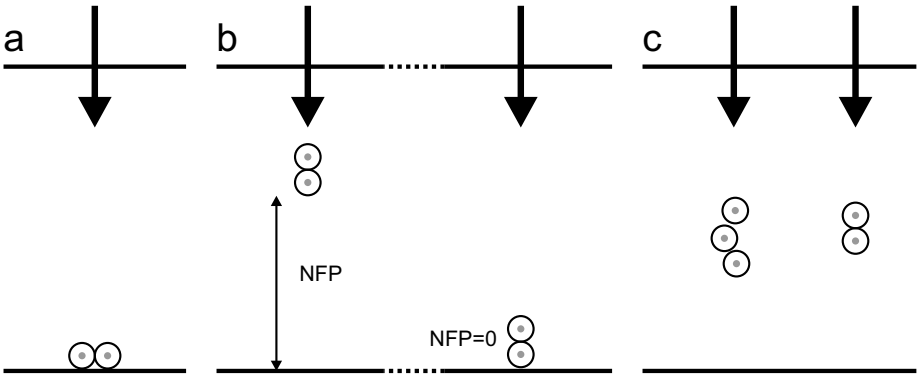

Fig. 3.3: Schematics of the measuring configurations. For confocal imaging, the inverted objective is used, while trapping was done with the upright objective (arrows). (a) A dumbbell trapped flat against the surface, to determine the core-to-core distance. (b) A dumbbell trapped at certain NFP in the sample. The position is changed to determine the ASF at several depths. (c) Two time-shared traps, with a dumbbell in one trap and three single particles in the other, at NFP = 20 μm, to determine the 3D configuration of three particles in optical tweezers.

Experimental method

To determine the axial scaling factor, the size or thickness of a certain object, or the distance between two objects, has to be known; this is the AFP. When imaging this distance, the displacement of the objective along the beam axis

is equal to the NFP. Kuypers and colleagues [5] used an elegant solution to know the true measured distance, which was by filling a single specimen with immersion oil and water next to each other. Imaging through the water gave the difference in NFP between the top and bottom surface. The true distance between the two surfaces, the AFP, was found by imaging through the immersion oil layer, for which no aberrations occurred.

With optical tweezers, a trapped particle can be moved over a distance along the optical axis, by moving the trapping objective. The displacement of this objective, however, is also scaled due to the difference in refractive index; the displacement of the objective is not equal to the displacement of the trapped particle, and the AFP difference is therefore not known.

To determine the axial scaling factor, we used a dumbbell particle with two fluorecently-labeled cores, positioned along the optical axis by trapping it in optical tweezers. The fixed distance between the two cores was measured by trapping the dumbbell flat against the bottom surface (Figure 3.3a). A series of xy confocal images was obtained, and the distance d between the two cores was taken to be the average distance over all frames in the image sequence.

With the core-to-core distance d known, the same dumbbell particle was held in one of two time-shared traps (Figure 3.3b). For several NFPs, z-stacks of images of the dumbbell were obtained. From these image stacks, the uncorrected 3D positions of the two cores were determined, and used to calculate the local axial scaling factor, making use of the tendency of the dumbbell to align along the beam axis in the trap. The other time-shared trap was filled with three single particles (Figure 3.3c). Using the obtained ASF, the 3D coordinates of those three particles in the trap were determined.

The dumbbell is not necessarily aligned exactly along the optical axis. Therefore, we take the displacement in xy of one core with respect to the other into account when determining the axial scaling factor ASF. For x and y we assumed the confocal microscope data to be accurate, so $x_m = x$ and $y_m = y$. The distance between the cores d is then defined as:

$$d = \sqrt{x^2 + y^2 + z^2}, \tag{3.12}$$

with x, y, and z the differences in position in the three orthogonal directions, and the axial distance z given by:

$$z = \mathrm{ASF} z_m, \tag{3.13}$$

with z_m the difference in NFP for the two dumbbell cores, which is equal to the axial displacement of the inverted objective.
For the axial scaling factor ASF, we can now write:

$$\mathrm{ASF} = \sqrt{\frac{d^2 - x^2 - y^2}{z_m^2}}. \tag{3.14}$$

It should be noted, that the difference in index of refraction between the silica particles ($n = 1.45$) and the dispersion medium ($n = 1.36$) introduces an extra source of aberration. The effect of these aberrations is different depending on whether the beam has to pass only through the silica shell, or also through a lower situated particle. This effect was not taken into account throughout this Chapter, but was expected to be relatively limited.

Determining particle coordinates

To determine the 3D coordinates of the particles in the trap [22], a home-written IDL (Research Systems, Inc.) routine was used which filtered the images of the data stack, before in each frame the particle positions were determined, using a method similar to the one described in Ref. [36]. A Gaussian was fitted to the integrated intensity profile of each particle in the z direction. However, for particles positioned above each other, it was difficult to distinguish between the cores, due to the axially extended PSF. For the dumbbell particle, we therefore plotted the integrated intensity, and fitted a double Gaussian (the sum of two separate Gaussians) to this curve. From this, the z-positions of the cores were obtained. Then, we plotted the xy-coordinates, and manually divided the data set into a set of coordinates for each core. This yielded the uncorrected 3D coordinates of the dumbbell cores, which gave, using Eq. (3.14), the local ASF.

The same procedure was followed for the three particles, now fitting a triple Gaussian to the integrated intensity profile and using the ASF obtained from the dumbbell data to scale the z distances.

3.4 Results and discussion

We determined the distance between the two cores of a dumbbell particle by imaging the particle trapped against the bottom surface. Averaging the distances over the 40 frames in an xy-series, we found for the core-to-core distance $d = 1.487$, with $\sigma = 0.017$ μm. The 6% difference with the expected d for the particle of 1.4 μm, might be due to the polydispersity of the particles, to a discrepancy in the xy-calibration of the confocal voxel size (we did not check this), or to near-field effects when imaging close to the surface.

In Figure 3.4a, the integrated axial intensity profiles are plotted for the dumbbell particle at several NFPs — starting at 0 μm, and then going down from 40 to again 0 μm — together with the double Gaussians fitted to these profiles. A stronger fluorescence can be seen for the higher core. Comparing the two curves for NFP = 0 μm gives an indication of the bleaching of the FITC during the measurements. For clarity, one of the profiles (for NFP = 30 μm) is given in Figure 3.4b, where also the individual Gaussians of which the sum is fitted to the profile are plotted.

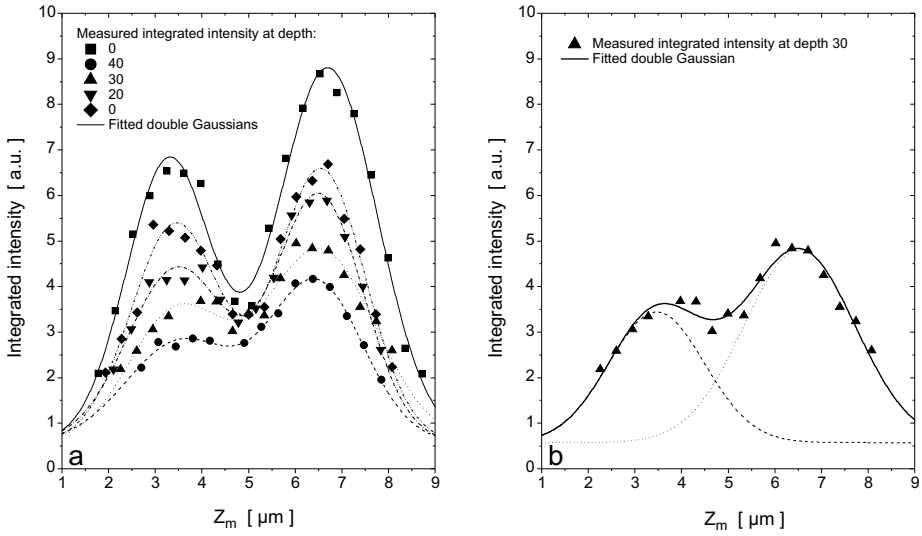

Fig. 3.4: Integrated intensity profiles in the axial direction for a silica dumbbell particle at different NFPs in ethanol. A double Gaussian was fitted to each curve, and the profiles were shifted in z such that the middle between the two Gaussian peaks was at 5.0 μm for each curve. (a) The profiles and the fitted double Gaussians for several NFPs. The difference in height between the first and the last profile — both measured at NFP = 0 — is due to bleaching. (b) The integrated intensity profile plotted for NFP = 30 μm. Also plotted are the fitted sum of two Gaussians and the two individual Gaussians.

The lowering of the maximum intensity for increasing NFP, due to spherical aberrations, is clearly visible in Fig. 3.4a. A corresponding widening of the peaks, however, is hardly apparent. In Figure 3.5a, we plotted the integrated axial intensity profiles, with the maximum of the double-Gaussian fit scaled to unity. The widths ω_1 (left peak) and ω_2 (right) of the fitted Gaussian peaks are given in Figure 3.5b, with the fitting errors indicated; the values can be found in Tabel 3.1. Due to the large relative error, a widening of the peaks cannot be claimed.

The difference in position for the peaks of the Gaussians gave the measured axial distance z_m. Tabel 3.2 lists the measured difference in xyz-coordinates between the two cores of the dumbbell at several NFPs, and the ASF calculated form them using Eq. 3.14. In Figure 3.6a the ASF is plotted for varying NFP. Also plotted are the average of the five values $\mathrm{ASF}_{average} = 0.75$ and the paraxial approximation $\mathrm{ASF}_{paraxial} = 1.36 \,/\, 1.515 = 0.898$. As shown in Section 3.2, the paraxial approximation overestimates the ASF. However, the spread of values around the mean – also given in Figure 3.6a in the measure ASF are large, making it precarious to draw strong conclusions. These large errors can be caused by motion of the dumbbell in the trap, or by the uncertainty in the

Tab. 3.1: Widths ω_1 and ω_2 of the two Gaussian peaks for which the sum is fitted to the intensity profiles, for several NFPs.

NFP	$\omega_1[\mu m]$	*error* $\omega_1[\mu m]$	$\omega_2[\mu m]$	*error* $\omega_2[\mu m]$
0	1.92	0.10	2.23	0.08
40	2.36	0.35	2.24	0.14
30	2.21	0.35	2.26	0.28
20	2.27	0.17	1.98	0.10
0	2.04	0.13	1.99	0.10

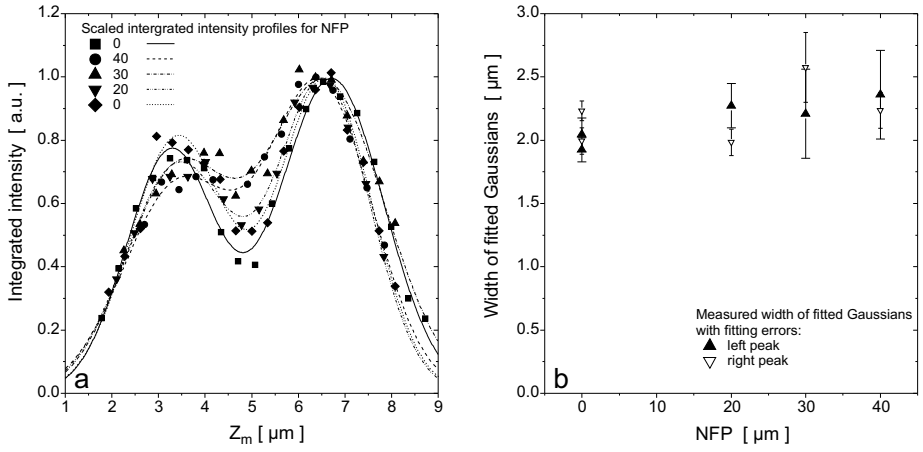

Fig. 3.5: (a) Integrated intensity curves with the maximum of the fit scaled to unity. (b) Fitted Gaussian peak widths and their fitting errors, for the left and the right peak.

Gaussian fits to the intensity profiles. We imaged close to the optical axis.

We used the data at NFP = 20 μm to obtain the coordinates of the three particles in the second trap. In Figure 3.6, the integrated intensity is plotted, together with a triple-Gaussian fit. From the plotted yz-positions of the three particles (Figure 3.7c), we see that the alignment of the three particles is tilted with respect to the optical axis of the imaging. For the dumbbell we see a tilt in the same direction, while the enhanced ray optics-based calculations of Gauthier and Ashman [21] for two single particles in a trapping beam predict alignment of both on the beam axis. This suggests that this tilt might be due to a misalignment of the trapping beam with the optical axis of the confocal imaging. Gauthier and Ashman [21] calculated the dynamic behavior of multiple spheres in an optical trapping beam, and for three particles they found that in the stable final configuration the center particle is pushed slightly out of alignment with the beam axis. The xy-projection of the positions (Figure 3.7a) shows that the

Tab. 3.2: Measured x, y, and z_m for several NFPs, with the ASF calculated from these values using Eq. (3.14) with $d = 1.487\mu m$.

NFP	$x[\mu m]$	$y[\mu m]$	$z_m[\mu m]$	*ASF*
0	-0.04	0.28	2.12	0.69
40	-0.08	0.24	1.82	0.81
30	-0.12	0.36	1.91	0.75
20	-0.12	0.32	1.90	0.76
0	-0.12	0.34	1.95	0.74

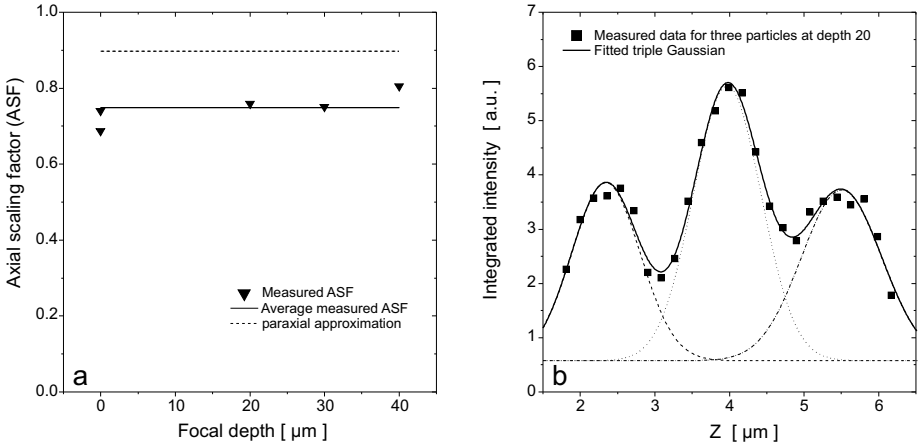

Fig. 3.6: (a) Axial scaling factor (ASF) measured at different focal depths in the sample using a dumbbell particle held in optical tweezers. Als indicated are the mean value $\mathrm{ASF}_{average} = 0.75$, and the paraxial approximation $\mathrm{ASF}_{paraxial} = 0.898$. Measured integrated intensity in the axial direction for three particles in a trap. A triple Gaussian is fitted to the data. The three individual Gaussians are indicated, as is the sum.

particles are not in one line, in accordance with those calculations. The distance between the particles is 1.732 μm for the lower and middle particle, and 1.677 μm for the middle and upper particle. This being 12% and 16% larger than the distance between the dumbbell cores of 1.487 μm, is an indication that the particles are charge-stabilized. We did not control the ionic strength in these experiments.

The fact that the particles were not fixed in space, but displayed Brownian motion in the optical trap, introduced errors in determining the core coordinates. Possibly stiffer trapping can reduce this error. The overlap of the Gaussian intensity profiles along the optical axis made it harder to determine the correct z position, especially for increasing NFP. A larger core-to-core distance is expected to improve the localization of the core positions, because there will be less signal

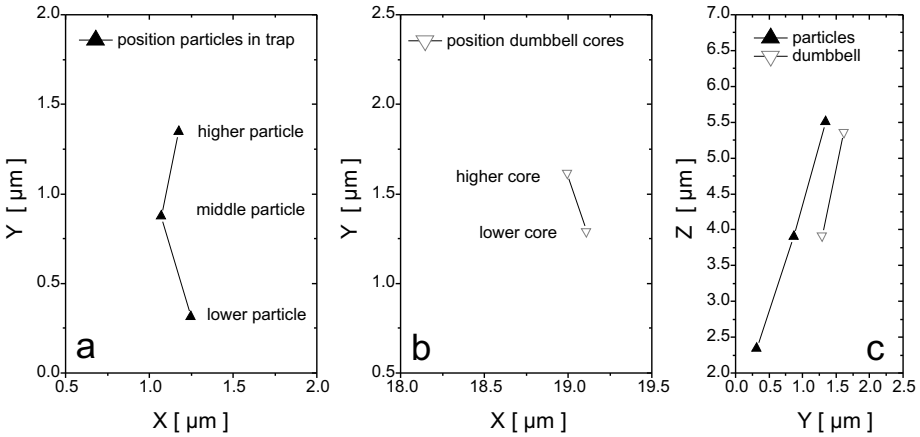

Fig. 3.7: Positions of the three particles and the dumbbell in two time-shared optical traps. (a) xy positions of the three particles, (b) xy positions of the dumbbell cores, and (c) the yz positions of all five cores.

overlap. In addition, with a larger distance between the cores, the relative error decreases.

3.5 Conclusions

Spherical aberrations due to a mismatch in index of refraction between the immersion fluid and a specimen, influence confocal imaging and optical trapping. The broadening of the point spread function causes a decrease in optical resolution and in trap stiffness, worsening with increasing focal depth. In addition, the actual depth of focus is scaled with respect to the nominal focus depth. When reconstructing 3D objects from confocal imaging data, this axial scaling factor (ASF) has to be taken into consideration to not over- or underestimate axial distances. These effects of a refractive index interface are more pronounced for increasing index difference. The ASF can be calculated [5] – including the illumination of the exit pupil and the radial dependence of the objective transmittance – or measured.

We used geometric optics (GO) to derive a simple representation of the effects on the PSF of a refractive-index mismatch. The ASF of a single ray depends on the radial distance of that ray to the optical axis. However, the ASF of each ray is independent of the NFP. Therefore, the overall ASF is also independent of the NFP. The difference in AFP for changing radial distance accounts for the broadening of the PSF. And although the ASF is independent of the NFP, the broadening increases for increasing NFP, because of the difference in ASF for the individual rays.

As a demonstration, we measured the ASF for an oil immersion objective

used in ethanol in our setup, by employing a silica dumbbell particle with two fluorescent cores. By trapping the dumbbell in optical tweezers, the particle, which aligned along the beam axis, could be imaged at different depths in the sample. We found an average ASF of 0.75. This is lower than the paraxial approximation of 0.90, which is in agreement with the literature. The large deviations in the measured ASF can be accounted for by inaccuracies due to Brownian motion of the particle in the trap. In addition, the small core-to-core distance, for which the PDFs overlap, introduced a large relative error in the measured distances. We used the experimentally obtained scaling factor to make a 3D reconstruction of the configuration of three silica particles held in a single optical trap. The particles aligned along the beam axis, although the center particle was pushed slightly outwards, in accordance with calculations [21]. The mismatch between the silica dumbbell and the ethanol introduced additional aberrations, which differed for imaging the upper core compared to imaging the lower core. However, it can be advantageous to measure the ASF *in situ*, and in a configuration similar to the configuration under examination – in our demonstration the three particles aligned along the beam axis.

It should be noted, that this single measurement is regarded as preliminary work, and no strong conclusions can be drawn, either about the ASF, or about the trapping configuration of three particles in a trap. For that, the accuracy of the particle position detection needs to be improved and the repeatability of the configurations investigated. In addition, the influence of the mismatch between the medium and the trapped particles should be examined.

3.6 Outlook

With the powerful combination of optical tweezers and confocal microscopy, we can image multiple trapped particles to make 3D reconstructions of their configuration. For better resolution, the particles are best suspended in a medium with a refractive index close to the index of the immersion fluid of the objective.

In the demonstrated system, there was a mismatch between the medium and the trapped particles. When imaging a higher trapped particle, the lower particles will affect the imaging. To better understand this influence, one could use core-shell particles with higher-index cores, and subsequently index-match the medium with the shells. The index difference is needed for optical trapping of the particle. Additional information can also be obtained by comparing the determined ASF with the ASF measured in a slab geometry [5]. Furthermore, by using glycerol objectives and glass that is index-matched with the immersion fluid for these lenses ($n \sim 1.48$), near-field effects of dumbbells at the wall should be minimal.

With the AODs, multiple traps can be moved independently with respect

to each other. This feature can be used to trap several configurations, and exchange their position. For example, a single particle can be trapped in one trap, while other traps are filled with two, three, or four particles. By measuring the 3D positions of the particles in the trap and then exchange their positions, the 3D configuration of multiple particles in a trap can be related to the position of a single trapped particle, without having to take any tilt of the focal plane or differences in the trapping potential between traps at different lateral positions, into account. This way the 3D configuration of multiple particles in a trap can be related to the position of the trapping beam axis, as indicated by the trapping position of a single particle.

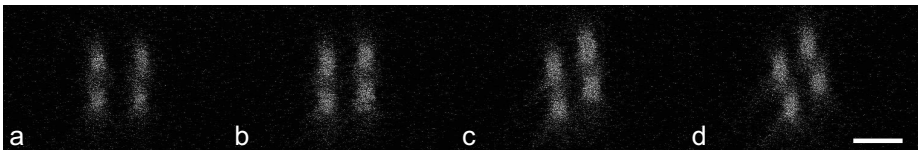

Fig. 3.8: xz-Confocal images of four 1.4-μm-diameter silica particles in two optical traps in the image plane. In each consecutive frame, the two traps are closer to each other. (a and b) The two particles in each trap align along the beam axis. (c and d) The traps are so close together that the particles push each other out of their original position. Only the 0.4-μm-diameter cores are imaged, and the images are scaled in z with ASF = 0.75. Scale bar is 2 μm.

Preliminary results of a slightly more complicated 3D configuration of particles are shown in the xz-confocal images in Figure 3.8. Here, four 1.4-μm-diameter silica particles were held in two time-shared trapping beams in the image plane. Each pair of particles aligned along the beam axis (Figure 3.8a and b). However, when the distance between the traps was decreased, the particles started to push each other out of this configuration (Figure 3.8c and d). The image was scaled in the z-direction with the ASF obtained in the experiment described in this Chapter (ASF = 0.75).

Acknowledgements

I would like to thank Toine van den Boogaard, who did most of the experimental work, Carlos van Kats for the dumbbell particles, Yu Ling Wu for help with the IDL image analysis, and Job Thijssen for useful discussions.

BIBLIOGRAPHY

[1] S. Hell, G. Reiner, C. Cremer, and E. H. K. Stelzer. Aberrations in confocal fluorescence microscopy induced by mismatches in refractive index. *J. of Microscopy*, 169:391–405, 1993.

[2] H. Jacobsen and S. W. Hell. Effect of the specimen refractive index on the imaging of a confocal fluorescence microscope employing high aperture oil immersion lenses. *Bioimaging*, 3:39–47, 1995.

[3] M. J. Booth, M. A. A. Neil, and T. Wilson. Aberration correction for confocal imaging in refractive-index-mismatched media. *J. of Microscopy*, 192(2):90–98, 1998.

[4] C. J. de Grauw, J. M. Vroom, H. T. M. van der Voort, and H. Gerritsen. Imaging properties in two-photon excitation microscopy and effects of refractive-index mismatch in thick specimens. *Appl. Opt.*, 38(28):5995–6003, 1999.

[5] L. C. Kuypers, W. F. Decraemer, J. J. J. Dirckx, and J.-P. Timmermans. A procedure to determine the correct thickness of an object with confocal microscopy in case of refractive index mismatch. *J. of Microscopy*, 218(1):68–78, 2005.

[6] A. Diaspro, F. Federici, and M. Robello. Influence of refractive-index mismatch in high-resolution three-dimensional confocal microscopy. *Appl. Opt.*, 41(4):685–690, 2002.

[7] A. van Blaaderen, A. Imhof, W. Hage, and A. Vrij. Three-dimensional imaging of submicrometer colloidal particles in concentrated suspensions using confocal scanning laser microscopy. *Langmuir*, 8(6):1514–1517, 1992.

[8] D. Bucher, M. Scholz, M. Stetter, K. Obermayer, and H.-J. Pflüger. Correction methods for three-dimensional reconstructions from confocal images: I. tissue shrinking and axial scaling. *J. of Neuroscience Methods*, 100:135–143, 2000.

[9] D. Malun, M. Giurfa, C. G. Galizia, N. Plath, R. Brandt, B. Gerber, and B. Eisermann. Hydroxyurea-induced partial mushroom body ablation does not affect acquisition and retention of olfactory differential conditioning in honeybees. *J. of Neurobiology*, 53(3):343–360, 2002.

[10] P. C. Ke and M. Gu. Characterization of trapping force in the presence of spherical aberration. *J. Mod. Opt.*, 45(10):2159–2168, 1998.

[11] A. C. Dogariu and R. Rajagopalan. Optical traps as force transducers: the effects of focusing the trapping beam through a dielectric interface. *Langmuir*, 16(6):2770–2778, 2000.

[12] E. Theofanidou, L. Wilson, W. J. Hossack, and J. Arlt. Spherical aberration correction for optical tweezers. *Opt. Comm.*, 236:145–150, 2004.

[13] K. C. Vermeulen, G. J. L. Wuite, G. J. M. Stienen, and C. F. Schmidt. Optical trap stiffness in the presence and absence of spherical aberrations. *Appl. Opt.*, 45(8):1812–1819, 2006.

[14] T. Ota, T. Sugiura, S. Kawata, M. J. Booth, M. A. A. Neil, R. Juskaitis, and T. Wilson. Enhancement of laser trapping force by spherical aberration correction

using a deformable mirror. *Jpn. J. Appl. Phys.*, 42(2):L701–L703, 2003.

[15] S. N. S. Reihani, M. A. Charsooghi, H. R. Khalesifard, and R. Golestanian. Efficient in-depth trapping with an oil-immersion objective lens. *Opt. Lett.*, 31(6):766–768, 2006.

[16] A. Rohrbach and E. H. K. Stelzer. Trapping forces, force constants, and potential depths for dielectric spheres in the presence of spherical aberrations. *Appl. Opt.*, 41(13):2494–2507, 2002.

[17] P. A. Maia Neto and H. M. Nussenzveig. Theory of optical tweezers. *Europhys. Lett.*, 50(5):702–708, 2000.

[18] A. Mazolli, P. A. Maia Neto, and H. M. Nussenzveig. Theory of trapping forces in optical tweezers. *Proc. R. Soc. Lond. A*, 459:3021–3041, 2003.

[19] M. P. MacDonald, L. Paterson, K. Volke-Sepulveda, J. Arlt, W. Sibbett, and K. Dholakia. Creation and manipulation of three-dimensional optically trapped structures. *Science*, 296:1101–1103, 2002.

[20] U. Gasser, E. R. Weeks, A. Schofield, P. N. Pusey, and D. A. Weitz. Real-space imaging of nucleation and growth in colloidal crystallization. *Science*, 292:258–262, 2001.

[21] R. C. Gauthier and M. Ashman. Simulated dynamic behavior of single and multiple spheres in the trap region of focused laser beams. *Appl. Opt.*, 37(27):6421–6431, 1998.

[22] A. van Blaaderen and P. Wiltzius. Real-space structure of colloidal hard-sphere glasses. *Science*, 270:1177–1179, 1995.

[23] J. Baumgartl and C. Bechinger. On the limits of digital video microscopy. *Europhys. Lett.*, 71(3):487–493, 2005.

[24] N. B. Viana, M. S. Rocha, O. N. Mesquita, A. Mazolli, and P. A. Maia Neto. Characterization of objective transmittance for optical tweezers. *Appl. Opt.*, 45(18):4263–4269, 2006.

[25] S. Nemoto. Waist shift of a Gaussian beam by plane dielectric interfaces. *Appl. Opt.*, 27(9):1833–1839, 1988.

[26] S. H. Wiersma and T. D. Visser. Defocusing of a converging electromagnetic wave by a plane dielectric interface. *J. Opt. Soc. Am. A*, 13(2):320–325, 1996.

[27] G. J. Brakenhoff, P. Blom, and P. J. Barends. Confocal scanning light microscopy with high aperture immersion lenses. *J. of Microscopy*, 117:219–232, 1979.

[28] S. W. Hell and E. H. K. Stelzer. *Lens aberrations in confocal fluorescence microscopy*, pages 347–353. Edited by J. B. Pawley (Plenum Press, New York and London), 1995.

[29] A. Ashkin. Observation of a single-beam gradient force optical trap for dielectric particles. *Opt. Lett.*, 11(5):288–290, 1986.

[30] M. W. Allersma, F. Gittes, M. J. deCastro, R. J. Stewart, and C. F. Schmidt. Two-dimensional tracking of ncd motility by back focal plane interferometry. *Biophys. J.*, 74:1074–1085, 1998.

[31] W. Grange, S. Husale, H.-J. Güntherodt, and M. Hegner. Optical tweezers system measuring the change in light momentum flux. *Rev. Sci. Instrum.*, 73(6):2308–2316, 2002.

[32] K. C. Vermeulen, J. van Mameren, G. J. M. Stienen, E. J. G. Peterman, G. J. L. Wuite, and C. F. Schmidt. Calibrating bead displacements in optical tweezers using acousto-optic deflectors. *Rev. Sci. Instrum.*, 77(1):013407, 2006.

[33] N. B. Viana, A. Mazolli, P. A. Maia Neto, H. M. Nussenzveig, M. S. Rocha, and O. N. Mesquita. Absolute calibration of optical tweezers. *Appl. Phys. Lett.*,

88(13):131110, 2006.

[34] K. Visscher, S. P. Gross, and S. M. Block. Construction of multiple-beam optical traps with nanometer-resolution position sensing. *IEEE J. Sel. Top. Quant. Electronics*, 2(4):1066–1076, 1996.

[35] P. M. Johnson, C. M. van Kats, and A. van Blaaderen. Synthesis of colloidal silica dumbbells. *Langmuir*, 21(24):11510–11517, 2005.

[36] J. C. Crocker and D. G. Grier. Methods of digital video microscopy for colloidal studies. *J. Colloid Interface Sci.*, 179:298–310, 1996.

4. IMPROVING THE ACCURACY OF LONG-RANGE PATTERNING OF COLLOIDAL PARTICLES

Optical tweezers are a versatile tool to pattern colloidal particles onto substrates. The patterning of colloidal particles is applicable in many fields, including colloidal epitaxy, colloidal lithography, and defect engineering in photonic crystals. Unlike techniques that rely on self-organization, e.g., controlled drying, optical trapping offers positional control over individual particles. In our optical tweezers setup, motorized actuators provide long-range displacement of the sample, while a high-accuracy piezo stage in a feedback loop using microscopy imaging ensures accurate positioning of every individual trapped particle in any desired arrangement. The method of one-by-one patterning enables the selection of particles from a mixture and discrimination against unwanted particles. By using two opposing objectives to create counter-propagating traps, high-refractive index particles that cannot be trapped in a single-beam gradient trap, can be patterned as well. In this Chapter, we demonstrate the patterning of substrates with mixtures of silica and high-index titania colloids. The particles could be selected from separate reservoirs and placed, with at least 60 nm rms *accuracy, at the intended positions on a glass wall.*

4.1 Introduction

The patterning of surfaces with colloidal particles finds its application in many different fields, including colloidal lithography [1, 2], colloidal epitaxy [3], and the creation of biological active structures [4]. Most ways of patterning are based on self-organization, such as controlled drying [5, 6], template-directed self-assembly [3], or spincoating [7]. None of these techniques, however, offer control over individual particles.

Recently, the use of optical tweezers for individual arrangement of particles on a substrate has been explored. While the first work was limited to collections of particles [8], or structures of only a few particles [9], Hoogenboom *et al.* [10] showed that one-by-one patterning of a large number of colloidal particles over an extended area is possible, with an accuracy of 73 nm (root-mean-square (*rms*) deviation). In Hoogenboom's work [10], silica particles were moved up from the bottom of the sample and positioned on the coated top surface, while either acousto-optic deflectors (AODs) steered the laser beam to the different positions of the intended structure, or a piezo stage moved the sample. Selection of particles was difficult, and, in addition, placement of the spheres was not checked by any feedback mechanism other than by eye, which made it hard to move far away from the pattern created and come back with high accuracy.

When patterning surfaces using optical tweezers, the accuracy of positioning is not only affected by the motion of the particle in the optical trap, but also by drift and hysteresis of the microscope stage, drift of the objectives, and by the pointing stability of the trapping laser.

In this Chapter, we combine long-range travel using motorized actuators with piezo positioning in a feedback loop with the camera image, for accurate repositioning of the sample. Drift of the specimen with respect to the objective is thus compensated for. We further demonstrate patterning with mixtures of colloids, including high-refractive index particles. The use of counter-propagating beams enables the stable three-dimensional trapping of these high-index particles, giving full positional control during patterning. The demonstrated technique of one-by-one patterning of 3D trapped particles combined with positional feedback control, will enable the generation of more complex 3D structures and, by using a two-step self-assembly method, the manipulation of defects in photonic crystals.

4.2 Experimental setup and methods

An infrared laser (Spectra Physics, Millennia IR, 1064 nm, 10 W cw) was split at a polarizing beam splitter cube to create counter-propagating optical tweezers (see Figure 2.1, page 16) using two opposing high-numerical aperture objectives. The inverted objective was used for imaging, while both the inverted and the upright objective were used for trapping. We used two 100× objectives (Leica,

1.4 NA, oil immersion), or a 63× objective (Leica, 1.4 NA, oil immersion) for imaging and a 100× objective for trapping.

For accurate positioning of particles at the top surface of a sample cell, the tweezers were kept at a fixed xy-position, while the sample was moved, using an xy-stage (Rolyn, 750-MS) fitted with motorized actuators (Newport, 850G-LS, closed-loop motorized actuators, 50 mm, accuracy 1 μm) for long-range travel, and an xyz-piezo stage (PI, P-563.3CD, 300×300×300 μm^3, accuracy 0.5 nm) for accurate positioning (see Figure 4.1). When patterning with an inverted single-beam gradient trap, the optical tweezers could also be moved towards the surface by moving the inverted objective, which was mounted on a piezo objective scanner (Physik Instrumente, Pifoc P-721.20). The experimental setup is described in more detail in Chapter 2, Section 2.2.

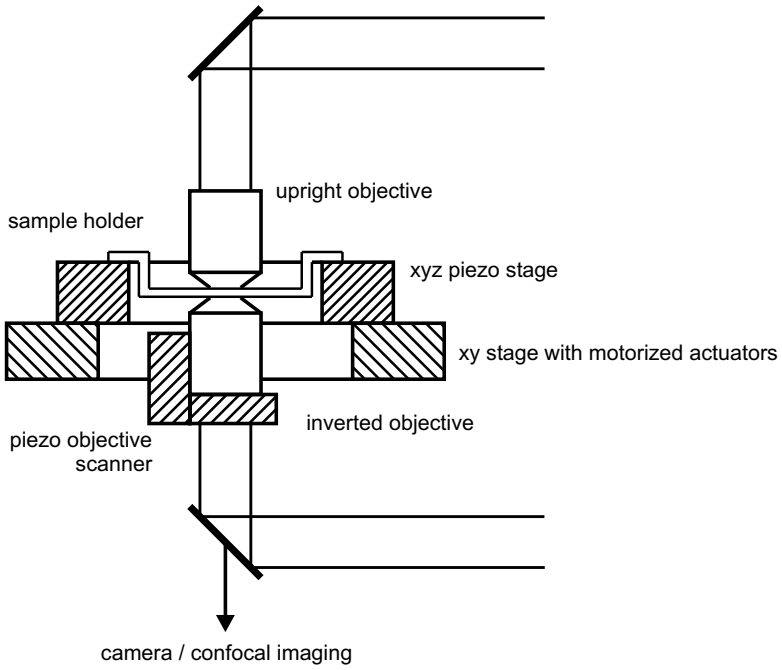

Fig. 4.1: Sideview of the setup, with two high-numerical aperture objectives for counter-propagating trapping, a microscope stage with motorized actuators for long-range displacements, and an xyz-piezo stage used in a feedback loop with position detection by image processing for accurate positioning of the sample. The inverted objective is mounted on a piezo objective scanner.

4.2.1 Feedback control of the piezo stage

To control the position of the sample during patterning, we used the piezo stage in a feedback loop with position detection by image processing. A custom-built program controlled the charge coupled device (CCD) camera (UNIQ, UP-600) and the piezo stage, as well as the piezo objective scanner and the motorized actuators.

We started by taking a reference image of one or preferably several particles on the top surface, at a position in the sample with few free particles. Then, using the motorized actuators, the tweezers were moved to a laterally displaced reservoir and a particle was selected (see Figure 4.2a for a schematic drawing). Returning to the starting position of the actuators, the reference particles were brought into the field of view again by moving the xyz-piezo stage down (Figure 4.2b). The axial trapping position of the particle was below the image focal plane, to be able to bring the top surface into focus without sticking the particle; this can be seen in Figure 4.3.

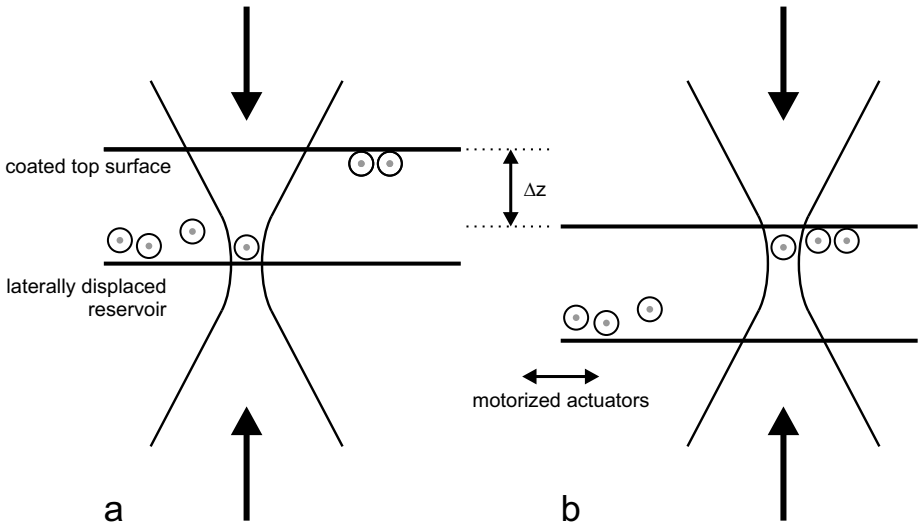

Fig. 4.2: Schematic sideview of patterning particles. (a) A particle is selected from a laterally displaced reservoir and trapped in counter-propagating optical tweezers. After translation of the sample using the motorized actuators, the pattern on the top surface is brought into the field of view (b), and the piezo xyz stage is used to position the trapped particle onto the surface.

By using a cross-correlation routine, the difference in position between the reference image and the current image was determined with sub-pixel accuracy (a few nanometers). The pixel size was typically 50–75 nm. The piezo stage was then moved to reposition the sample, and the cross-correlation was executed a second time to check the position. From here, the piezo stage was moved

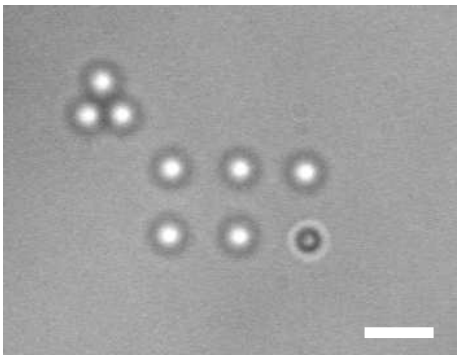

Fig. 4.3: Brightfield microscopy image of a pattern of 5 particles. A sixth particle, trapped below the focal plane, is ready to be patterned. An image of the three particles in the upper left corner was used as the reference image. Scale bar is 4 μm.

laterally to the next position of the pattern, and the particle was stuck to the surface by moving the stage in the z-direction.

By moving to the original starting position first for each particle, the same reference image could be used each time. However, to not be confined to the range of the piezo stage, a new reference image can be selected at any time. The software for image feedback and control of the stages was also used to control the camera and the stages on the setup described in Chapter 7.

4.2.2 Colloidal dispersions

For the patterning of mixtures of particles, we used a dispersion of 1.4-μm-diameter SiO_2 (refractive index $n = 1.45$) and 0.5-μm-diameter ZnS ($n = 2.0$) particles in ethanol ($n = 1.36$). The synthesis and characterization of the ZnS particles is described elsewhere [11]. The 1.4-μm-diameter silica particles had a 400-nm-diameter silica core, labeled with the fluorescent dye fluorescein isothiocyanate (FITC) [12–14]. Also, a mixture of 1.0-μm-diameter SiO_2 and 1.1-μm-diameter TiO_2 ($n = 2.4$) in ethanol [15], was used.

The sample cells consisted of two No. 1 cover slides sealed together with candle wax or UV glue and candle wax. Because all particles used sedimented to the bottom, they were patterned on the top surface, which was positively charged after coating it with 3-aminopropyltri-(m)ethoxysilane (APS). For this, the cover slides were placed in a mixture of 170 ml ethanol and 4.5 ml ammonia, after which 23.5 ml of APS was added. Following an hour of stirring, the cover slides were taken out, thoroughly rinsed several times with ethanol, and dried with N_2 gas.

To create a laterally displaced reservoir of particles, the sample cell, open on

two sides, was first filled with ethanol, after which the colloidal dispersion was flowed in. This way, a concentration gradient was set up, and patterning could be done at a position void of particles, or with a dilute concentration of choice.

4.2.3 Image analysis

To filter the images and determine the position of each particle with sub-pixel accuracy, a method, similar to the one described in Ref. [16], was used, in which local brightness maxima are identified, and a brightness-weighted centroid is fitted to the particle image.

The accuracy of patterning followed from the *rms* deviation of the particle positions away from their intended positions. To determine this value, we translated, rotated, and scaled the set of experimentally obtained particle coordinates, to best overlay the experimental and the intended pattern, assuming correct positioning of the intended pattern by the piezo stage. A rotation could be introduced by an angle between the field of view of the camera, the field of view of the confocal scan head, and the piezo stage axes. The scaling was used to compensate for a possible systematic deviation in the calibration of the camera pixels and of the confocal pixels.

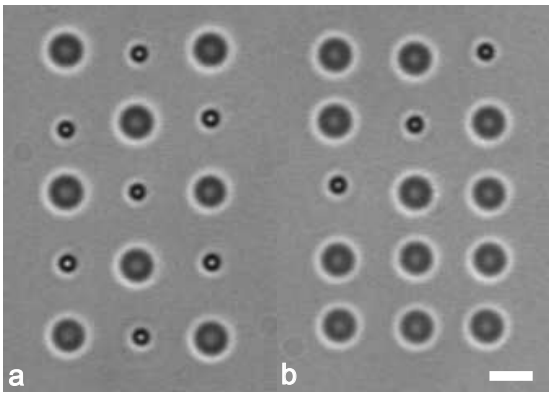

Fig. 4.4: Two patterns of a mixture of 1.4-μm-diameter silica particles and 0.5-μm-diameter high-refractive index ZnS. Patterning was done using counter-propagating tweezers; the ZnS particles could not be confined in a single-beam optical trap. Scale bar is 2 μm.

4.3 Results and discussion

Our first experiments were performed without image feedback control, only using the motorized actuators and the piezo stage. In Figure 4.4 we patterned with a mixture of ZnS and SiO_2, using a counter-propagating optical trap; the

ZnS particles could not be trapped in single-beam optical tweezers. By using a laterally displaced reservoir with a low concentration, we could, one-by-one, select particles from the mixture. The trap was kept stationary, while the sample was moved using the motorized actuators, and for each particle, we manually determined the position to pattern it.

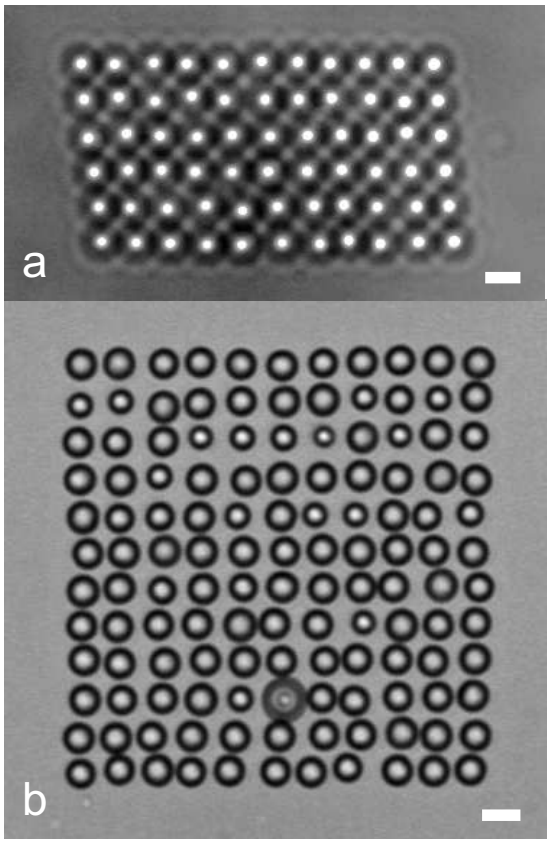

Fig. 4.5: (a) Row-by-row patterned 1.4-μm-diameter SiO_2 particles. The lateral shift due to drift is apparent. (b) Surface patterned, without any size selection, with polydisperse TiO_2 particles, using counter-propagating optical tweezers. Scale bars are 2 μm.

In Figure 4.5a, 1.4-μm-diameter silica particles were patterned row-by-row, starting from right to left, top to bottom. Drift of the sample with respect to the trapping position can be clearly seen. Figure 4.5b shows patterned TiO_2 particles from a polydisperse solution, when no selection based on size was done.

This same dispersion of titania particles, now mixed with silica, was used in the patterning shown in Figure 4.6. Here, 60 TiO_2 particles and 12 SiO_2 particles were stuck to an APS-coated surface. From the dilute dispersion,

particles were selected and trapped with a counter-propagating dual-beam trap, as the titania particles could not be trapped in single-beam optical tweezers. The sample was moved with the motorized actuators, while the tweezers were kept at a fixed position. To limit effects of hysteresis of the motorized actuators, we approached the sticking position from the same side each time. However, the deviations of the particles away from the intended positions, partly caused by drift of the sample, are clearly visible. Due to selection of the individual colloids, the size distribution of the patterned particles was improved as compared to the distribution in the dispersion.

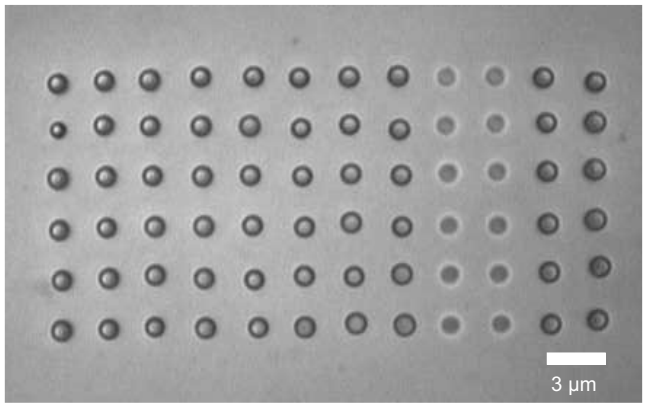

Fig. 4.6: Surface patterned with 60 TiO_2 particles and 12 SiO_2 particles. The TiO_2 particles cannot be trapped with a single-beam gradient trap. The diameters of the particles are 1.1 µm and 1.0 µm for the titania and silica, respectively. Scale bar is 3 µm.

The use of a laterally displaced reservoir of particles and long-range motorized actuators gave more flexibility to select particles from a mixture. This selection could be based on the material of the particle, or, for example, on the size of the particle, when using a polydisperse solution (compare Figures 4.5b and 4.6). One-by-one patterning, however, is time consuming, and for larger patterns, drift was often affecting the position accuracy. To compensate for this, feedback control is needed.

4.3.1 Patterning with feedback control

We compensated for drift of the sample, by performing feedback control based on the video microscopy image. To investigate the accuracy of the feedback control, we compared images taken after repositioning of the sample. Figures 4.7a–g show the sample at different time intervals during patterning. The sample returns to the same position, which can be clearly seen in the Figures 4.7h–m, where Figure 4.7a is subtracted from the Figures 4.7b–f. The patterned

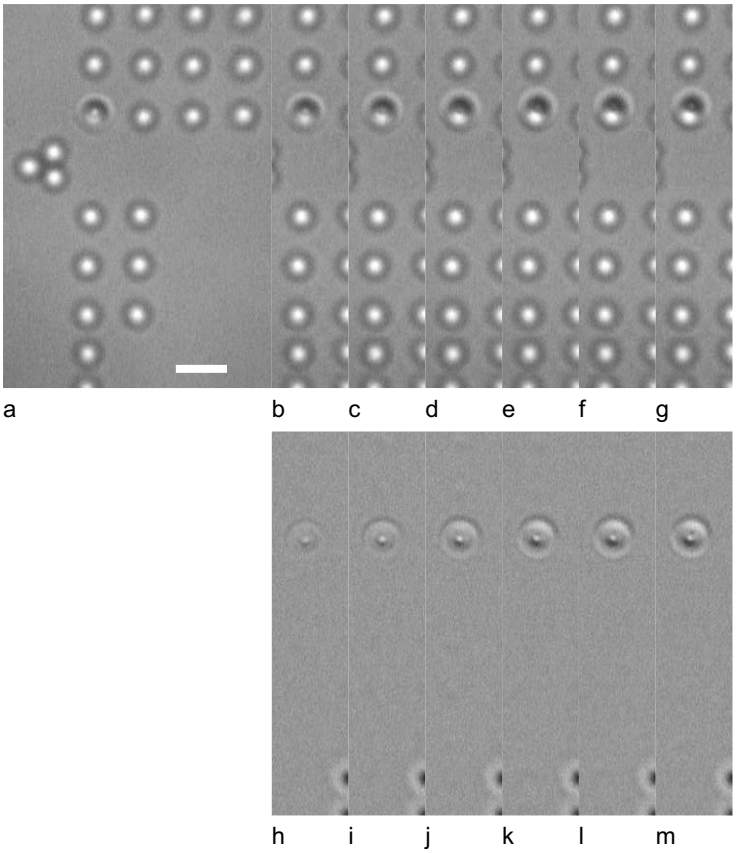

Fig. 4.7: Brightfield microscopy images of a trapped particle before it is positioned onto the surface. (a) A section of the pattern is visible; an image of the three colloids on the far left was used as the reference image. The trapped particle is slightly displaced with respect to the pattern position. (b–g) Images taken at +6, +16, +31, +57, +73, and +98 minutes. Repositioning of the sample was accurate to sub-pixel level, but the position of the trap with respect to the camera changed. (h–m) Images (b–g) with image (a) subtracted from them. The patterned particles are not visible in these images, indicating good repositioning of the sample. The drift of the trapped particle is clearly visible. Scale bar is 4 μm.

particles are not visible in these images, indicating good repositioning of the sample. (For clarity, a pixel value of 150 was added to the images.) Also clear from the images is that the trapped particle moved with respect to the camera. This could be due to pointing instability of the trapping laser, or to drift of one objective with respect to the other. This drift was not compensated for in the feedback control. The 63× inverted objective was used for imaging, while the

100× upright objective was used for trapping. For a typical trap stiffness of 50 pN/μm, the rms displacement of a particle in the trap is 10 nm.

To investigate the accuracy of patterning particles onto a surface, we analyzed the pattern of which a brightfield microscopy image is shown in Figure 4.8a, while Figure 4.8b depicts a fluorescence confocal image of the structure.

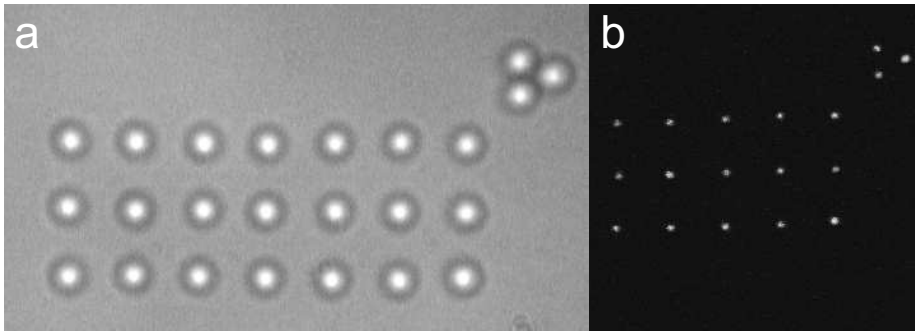

Fig. 4.8: A pattern of 1.4-μm diameter SiO_2 particles with a fluorescently (FITC) labeled 400-nm-diameter core. (a) Brigthfield microscopy image. (b) Fluorescence confocal image of a section of the pattern. Only the fluorescently labeled cores are visible. The distance between the particles is 4 μm.

First, we will look at the reproducibility of the position detection, which includes the image processing method, of the particles. For both the confocal images and the video microscopy images we determined the positions of the 15 particles from several images, overlaid their center-of-mass, and calculated for each of the 15 particles the rms deviation compared to the average position of that particle in the images. For the confocal data of five images (pixel size 97×97 nm^2), taken shortly after each other, we found an average rms deviation of 15 nm, while for five camera images (pixel size 75×75 nm^2), taken from one movie with the sample kept at a fixed position, this was 4 nm rms.

We also compared the two imaging techniques with each other, and found an rms value of 46 nm for the positions determined from the confocal image as compared to the positions from the camera image. The deviation between the two techniques is larger than the accuracy of either of the techniques — 15 nm and 4 nm for confocal and camera imaging, respectively. This indicates that even for a perfect pattern, deviations will be found.

In Figure 4.9 the intended positions are plotted together with the positions obtained from a confocal image and from a camera image. When comparing the confocal images with the intended positions we obtained an rms value of ∼132 nm, and an rms value of approximately 102 nm was found for the camera images with respect to the intended positions. These deviations, which were

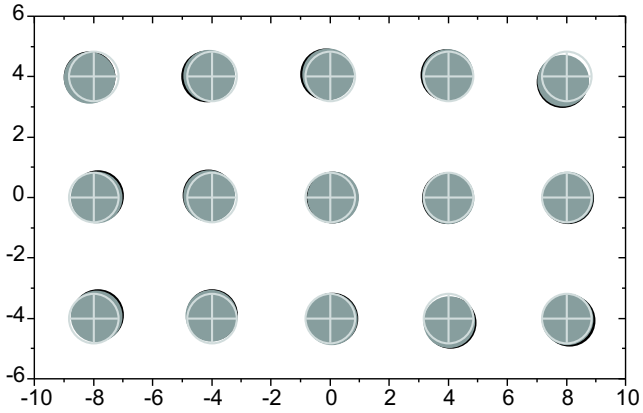

Fig. 4.9: Particle positions of the pattern shown in Figure 4.8b. Confocal data (black dots), camera data (gray dots), and intended positions (light gray crosses).

larger than the deviation we found between the two techniques, were mainly caused by the inaccuracy of the patterning. This could be due to drift of the trapping laser position, or to motion of the particle in the trap. The particle moves with respect to the focus of the laser beam due to Brownian motion. In addition, reflections and scattering from the interface and the particle play a role as well [17–19].

Optimizing the patterning method is expected to improve the accuracy. A better accuracy was already found for part of an other pattern. Figure 4.10 shows thirty 1.4-μm-diameter silica particles at 5 μm distance from each other. Although the accuracy of the whole pattern was >100 nm rms (data not shown), we found a value of 60 nm rms deviation of the positions away from the intended positions, for these thirty particles that were first patterned. We used a single-beam trap with 0.4 W laser power (corresponding to 45 mW in sample).

4.4 Conclusions and outlook

By combining counter-propagating trapping with separate reservoirs, mixtures of particles could be patterned, including high-refractive index particles that could not be trapped in single-beam gradient tweezers. One-by-one the particles could be selected, or discarded, based on their material, size, or suitability. By using feedback control based on image processing together with a high-accuracy piezo stage, we were able to compensate for drift of the sample with respect to the imaging objective. Drift of the trapping position with respect to the imaging system is at the moment not compensated for, which increased the deviation of the position of patterned particles away from their designated position. Improving the stability of the trapping position can, for example, be

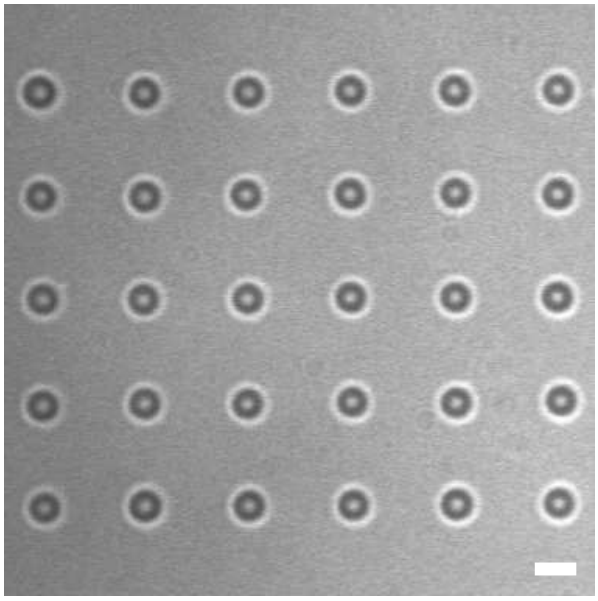

Fig. 4.10: Silica particles, patterned with an rms deviation of 60 nm. Scale bar is μm.

done by having the trapping laser beam pass through an optical fiber. A pointing instability will then be translated into a change in laser power. By analyzing the image of the trapped particle, the deviation can also be compensated for by moving the laser focus using the AODs. We demonstrated the patterning of particles with 60 nm *rms* deviation. The accuracy of patterning is also affected by the position of the particle in the optical trap, due to Brownian motion — determined by the trap stiffness — as well as due to reflections and scattering at the interfaces. Brownian motion can be reduced by trapping at a higher stiffness. More experiments are needed to optimize the circumstances and improve the accuracy. In addition, the influence of nearby particles on the positioning accuracy and effects of heating by the trapping laser beam can be investigated as well.

Acknowledgements

I would like to thank Yu Ling Wu for help with the IDL image analysis and Krassimir Velikov for the ZnS particles.

BIBLIOGRAPHY

[1] D. L. J. Vossen, D. Fific, J. Penninkhof, T. van Dillen, A. Polman, and A. van Blaaderen. Combined optical tweezers/ion beam technique to tune colloidal masks for nanolithography. *Nano Letters*, 5(6):1175–1179, 2005.

[2] D. K. Yi, M. J. Kim, L. Turner, K. S. Breuer, and D.-Y. Kim. Colloid lithography-induced polydimethylsiloxane microstructures and their application to cell patterning. *Biotech. Lett.*, 28(3):169–173, 2006.

[3] A. van Blaaderen, R. Ruel, and P. Wiltzius. Template-directed colloidal crystallization. *Nature*, 385:321–324, 1997.

[4] J. C. Garno, N. A. Amro, K. Wadu-Mesthrige, and G.-Y. Liu. Production of periodic arrays of protein nanostructures using particle lithography. *Langmuir*, 18(21):8186–8192, 2002.

[5] Y. A. Vlasov, X.-Z. Bo, J. C. Sturm, and D. J. Norris. On-chip natural assembly of silicon photonic bandgap crystals. *Nature*, 414:289–293, 2001.

[6] P. Jiang, J. F. Bertone, K. S. Hwang, and V. L. Colvin. Single-crystal colloidal multilayers of controlled thickness. *Chem. Mater.*, 11(8):2132–2140, 1999.

[7] P. Jiang, T. Prasad, M. J. McFarland, and V. L. Colvin. Two-dimensional nonclose-packed colloidal crystals formed by spincoating. *Appl. Phys. Lett.*, 89(1):011908, 2006.

[8] S. Ito, H. Yoshikawa, and H. Masuhara. Optical patterning and photochemical fixation of polymer nanoparticles on glass substrates. *Appl. Phys. Lett.*, 78(17):2566–2568, 2001.

[9] C. Mio and D. W. M. Marr. Tailored surfaces using optically manipulated colloidal particles. *Langmuir*, 15(25):8565–8568, 1999.

[10] J. P. Hoogenboom, D. L. J. Vossen, C. Faivre-Moskalenko, M. Dogterom, and A. van Blaaderen. Patterning surfaces with colloidal particles using optical tweezers. *Appl. Phys. Lett.*, 80(25):4828–4830, 2002.

[11] K. P. Velikov and A. van Blaaderen. Synthesis and characterization of monodisperse core-shell colloidal spheres of zinc sulfide and silica. *Langmuir*, 17(16):4779–4486, 2001.

[12] A. van Blaaderen and A. Vrij. Synthesis and characterization of colloidal dispersions of fluorescent, monodisperse silica spheres. *Langmuir*, 8(12):2921–2931, 1992.

[13] N. A. M. Verhaegh and A. van Blaaderen. Dispersions of rhodamine-labeled silica spheres: synthesis, characterization, and fluorescence confocal scanning laser microscopy. *Langmuir*, 10(5):1427–1438, 1994.

[14] H. Giesche. Synthesis of monodispersed silica powders II. Controlled growth reaction and continuous production process. *J. Eur. Ceram. Soc.*, 14(3):205–214, 1994.

[15] S. Eiden-Assmann, J. Widoniak, and G. Maret. Synthesis and characterization of porous and nonporous monodisperse colloidal tio_2 particles. *Chem. Mater.*,

16(1):6–11, 2004.

[16] J. C. Crocker and D. G. Grier. Methods of digital video microscopy for colloidal studies. *J. Colloid Interface Sci.*, 179:298–310, 1996.

[17] H. Fujiwara, H. Takasaki, J. Hotta, and K. Sasaki. Observation of the discrete transition of optically trapped particle position in the vicinity of an interface. *Appl. Phys. Lett.*, 84(1):13–15, 2004.

[18] A. Jonáš, P. Zemánek, and E.-L. Florin. Single-beam trapping in front of reflective surfaces. *Opt. Lett.*, 26(19):1466–1468, 2001.

[19] W. Inami and Y. Kawata. Analysis of the scattered light distribution of a tightly focused laser beam by a particle near a substrate. *J. Appl. Phys.*, 89(11):5876–5880, 2001.

5. HIGH-REFRACTIVE INDEX PARTICLES IN DYNAMIC ARRAYS OF COUNTER-PROPAGATING OPTICAL TWEEZERS

We demonstrate the simultaneous trapping of multiple high-refractive index ($n > 2$) titania particles in a dynamic array of counter-propagating dual-beam optical tweezers in which the destabilizing scattering forces are cancelled. A pair of acousto-optic deflectors allows for fast, computer controlled, manipulation of the individual trapping positions, while the method to create the patterns ensures the possibility of arbitrarily chosen configurations. The manipulation of high-index particles can be applied in the patterning of surfaces for colloidal epitaxy and colloidal lithography, and in exerting higher forces with low laser power in biophysical experiments.

5.1 Introduction

In 1986, Ashkin introduced the optical trapping of dielectric particles using a single-beam gradient trap [1]. In such a configuration, known as optical tweezers, a large gradient in light intensity is created by tightly focusing a laser beam using a high-numerical aperture (NA) objective. For particles with a refractive index n_p higher than that of the surrounding medium n_m, this gradient provides the necessary force to balance the destabilizing scattering force. In general, an increase in n_p or in the radius r of the particle yields an increase in both these forces. The dependence on r and on $m{=}n_p/n_m$, however, is stronger for the scattering force than for the gradient force. This limits the size and refractive index of particles that can be trapped in a single-beam gradient trap, and as a consequence, a limit is set to the trapping force of a single-beam gradient trap.

By using a second, counter-propagating, trapping beam, the scattering forces can be cancelled. Such dual-beam traps have been used before in several configurations [2–6]. In these cases, however, the focusing of the laser beam was mild, either due to the use of low-NA objectives or because the diameter of the beam was kept small, yielding a low effective NA of the trapping beam. Creating high trapping forces with a counter-propagating dual-beam trap was therefore not fully exploited.

We combine dual-beam trapping with the use of high-NA objectives — thereby canceling the scattering forces, while a large gradient provides a high trap stiffness — to trap high-refractive index particles that cannot be trapped with single-beam gradient tweezers.

In a variety of experiments it is desirable to create multiple traps, and, moreover, to be able to move these traps with respect to each other, for example to trap multiple particles [7–9]. In addition, non-spherical particles can be trapped with multiple dynamic traps for rotational control [10]. There are several methods to create such dynamic arrays of optical traps, including the use of holographic tweezers [11], and the generalized phase-contrast (GPC) method [12]. When using acousto optic deflectors (AODs), multiple traps can be created by mixing several sound frequencies before applying the combined signal to the AODs. An alternative method, however, demonstrated by Visscher *et al.* [7], is to time-share the laser beam over the array positions on a time-scale faster than the typical time-scale of the Brownian motion of the trapped particles.

In this Chapter, we combine counter-propagating trapping with the use of dynamic arrays of traps. Due to the configuration of the counter-propagating beam paths, the pattern imaged by the upright objective is mirrored with respect to the pattern imaged by the inverted objective. We present a method of scanning the pattern that enables us to create multiple dual-beam traps with arbitrary configuration using one pair of AODs.

5.2 Experimental methods

5.2.1 Experimental setup

To allow for counter-propagating dual-beam trapping in our setup (Figure 5.1a), the condenser of an inverted microscope (Leica, DM IRB) was replaced by a second high-NA objective (both Leica, 100×, 1.4 NA, oil) [13]. For a more detailed description of the setup, see section 2.2. An infra-red laser beam (Spectra Physics, Millennia, 1064 nm, 10 W cw) was split at a polarizing beam splitter cube, while the rotation of waveplate *WP* determined the ratio between the power sent to the inverted objective and the power sent to the upright objective. In both beam paths a pair of lenses ($L3_{i,u}$ and $L4_{i,u}$, all $f = 80$ mm) formed a telescope to provide manual displacement of the laser focus. The use of dichroic mirrors $DM_{i,u}$ allowed for illumination and imaging in the visible. Before splitting, the laser beam passed a pair of AODs (IntraAction, DTD-276HB6), positioned at a plane conjugate to the back focal planes of the objectives. The signal to the AODs was supplied by direct digital synthesizers (Novatech, DDS 8m), controlled by a *LabVIEW* (National Instruments) program. By fast repositioning of the laser focus, multiple time-shared traps were created. The position of the traps could be pre-programmed, or changed interactively. The beam was expanded in two steps: before the AODs by a 6× beam expander (*Exp*), and after the AODs ∼2× by the lenses *L1* and *L2* ($f = 120$ mm and $f = 250$ mm, respectively). To estimate the power inside the optical trap, we used the two-objective method [14]; the absorption of a beam passing the two objectives was measured, which gave – assuming equal absorption of both – the absorption of one objective.

5.2.2 Creating dynamic arrays of counter-propagating tweezers

A pattern scanned by the AODs is imaged inside the sample by both objectives. The upright objective, however, will give a mirror image of the pattern imaged by the inverted objective (see Figure 5.1b). To not be limited to symmetric patterns, we scanned both the desired pattern and its mirror image. Then, inside the sample, we placed the pattern from the inverted beam opposite the mirror image from the upright beam, creating an array of dual-beam traps.

By scaling the added mirror image, we could also compensate for differences in magnification between the inverted and the upright beam path, introduced by the telescopes, or by the use of objectives with different magnifications.

5.2.3 Sample cell

The sample cell, with a thickness of approximately 24 μm, consisted of two cover slips (Menzel, No. 1), sealed together with candle wax. It was filled with a dilute

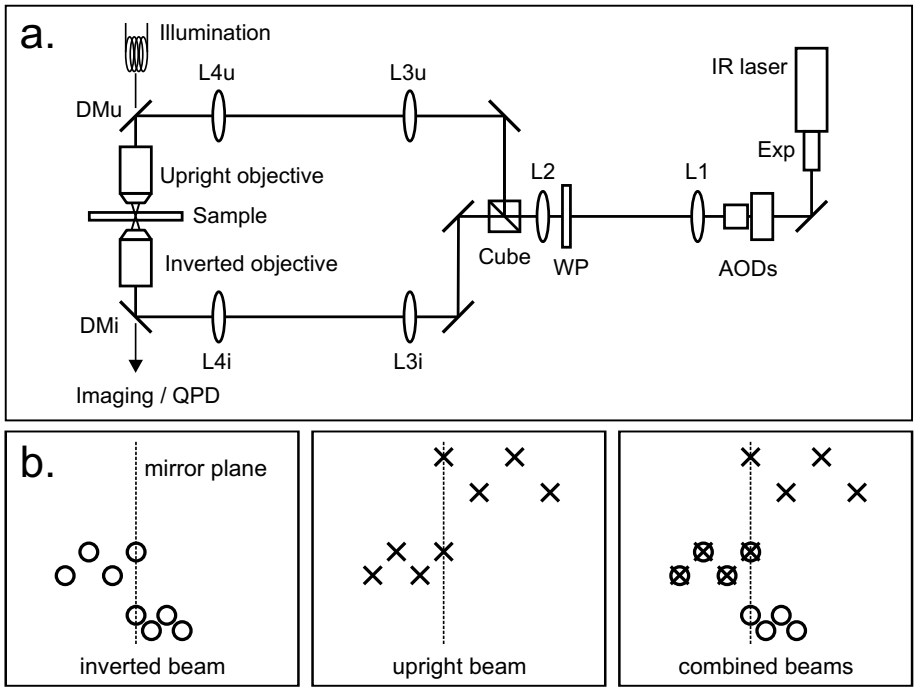

Fig. 5.1: Schematics of (a) the dual-beam optical tweezers and (b) the counter-propagating traps scanned with one pair of AODs. A mirrored and appropriately scaled pattern is added to the original traps, to create dual-beam traps of which the position can be arbitrarily chosen. The dashed lines indicate the mirror plane.

mixture of 1.4-μm-diameter SiO_2 ($n = 1.45$) particles and 1.1-μm-diameter TiO_2 ($n = 2.4$) particles in ethanol ($n = 1.36$).

5.3 Results and discussion

To create counter-propagating traps, we aligned the beam focused by the upright objective on top of the beam focused by the inverted objective.

Because the image focal plane was defined by the inverted objective, we started with trapping a silica particle with the beam coming from below. The z-position of the focus of the laser beam could be moved relative to the focus of the objective by moving $L3_i$ along the beam axis to change the beam divergence. Due to the limited difference in refractive index between the particle and the surrounding medium, the silica particle was trapped only slightly beyond the focal point of the trapping beam (24 nm, according to calculations for the case without spherical aberrations, see also Chapter 8). Therefore, by moving $L3_i$ and bringing the silica particle in focus, we positioned the focus of the trapping

laser approximately at the focus of the inverted objective. Now, the laser beam was parallel upon entering the inverted objective.

The position of the focus of the beam coming from above was determined not only by the position of the upright objective, but also by the divergence of the laser beam entering this objective. In the case of Köhler illumination, the condenser is in its correct z-position when the field diaphragm is in focus. Using the upright objective as condenser, we did not have true Köhler illumination, and using the image of the field diaphragm to determine the z-position was therefore not possible. We did use the image of the field diaphragm for alignment of the upright objective in the x- and y-direction. For the z-direction, however, we used the fact that the magnification of a pattern scanned by the AODs is different for the inverted than for the upright beam path, when the divergence of the two paths differ.

To find the position of $L3_u$ for which the upright beam is parallel at the objective, we started by time-sharing the beam over two positions, thus creating from each side two traps at a lateral distance of several micrometers from each other. We trapped two silica particles using the inverted objective to determine the positions of those two traps, and, by moving the upright objective in the z-direction (along the optical axis), brought the upright traps into the image focal plane of the inverted objective. Now, by moving $L3_u$ and compensating for this movement of the focus in the z-direction by moving the upright objective, we matched the magnification, while keeping the upright beam focus in the image plane of the inverted objective. When the magnifications matched – which was easily verified by alternatingly blocking the inverted and the upright beam and visually checking that the trapped particles did not change position – the focal planes of the two objectives were in close proximity of each other and the traps were aligned.

Dynamic arrays of dual-beam traps

The pattern in the stills from the movie in Figure 5.2 consisted of an array of eight traps. By combining them, four counter-propagating traps were created. The eight single-beam traps that were also formed, four from each side, were not used. The array of dual-beam traps, positioned at a distance of 12 μm from either wall, was filled with one silica and three titania particles. The total power inside the sample was 44 mW, corresponding to 5.5 mW for each individual dual-beam trap. The positions of the pattern were addressed at 4.5 kHz, and changed in 34 steps over a total period of 1.2 seconds, yielding an average speed of the particles of approximately 20 μm/s. At higher speeds, the silica particle was the first to escape from the trap, due to the drag force exerted on it by the medium.

Note that in brightfield microscopy, the 1.1-μm-diameter titania particles appear to be larger than the 1.4-μm-diameter silica particles, due to the higher

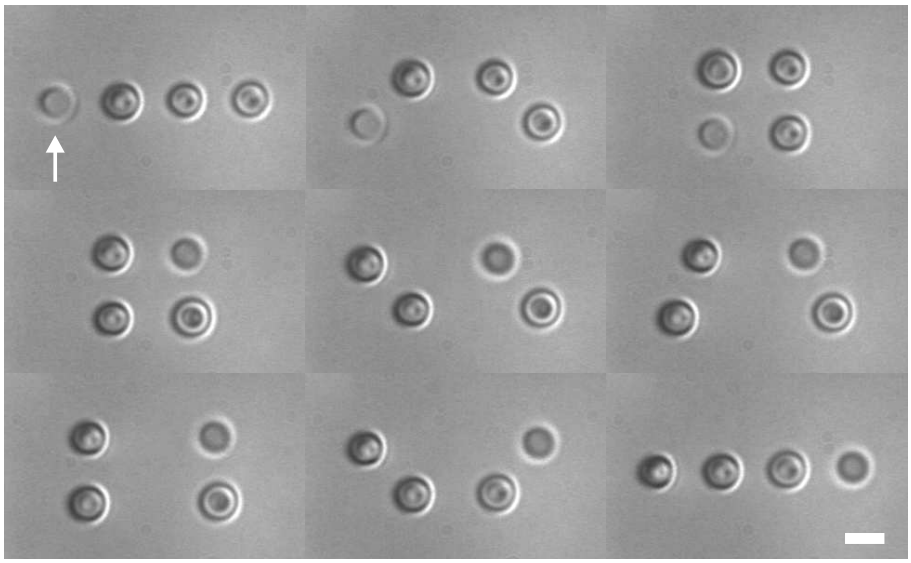

Fig. 5.2: Stills from a movie in brightfield microscopy of four dual-beam traps filled with one 1.4-μm-diameter SiO_2 (arrow) and three 1.1-μm-diameter TiO_2 particles. The pattern is changed in 34 steps in 1.2 seconds. Scale bar is 2 μm.

index of refraction [15]. Single-beam traps that are also formed can be positioned away from the trapping area, as far as the range of the AODs permits, to not disturb the counter-propagating traps. The 50 % loss of power into these traps is not a problem with the use of a high-power laser.

5.4 Conclusion and outlook

The trapping of high-refractive index particles in dynamic arrays of counter-propagating optical tweezers was demonstrated. The method of scanning both the pattern and its mirror image provides flexibility in manipulating multiple high-index particles, by supplying the possibility of arbitrarily chosen dynamic configurations of the dual-beam traps using a single pair of AODs. In addition, differences in magnification can be compensated for by scaling one of the patterns.

The trapping of high-index particles finds its application in, for example, patterning surfaces for colloidal epitaxy [16], colloidal lithography [17], and doping of photonic crystals, and in manipulating and rotating non-spherical high-refractive index particles like nanorods (Chapter 6). The possibility to exert high forces on multiple particles simultaneously will be further explored in biophysical force measurements (Chapter 8).

Acknowledgements

I thank J.S. Schütz-Widoniak for the TiO_2 particles, Jacob P. Hoogenboom for the SiO_2 particles, and Johan Herscheid for programming the interface to the synthesizers.

BIBLIOGRAPHY

[1] A. Ashkin. Observation of a single-beam gradient force optical trap for dielectric particles. *Opt. Lett.*, 11(5):288–290, 1986.

[2] A. Ashkin. Acceleration and trapping of particles by radiation pressure. *Phys. Rev. Lett.*, 24(4):156–159, 1970.

[3] S. B. Smith, Y. Cui, and C. Bustamante. Optical-trap force transducer that operates by direct measurement of light momentum. *Methods in Enzymology*, 361:134–162, 2003.

[4] P. J. Rodrigo, V. R. Daria, and J. Glückstad. Real-time three-dimensional optical micromanipulation of multiple particles and living cells. *Opt. Lett.*, 29(19):2270–2272, 2004.

[5] W. Wang, A. E. Chiou, G. J. Sonek, and M. W. Berns. Self-aligned dual-beam optical laser trap using photorefractive phase conjugation. *J. Opt. Soc. Am. B*, 14(4):697–704, 1997.

[6] W. Grange, S. Husale, H.-J. Güntherodt, and M. Hegner. Optical tweezers system measuring the change in light momentum flux. *Rev. Sci. Instrum.*, 73(6):2308–2316, 2002.

[7] K. Visscher, S. P. Gross, and S. M. Block. Construction of multiple-beam optical traps with nanometer-resolution position sensing. *IEEE J. Sel. Top. Quant. Electronics*, 2(4):1066–1076, 1996.

[8] W. Steffen, D. Smith, R. Simmons, and J. Sleep. Mapping the actin filament with myosin. *Proc. Natl. Acad. Sci. USA*, 98(26):14949–14954, 2001.

[9] A. van Blaaderen. Colloids under external control. *MRS Bulletin*, February:85–90, 2004.

[10] P. J. Rodrigo, L. Gammelgaard, P. Bøggild, I. R. Perch-Nielsen, and J. Glückstad. Actuation of microfabricated tools using multiple GPC-based counterpropagating-beam traps. *Opt. Express*, 13(18):6899–6904, 2005.

[11] E. R. Dufresne, G. C. Spalding, M. T. Dearing, S. A. Sheets, and D. G. Grier. Computer-generated holographic optical tweezer arrays. *Rev. Sci. Instrum.*, 72(3):1810–1816, 2001.

[12] R. L. Eriksen, P. C. Mogensen, and J. Glückstad. Multiple-beam optical tweezers generated by the generalized phase-contrast method. *Opt. Lett.*, 27(4):267–269, 2002.

[13] D. L. J. Vossen, A. van der Horst, M. Dogterom, and A. van Blaaderen. Optical tweezers and confocal microscopy for simultaneous three-dimensional manipulation and imaging in concentrated colloidal dispersions. *Rev. Sci. Instrum.*, 75(9):2960–2970, 2004.

[14] H. Misawa, M. Koshioka, K. Sasaki, N. Kitamura, and H. Masuhara. Three-dimensional optical trapping and laser ablation of a single polymer latex particle in water. *J. Appl. Phys.*, 70(7):3829–3836, 1991.

[15] J. Baumgartl and C. Bechinger. On the limits of digital video microscopy. *Euro-*

phys. Lett., 71(3):487–493, 2005.

[16] J. P. Hoogenboom, D. L. J. Vossen, C. Faivre-Moskalenko, M. Dogterom, and A. van Blaaderen. Patterning surfaces with colloidal particles using optical tweezers. *Appl. Phys. Lett.*, 80(25):4828–4830, 2002.

[17] D. L. J. Vossen, D. Fific, J. Penninkhof, T. van Dillen, A. Polman, and A. van Blaaderen. Combined optical tweezers/ion beam technique to tune colloidal masks for nanolithography. *Nano Letters*, 5(6):1175–1179, 2005.

6. THREE-DIMENSIONAL OPTICAL TRAPPING AND MANIPULATION OF HIGH-REFRACTIVE INDEX NANORODS IN LINE OPTICAL TWEEZERS

Semiconducting nanowires, such as ZnO and Si rods, are used in the fields of nanophotonics and nanoelectronics. Optical tweezers offer the promise of flexible positional control of such particles in liquids, but so far this has been limited to either manipulation close to the surface, or axial trapping of nanowires. We show the three-dimensional trapping of ZnO and silica-coated Si high-refractive index rods in counter-propagating line tweezers, and demonstrate translational and rotational in-plane manipulation, away from the surfaces. The particles investigated — 100-nm-thick ZnO rods with lengths varying from a few up to 15 μm and 10-μm-long silica coated Si rods with an approximate thickness of 200 nm — could not be trapped in single-beam line traps. Full translational and in-plane rotational control of semiconducting nanorods expand the possibilities to position individual rods in complex geometries significantly.

6.1 Introduction

Semiconducting nanowires, with optical properties like spontaneous emission, subwavelength waveguiding, and lasing, are useful as building blocks in nanoscale electronics [1] or photonic devices [2, 3]. To assemble these building blocks into functional circuits, specific positioning of nanorods is necessary. There are many techniques proposed for manipulation of rods, such as electric fields [4], micromanipulators [2], and fluidics [5].

Recently, optical manipulation has been explored as a method to position individual nanowires as well. This was first demonstrated by Yu *et al.* [6], with CuO rods being held against a surface in line optical tweezers. However, the use of a cylindrical lens to create the line tweezers limited the rotational control. Agarwal and colleagues [7] showed the trapping, by pressing them against a surface, of multiple CdS nanowires in dynamic holographic line tweezers, with the possibility of rotating, cutting, and fusing the wires. The first three-dimensional trapping away from the surface was reported by Pauzauskie *et al.* [8], who demonstrated trapping of nanowires, including GaN, ZnO, and Si, along the beam axis of the optical tweezers. Here, use was made of the fact that rods in an optical trapping beam experience forces that tend to align the particles along the optical axis. Rotational control, however, was in this case only obtained at the surface, after positioning one end onto the surface.

For spheres, an almost complete theoretical description of the trapping potential that has been verified by experiments, is possible [9, 10]. For strongly scattering rod-like particles, however, this is not the case. Based on our experience with the trapping of high-refractive index spheres (see also Chapter 8), it was expected that many high-index rods that are interesting for applications cannot be stably trapped in single-beam line tweezers.

In this Chapter, we demonstrate counter-propagating dual-beam line tweezers, in which ZnO and silica-coated Si nanorods are trapped in three dimensions, away from the surface. The use of two opposing high-numerical aperture objectives supplies the necessary intensity gradient, while the scanning of the line tweezers with Acousto-Optic Deflectors (AODs) enables full dynamic in-plane orientational control.

6.2 Experimental setup and details

6.2.1 Optical tweezers setup

An infra red laser beam (Spectra Physics, Millennia IR, 10 W cw, 1064 nm) was focused inside a microscope (Leica, DM IRB) to form optical tweezers. First, the beam passed a set of AODs, with which the xy-displacement of the laser traps inside the sample was controlled, and time-shared traps were created. After the AODs, the beam was split using a polarizing beam splitter cube. The

horizontally polarized beam entered the inverted objective, while the vertically polarized beam was focused by the upright objective (both objectives: Leica, 100×, 1.4 NA, oil immersion). These two opposing beams then formed counter-propagating traps, in which high-refractive index particles could be trapped. The setup is described in more detail in Section 2.2.

When creating counter-propagating tweezers, the two objectives remained at a fixed distance from each other. To move the traps, the sample was moved, using motorized actuators for long range displacement, in addition to an xyz-piezo stage (PI, 300×300×300 μm^3) for accurate positioning. A digital Charge Coupled Device (CCD) camera (Uniq Vision, UP-600) was used for imaging in brightfield microscopy.

Counter-propagating line tweezers

Using the AODs, line tweezers were created, which consisted of individual traps spaced 0.5 MHz apart, corresponding to 0.9 μm for the 100× objectives. Depending on the length of the nanowires, we used lines made up out of 5, 7, 9, 11, or 13 points, varying in length from approximately 3.5 to 11 μm. The two lines of a pattern were addressed one after the other, for each line starting at the center point, going, alternatingly left and right, outwards. Direct Digital Synthesizers (Novatech Instruments Inc., DDS8m) provided the signals to the AODs, and a *LabVIEW* program was used to create and switch between different arrays of traps. Addressing the pattern was done on a time scale of <1 ms; fast enough compared to the Brownian motion of a trapped rod in the tweezers. Per pattern, two lines of traps were created and superimposed, to create counter-propagating line tweezers. In this scheme, the two lines were independent, enabling full dynamic rotational control over the lines. By switching to pattern with different oriented lines, the trapped rods could be rotated. More information on creating dynamic dual-beam traps can be found in Chapter 5.

Because it was not possible to trap the rods in single-beam line tweezers, the alignment in xyz of the inverted and the upright beams was investigated by looking at the camera image of the trapping beams. After removing the IR filter, the upright beam, as well as the reflection of the inverted beam, were visible. Now, with the inverted objective focused onto the glass-medium interface, the divergence of the two beams was changed until satisfactory focused images appeared for both beams. Then, the line traps were placed on top of each other in the xy-direction.

6.2.2 Rod dispersions and sample cells

The ZnO rods were grown using the Vapor-Liquid-Solid mechanism, with gold nanoclusters as the catalyst particles and carbothermal reduction of ZnO powder as the vapor source [11, 12]. The index of refraction n of the zinc-oxide was 1.9

at the trapping wavelength, and the rods, with lengths varying from ∼0.5 to 15 μm, were dispersed in water ($n = 1.33$). The silicon rods ($n = 3.6$) were coated with a 50-nm-thick layer of silica ($n = 1.45$); their synthesis is described elsewhere [13]. They were dispersed in water, had a thickness of ∼200 nm, and lengths of 5 to 15 μm.

The samples consisted of two cover slips (Menzel, No. 1) sealed together with candle wax. Silica spheres were attached to the top surface by putting a dispersion of spheres onto the cover slip, and letting them dry before assembly of the sample cell.

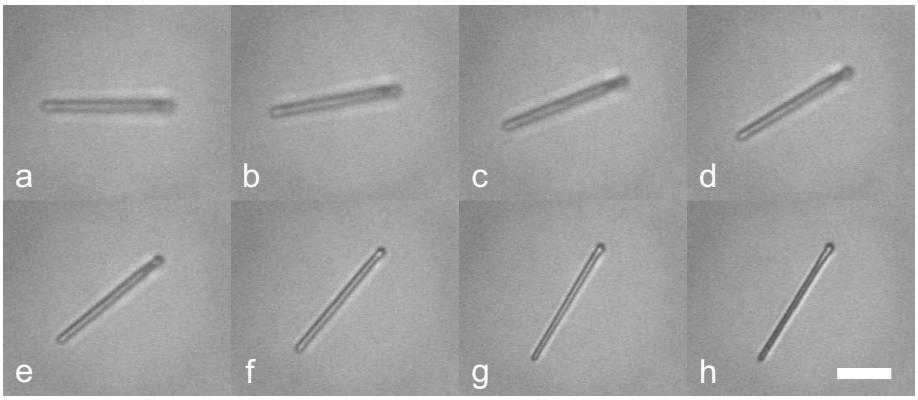

Fig. 6.1: Transmission microscopy image of a ZnO rod in water, trapped in counter-propagating line tweezers, at a distance of 30 μm from both top and bottom surface. The rod is rotated in steps of 10°, over (a) 0°, (b) 10°, (c) 20°, (d) 30°, (e) 40°, (f) 50°, and (g and h) 60°. For different orientations, the stable trapping position is located at a different depth z, due to the orthogonal polarizations of the inverted and upright trapping beams. Scale bar is 5 μm.

6.3 Results and discussion

Using single-beam line tweezers, the ZnO and silica-coated Si rods could be trapped against the surface. However, three-dimensional trapping in the plane perpendicular to the beam-axis, was not possible using single-beam line tweezers; the rods were expelled from the laser focus (not shown). Figure 6.1 shows a 13-μm-long ZnO nanowire, trapped in counter-propagating line tweezers. First, the rod was trapped horizontally with respect to the camera image, and was slightly out of focus. Then, the rod was rotated over 60°, in steps of ten degrees, and with each step, the rod moved in the z-direction and came more into focus. This is expected to be due to the influence of the polarization of the laser light. The polarization of the inverted trapping beam was left-right in the image plane, while the upright beam was perpendicular polarized, thus up-down in the image

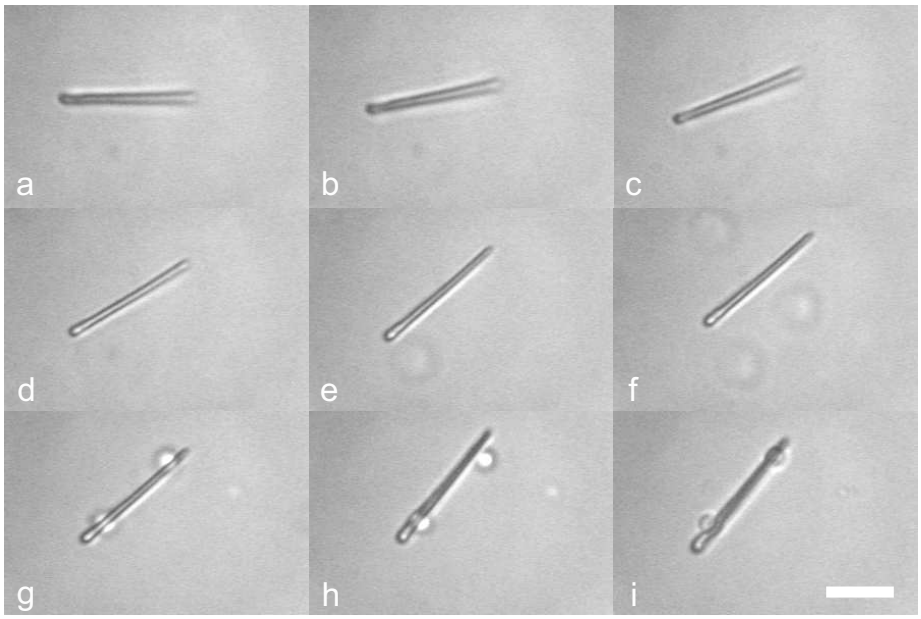

Fig. 6.2: Transmission microscopy image of a ZnO rod in water, trapped in counter-propagating line tweezers. The nanorod is rotated from (a) 0°, over (b) 10°, (c) 20°, (d) 30°, (e – g) 40°, and (h) 50°, to be (i) placed on top of two silica particles that were adhered to the top surface of a >30-μm-thick sample. Scale bar is 5 μm.

plane.

The ZnO rods could be stably trapped, translated in all three dimensions, and rotated in the plane perpendicular to the beam axis, which can be clearly seen in the Figures 6.2 and 6.3. In Figure 6.2, a rod was trapped and moved from the bottom to the top surface, over a distance of more than 30 μm. Silica spheres were attached to the top surface, and by translating the stage in xy, two spheres were selected. The rod was rotated over the desired angle, and positioned on top of these two spheres. Again, the dependence of the z-position of the rod on the rotation angle of the line tweezers is apparent.

Figure 6.3 also shows the trapping and lifting of a ZnO nanowire towards a silica sphere-coated top surface. Now, two touching spheres were selected, and the rod was trapped against the surface and then moved into the space in between the spheres and the surface. The rod was stuck there, but could still be rotated with the laser tweezers (Figures 6.3e–j). Figures 6.3k and l show images with an additional 1.6× optical zoom. It can be clearly seen that the rod is sticking through the space in between the surface and the two spheres.

In Figure 6.4, a silica-coated Si rod dispersed in water, is trapped in counter-propagating line tweezers, lifted off of the surface over 8 μm, and then rotated

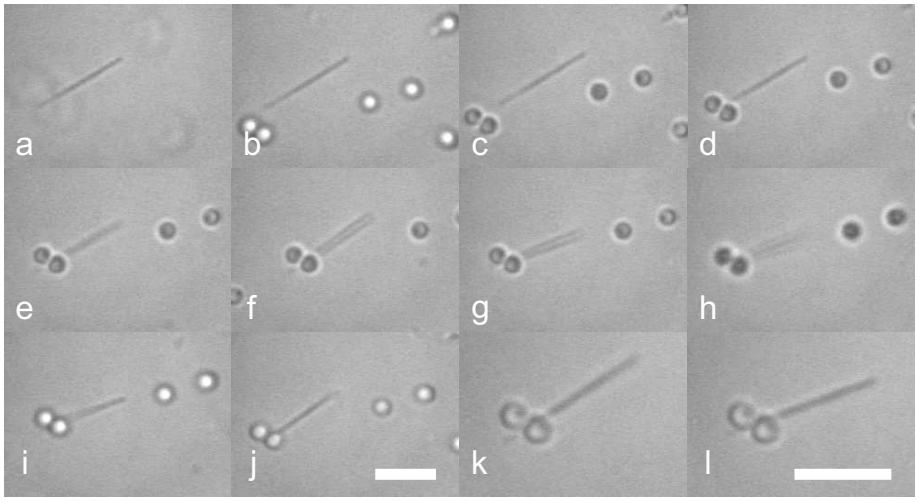

Fig. 6.3: Transmission microscopy image of a ZnO rod in water, trapped in counter-propagating line tweezers. The ZnO rod is (a – d) translated in the sample and (e) positioned underneath a pair of touching silica spheres that are adhered to the top surface. The rod could not be removed, although it could be rotated (f – j). (k and l) 1.6× optical zoom images of the nanorod, sticking through the space in between the surface and the spheres, and moved with tweezers. Scale bars are 5 μm.

over 10°. The Si rods could not be trapped in single-beam line tweezers, and were, in general, more difficult to trap in three dimensions than the ZnO rods. Stable axial trapping of the rods, like Pauzauskie and colleagues [8] did, was not possible, probably due to the large thickness of our rods (approximately 200 nm).

A separation of 0.9 μm between the traps that made up the line tweezers, was sufficient for in-plane trapping of the nanowires. Only very short rods (< 3 μm) tended to prefer an axial trapping direction, but, due to the limited stiffness in the z-direction for line-tweezers (see Section 6.5, page 89), it is doubtful that a closer spacing of traps would prevent this. Trapping with two 63× objectives (Leica, 63×, 1.32 and 1.4 NA, oil immersion) was not achieved, possibly because of a lower effective NA of the trapping beams due to underfilling of the back focal planes. The 63× objectives have a 1.5× larger opening than the 100× objectives; expanding the trapping beam to overfill the 63× objectives might make trapping of high-index rods with these objectives possible.

6.4 Conclusions and outlook

ZnO rods were trapped in counter-propagating line tweezers, and lifted >60 μm off of the bottom of the sample cell. We showed full rotational control in

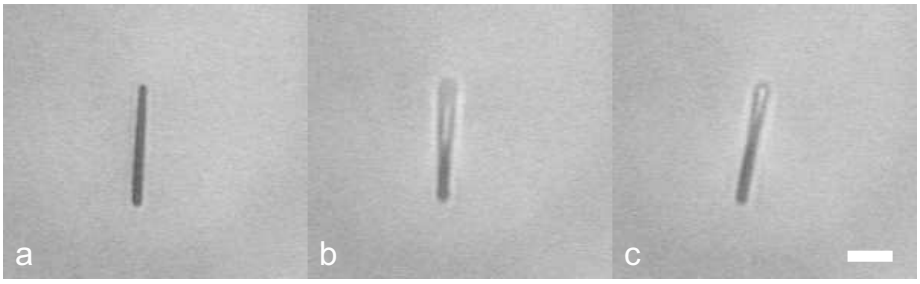

Fig. 6.4: A silica-coated Si rod in water, trapped in counter-propagating line tweezers (a) against the bottom surface, and (b) 8 μm above the bottom surface, where it is (c) rotated over 10°. Scale bar is 2 μm.

the plane perpendicular to the beam axes. As a demonstration, ZnO rods were brought to the top surface, where they were translated in the sample cell, and placed on top of two silica particles, or, alternatively, positioned in between the surface and two touching silica spheres. In addition, we showed the 3D trapping of silica-coated Si rods.

The trapping of these high-refractive index rods in the plane perpendicular to the beam axis away of the surface was not possible with single-beam line tweezers — in the axial direction no sufficient gradient force could be obtained to balance the destabilizing scattering force — and, to the best of our knowledge, has not been shown before. The possibility to manipulate, translate, and rotate individual nanowires, expands the range of possibilities in using these rods in nanoelectronics and nanophotonic applications.

Currently, we are working on coating the top surface of the sample cell to be able to attach the rods [14]. Free rods can reside at the bottom, and be selected, to then be transferred and adhered to the top surface. This way, configurations and structures of nanowires on the surface can be made permanent, and used in, for example, photoluminescence experiments.

When using line tweezers with a length shorter than the trapped rod, the rod tends to be tilted with respect to the focal plane. We plan to investigate the possibilities to combine line traps that are too short with intensity manipulation of the individual traps that make up the line, to control the pitch of trapped rods.

The use of AODs offers the flexibility to expand the arrays of traps to create two line traps, which can be moved independently from each other within the range of the AODs. This way, rods away from the surfaces can be positioned with respect to each other .

Acknowledgements

I would like to thank Andrew Campbell with whom I did the experimental work, Bert van Vugt for the ZnO rods, Carlos van Kats and Patrick Johnson for the Si rods, Peter van Oostrum for the calculations, and Johan Herscheid for the software development.

6.5 Appendix — Reduced axial trap stiffness in line tweezers

For line optical tweezers, created by closely-spaced optical traps, the axial stiffness is reduced in comparison to the stiffness of each individual trap. In this Section, we will look at the effects of nearby optical traps on the stiffness and trapping position of a particle in a single-beam trap. Calculations of the trap stiffness and the trapping depth are presented, and qualitative arguments are given to explain the effects of nearby traps on the trapping potential. In addition, we experimentally confirm the influence of traps in close proximity on the trapping depth of a particle. The difficulties in predicting the potential in a multiple-trap system from the potentials of the individual traps, are discussed.

A particle trapped in a multiple time-shared trap configuration, experiences the time-averaged potential of these traps when the time-sharing takes place on a time-scale faster than the typical time-scale of the Brownian motion of a particle in the traps [15, 16]. Because the individual traps do not exist simultaneously, no interference occurs, and the three-dimensional (3D) potential of the multiple-trap configuration is the sum of the 3D potentials of each individual trap in the system.

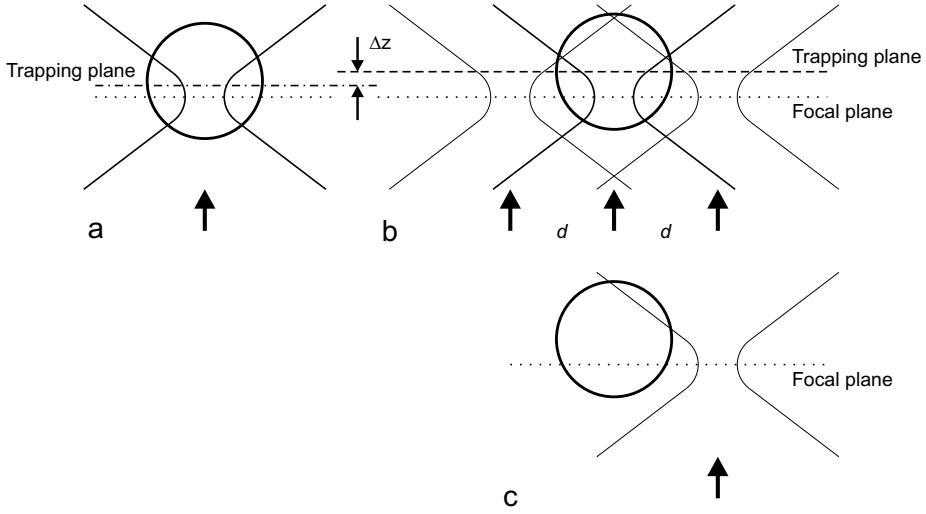

Fig. 6.5: Schematic view of (a) a particle trapped in an individual single-beam trap, (b) the same particle trapped in the middle one of three identical traps with trap separation d, and (c) the particle with respect to the right trap at the trapping position of the three-trap situation.

Calculations

To examine the influence of nearby traps on the trapping potential in a multiple-trap system, we considered the situation of a particle, held in a system of three

identical time-shared traps in close proximity to each other (Figure 6.5b).

We used the explicit partial-wave Lorenz-Mie representation given by Mazolli *et al.* [10] for our calculations of the axial trapping position and the axial trap stiffness κ_z. The three traps, with their beam axes in one plane and their foci at the same depth, are described by the parameters $\gamma = 1.18$ and $\theta_0 = 72.9°$ [10].

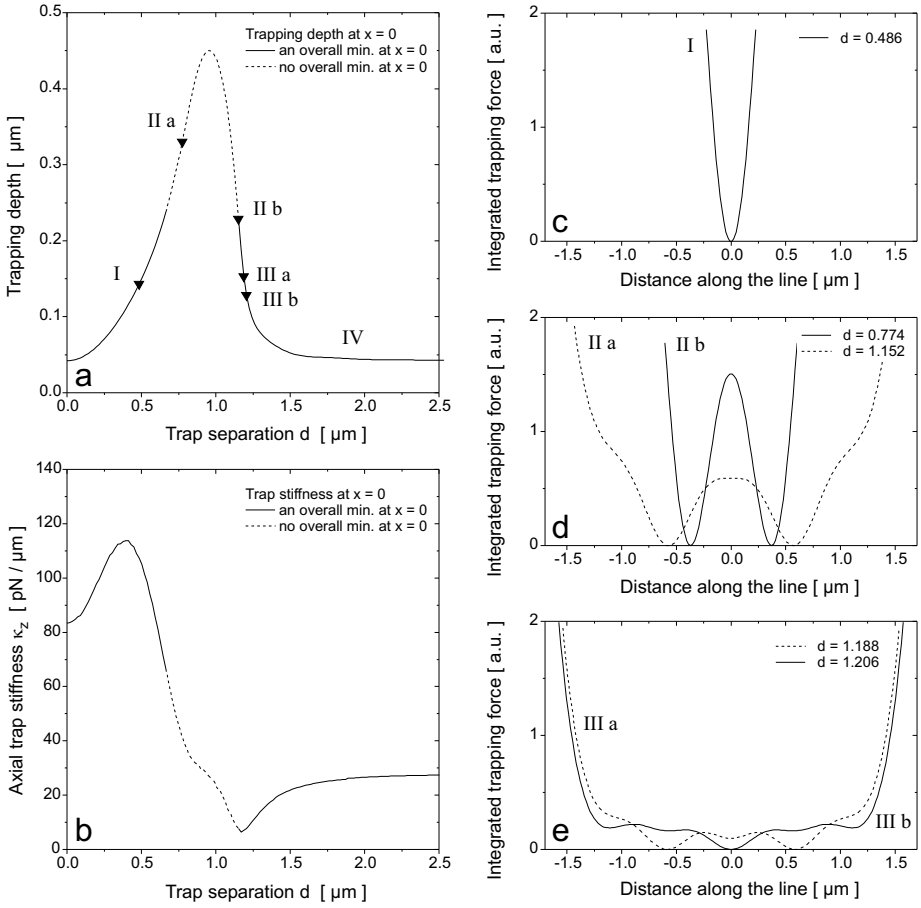

Fig. 6.6: Calculations for a 1.4-μm-diameter silica particle in a configuration of three optical traps. (a) For varying trap separation d, the trapping depth on the middle beam axis (x = 0) with respect to the focal plane. For certain separations (dashed line) the over-all minimum of the potential is not at x = 0. (b) Corresponding axial trap stiffness κ_z. (c–e) Integrated trapping force (*"potential"*) curves parallel to the line connecting the three traps, for several trap separations d. The Roman numbers correspond to positions indicated in (a). The curves illustrate the change from one stable trapping position (c), via two trapping positions (d), to one (e), before the beams are so far apart that they form three separate traps (indicated with IV in (a) but not shown).

Figure 6.6a shows the calculated axial trapping position of a 1.4-μm-diameter silica particle in ethanol, on the beam axis of the middle trap (x = 0) of a three-trap system, for varying distance d between the traps. In Figures 6.6c–f, the integrated trapping force (the *"potential"*) parallel to the line connecting the three traps, is plotted for several trap separations d. For every curve, the over-all minimum is set to zero. As can be seen, for small d, there is one stable trapping position at x = 0 (Fig. 6.6c), and the trapping depth increases for increasing d. For larger d, the stable trapping position splits up into two positions, located in between the three traps (Fig. 6.6d). This range, where the particle will not be stably trapped at x = 0, is indicated by the dashed part of the curve in Figure 6.6a. For even larger separation, the trapping depth decreases for increasing d, and the system will again have a stable trapping position at x = 0. First only at this center position (Fig. 6.6e), but for further increasing d there are three trapping positions (not shown). For certain separation, the trapping depth reaches its initial value; the traps are so far apart that a particle in the center trap does not experience any force from the two outer traps.

In Figure 6.6b, the corresponding axial trap stiffness κ_z is plotted. For $d = 0$, where the particle is trapped in three identical traps, the stiffness is three times the stiffness for large d, where the traps do not influence each other anymore. For increasing d, κ_z first increases, after which it drops blow the value for a single trap.

It should be noted that the presented calculations only show a very limited view of the complex 3D trapping potential, and the outcome as given here should be treated in a qualitative manner.

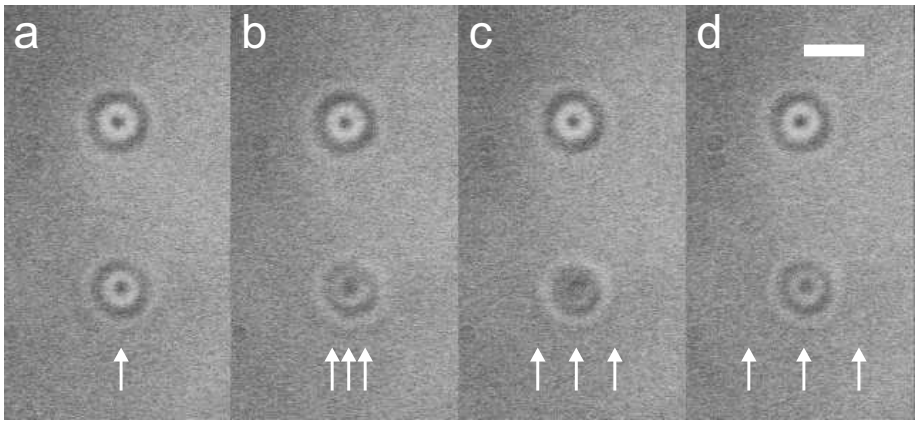

Fig. 6.7: Brightfield microscopy images of two 1.4-μm-diameter silica particles in four optical traps. (a) The top particle is trapped in one trap, while the bottom particle is held in three traps, which were moved away from each other over (b) 0.55 μm, (c) 1.27 μm, and (d) 1.82 μm. The axial trapping position depends on the distance between the traps. Scale bar is 2 μm.

Experimental confirmation

The larger trap position depth with respect to the focus position, as well as the decrease in trap stiffness for closely-spaced traps can be observed experimentally. Figure 6.7 shows two 1.4-μm-diameter silica particles in ethanol, in a system of four time-shared traps. The top particle is held in one trap, while the bottom particle is confined, in the same trapping plane, in three traps (Fig. 6.7a). Then, two of those three traps are moved away from the central third one, in steps of 0.18 μm. In Figure 6.7b, the distance between the traps is 0.55 μm, while for (c) and (d) the distances are 1.27 μm and 1.82 μm, respectively. As can be seen from the changes in the image of the bottom particle, the trapping position is displaced in the axial direction. In (c), the particle is trapped deeper than in (b), while in (d) the trapping is less deep than in (c), but still displaced with respect to (a). This qualitatively corresponds to the curve given in Figure 6.6a.

The decrease in stiffness to below the value for a single trap, was also clearly visible in the video images; for certain d the deviations of the particle in the single trap away from its stable trapping position, were smaller than the deviations of the particle in the three-trap configuration. An increase in stiffness for small d values was not observed. However, at the initial stiffness used, it would have been difficult to notice a decrease in motion of the particle.

Discussion

We will give a qualitative description of how the trapping depth and the trap stiffness of a particle are affected by traps in close proximity to the particle.

Because the three traps each have their focal point in the same z-plane, a particle will be confined at the same z-position and with the same stiffness, when trapped in one of the three traps individually (Figure 6.5a). However, with all three traps present, the two outer traps also contribute to the potential of the particle trapped in the middle. The effect of this added potential is two-fold. Due to the scattering force, the particle is trapped behind the focus of the single beam. Only part of the added outer two traps interacts with the particle, and as a consequence of the symmetry breaking about the focal plane, this added light moves the equilibrium trapping position of the particle even further from the focal plane: the particle is trapped at a larger depth in the sample (Figure 6.5b). In addition, due to the opposite gradients of the neighboring traps, the local gradient in the trapping region is decreased, which lowers the axial stiffness.

Due to the large opening angle of the trapping beam focused by a high-NA objective, a particle can be influenced by a trap at a relatively large lateral distance to the particle. This introduces an experimental difficulty in predicting the 3D potential landscape of a multiple-trap configuration from the measured potentials of the individual traps, as we will discuss in the next paragraph.

The 3D potential of an optical trap can be obtained by measuring the 3D

position of a particle in the trap in time. Due to Brownian motion, a particle will sample the potential landscape, revealing the shape of the trap [17]. In many trapping experiments, however, the position of a particle is not detected in three dimensions. Usually, both with video analysis, as well as with QPD position detection, the projection of the position onto the xy-plane is recorded, although information about the z-position is obtainable [17–19]. The 2D information of the potential well is clearly not sufficient to derive the 3D potential of the multiple-trap configuration. Moreover, even when the excursions of the particle in the z-direction can be neglected, the added 2D potentials only yield the 2D potential in the trapping plane of the individual traps, which is, as we have shown, not necessarily the trapping plane in a multiple-trap configuration. To be able to add the potentials of the individual traps, these potentials need to be known at the trapping position of the particle in the multiple-trap system. With only the right trap present (Figure 6.5c), the likelihood of a particle to be at the position of the trapping region of the three traps, is very small. Only for very low laser powers will the particle ever visit this region, with the possibility that then the particle is no longer trapped. An alternative method is to bring the particle with another trap to this position, let it go, and record its behavior. In general, the sampling time needed to obtain the potential of the trap in an area far from the focus of this trap, will be very long.

The results obtained for the simplified situation of a system of three closely-spaced traps, can be readily applied to a particle in optical line tweezers. A particle trapped in line tweezers experiences forces from many (time-shared) trapping beams. Therefore, a possible increase in axial trap stiffness for small d, as shown in the calculations, will disappear; for every beam at a favorable distance there are many others at less-favorable distances.

Concluding remarks

In conclusion, in single-beam line tweezers, a particle will be trapped at a larger depth and with a smaller stiffness, as compared to the trapping in an individual trap. The use of a different spacing between the individual points, or of a different-NA objective, cannot prevent this. In addition, the sampling of the individual traps over the full range necessary to obtain the line potential, is difficult, frustrating the prediction of the potential landscape of multiple closely-spaced traps.

When creating a line potential along which the potential differences are small enough compared to k_BT, a shallow z-potential might inhibit trapping in the z-direction. For counter-propagating line-tweezers, the trapping position will remain at the focal plane, because the scattering forces counter-act. Therefore, although the axial stiffness will be reduced in comparison to an individual counter-propagating trap, the decrease in stiffness will be less compared to single-beam line tweezers. This advantage of counter-propagating line tweezers

over single-beam line tweezers can be used in experiments such as, for example, measuring the pair potential of two particles in a 1D potential well. In the future, we will investigate the trapping in counter-propagating line tweezers, both experimentally and with calculations.

BIBLIOGRAPHY

[1] Y. Cui and C. M. Lieber. Functional nanoscale electronic devices assembled using silicon nanowire building blocks. *Science*, 291:851–853, 2001.

[2] D. J. Sirbuly, M. Law, H. Yan, and P. Yang. Semiconductor nanowires for subwavelength photonics integration. *J. Phys. Chem. B*, 109(32):15190–15213, 2005.

[3] D. J. Sirbuly, M. Law, P. Pauzauskie, H. Yan, A. V. Maslov, K. Knutsen, C.-Z. Ning, R. J. Saykally, and P. Yang. Optical routing and sensing with nanowire assemblies. *Proc. Natl. Acad. Sci. USA*, 102(22):7800–7805, 2005.

[4] P. A. Smith, C. D. Nordquist, T. N. Jackson, T. S. Mayer, B. R. Martin, J. Mbindyo, and T. Mallouk. Electric-field assisted assembly and alignment of metallic nanowires. *Appl. Phys. Lett.*, 77(9):1399–1401, 2000.

[5] B. Messer, J. H. Song, and P. Yang. Microchannel networks for nanowire patterning. *J. Am. Chem. Soc.*, 122(41):10232–10233, 2000.

[6] T. Yu, F.-C. Cheong, and C.-H. Sow. The manipulation and assembly of CuO nanorods with line optical tweezers. *Nanotechnology*, 15:1732–1736, 2004.

[7] R. Agarwal, K. Ladavac, Y. Roichman, G. Yu, C. M. Lieber, and D. G. Grier. Manipulation and assembly of nanowires with holographic optical traps. *Opt. Express*, 13(22):8906–8912, 2005.

[8] P. J. Pauzauskie, A. Radenovic, E. Trepagnier, H. Shroff, P. Yang, and J. Liphardt. Optical trapping and integration of semiconductor nanowire assemblies in water. *Nature Materials*, 5:97–101, 2006.

[9] A. Rohrbach. Stiffness of optical traps: Quantitative agreement between experiment and electromagnetic theory. *Phys. Rev. Lett.*, 95(16):168102, 2005.

[10] A. Mazolli, P. A. Maia Neto, and H. M. Nussenzveig. Theory of trapping forces in optical tweezers. *Proc. R. Soc. Lond. A*, 459:3021–3041, 2003.

[11] R. Prasanth, L. K. van Vugt, D. A. M. Vanmaekelbergh, and H. C. Gerritsen. Resonance enhancement of optical second harmonic generation in a ZnO nanowire. *Appl. Phys. Lett.*, 88(18):181501, 2006.

[12] M. H. Huang, Y. Wu, H. Feick, N. Tran, E. Weber, and P. Yang. Catalytic growth of zinc oxide nanowires by vapor transport. *Adv. Mater.*, 13(2):113–116, 2001.

[13] C. M. van Kats, P. M. Johnson, J. E. A. M. van den Meerakker, and A. van Blaaderen. Synthesis of monodisperse high-aspect-ratio colloidal silicon and silica rods. *Langmuir*, 20(25):11201–11207, 2004.

[14] J. P. Hoogenboom, D. L. J. Vossen, C. Faivre-Moskalenko, M. Dogterom, and A. van Blaaderen. Patterning surfaces with colloidal particles using optical tweezers. *Appl. Phys. Lett.*, 80(25):4828–4830, 2002.

[15] K. Visscher, S. P. Gross, and S. M. Block. Construction of multiple-beam optical traps with nanometer-resolution position sensing. *IEEE J. Sel. Top. Quant. Electronics*, 2(4):1066–1076, 1996.

[16] L. P. Faucheux, G. Stolovitzky, and A. Libchaber. Periodic forcing of a Brownian particle. *Phys. Rev. E*, 51(6):5239–5250, 1995.

[17] L. I. McCann, M. Dykman, and B. Golding. Thermally activated transitions in a bistable three-dimensional optical trap. *Nature*, 402:785–787, 1999.

[18] A. Pralle, M. Prummer, E.-L. Florin, E. H. K. Stelzer, and J.K.H. Hörber. Three-dimensional high-resolution particle tracking for optical tweezers by forward scattered light. *Microscopy Research and Technique*, 4:378–386, 1999.

[19] A. Rohrbach and E. H. K. Stelzer. Three-dimensional position detection of optically trapped dielectric particles. *J. Appl. Phys.*, 91(8):5474–5488, 2002.

7. OPTICAL TWEEZERS SETUP FOR FORCE MEASUREMENTS IN COUNTER-PROPAGATING TRAPS COMBINED WITH INDEPENDENT QUADRANT PHOTODIODE POSITION DETECTION

Optical tweezers are well suited to manipulate micron-sized particles and measure forces in the picoNewton range. Accurate position detection yields the force exerted on a particle in the trap, after determination of the trap stiffness. Here we present an optical tweezers setup, in which counter-propagating trapping with high-numerical aperture objectives is combined with quadrant photodiode position detection, to measure forces for high-refractive index particles. The stiffnesses are obtained from power spectral density curves of the position detection signal. Due to the use of a separate laser, position detection is independent from trapping, and can easily be combined with time-shared multiple dual-beam laser traps.

7.1 Introduction

Optical trapping is a versatile technique to manipulate micrometer-sized particles in a non-invasive manner, with the possibility of force measurements on the picoNewton scale [1–3]. This combination of features has been used in the fields of biology and soft condensed matter physics, with applications including the study of molecular motors [1], stretching of DNA [4], and microrheology on colloidal suspensions [5].

It is possible to directly measure the force exerted on a particle, by collecting all the light from the trapping laser after it interacted with the particle, and measure the change in momentum flux [6, 7]. Due to conservation of momentum, the change is a direct measure for the gain in momentum of the particle, thus for the force exerted on the particle. The demand to collect all the light inhibits overfilling of the objective with the trapping laser, as is mostly done in optical tweezers setups. Underfilling, however, decreases the effective numerical aperture (NA) of the laser beam and limits the trapping ability due to a decrease in gradient force. Grange and colleagues [6] and Smith *et al.* [7] circumvented this problem by using a second, opposing, low-NA trapping beam, to create counter-propagating tweezers, and directly measured forces by collecting the trapping light exiting from the sample.

In most schemes, though, force measurements are conducted in two steps. First, the stiffness of the trap – the force per displacement of the trapped particle at the trapping position – is determined, after which accurate position detection yields the force exerted on the trapped object. In recent years, several methods have been used to obtain the trap stiffness [3, 8]. The optical potential analysis [9], the Equipartition method, and the power spectral method [10], all employ the Brownian motion of the particle in extracting the stiffness. The latter two by assuming a harmonic potential. The motion of a particle with certain size in a harmonic potential, suspended in a medium with temperature T and viscosity η, is known, and from this the stiffness can be found. In the optical potential analysis, harmonicity of the potential is not necessary. It uses the fact that due to the thermal motion, the particle samples the potential well, and after long enough observation, the position distribution reveals the shape of the potential. With the drag force method [11, 12], the particle is moved with respect to the specimen at a certain speed, and from the displacement response of the particle, the trap stiffness can be obtained.

The accurate position detection, needed to determine the stiffness and consequently detect the displacement of the particle, is done in several ways. The two most commonly used are video image analysis [13], and quadrant photodiode (QPD) position detection using the trapping laser [14–16] or a separate detection laser [8]. Video analysis is accurate to subpixel-level (within a few nanometers), but does not offer the bandwidth necessary in most schemes to acquire the trap

stiffness. The use of a QPD for position detection is a very sensitive technique, and measuring steps as small as 0.1 nm has been reported [17]. Its operating speed enables the determination of power spectra up to 100 kHz [10, 18].

In this Chapter, we present an optical tweezers setup, in which counter-propagating trapping employing overfilled high-NA objectives, is combined with QPD position detection. Due to the use of a second laser, position detection is independent from trapping. This way, stiffness and force measurements can be done on high-refractive index particles, trapped in dual-beam time-shared traps.

7.2 Force measurements with quadrant photodiode position detection

The force on a particle in an optical trap can be determined by first fitting a Lorentzian to the power spectral density (PSD) curve of the QPD signal and obtain the trap stiffness κ. Once the stiffness is known, the position of the particle yields, for small displacements, the force.

7.2.1 Trap stiffness κ

In a single Gaussian-beam optical trap, a particle experiences a potential which can be approximated by a harmonic potential if the displacements of the particle from the center of the trap are not too large. The motion of a particle in such a harmonic potential is described by the Einstein-Ornstein-Uhlenbeck theory of Brownian motion [10, 19], for which the Langevin equation for one dimension reads:

$$m\ddot{x}(t) + \gamma_0\dot{x}(t) + \kappa_x x(t) = (2k_BT\gamma_0)^{1/2}\xi(t), \tag{7.1}$$

with m the mass of the particle, $x(t)$ its position in time, γ_0 the viscous drag coefficient, $-\kappa x(t)$ the harmonic force from the trap, and k_B Boltzmann's constant. $(2k_BT\gamma_0)^{1/2}\xi(t)$ represents the random Gaussian distribution of the Brownian forces at temperature T. With the experimental time resolution long in comparison with the typical time scale for loss of kinetic energy through friction, the inertial term can be dropped. Defining the roll-off frequency f_0:

$$f_0 = \frac{\kappa}{2\pi\gamma_0}, \tag{7.2}$$

we can rewrite Eq. (7.1), and find for the motion of the particle:

$$\dot{x}(t) + 2\pi f_0 x(t) = (2k_BT/\gamma_0)^{1/2}\xi(t). \tag{7.3}$$

Fourier transformation will give the power spectral density $S_x = \mathrm{X}^*(\mathrm{f})\ \mathrm{X}(\mathrm{f})$ — the amount of power per unit of frequency as a function of the frequency — for

the motion as a Lorentzian [14, 16]:

$$S_x(f) = \frac{k_B T}{\gamma_0 \pi^2 (f_0^2 + f^2)}, \tag{7.4}$$

with S_x in units of distance^2/frequency. The viscous drag coefficient γ_0 for an isolated sphere with radius r, relatively far away ($>> r$) from a wall, in a medium with viscosity η, is given by Stoke's law:

$$\gamma_0 = 6\pi\eta r, \tag{7.5}$$

so we find for the stiffness κ:

$$\kappa = 12\pi^2 \eta r f_0. \tag{7.6}$$

By fitting a Lorentzian to the PSD curve, the roll-off frequency f_0 is obtained. Equation (7.6) then gives the stiffness κ, and measuring the displacement Δx will yield the force on the particle in the harmonic potential with:

$$F_x = \kappa_x \Delta x. \tag{7.7}$$

For constant drag coefficient η, κ increases linearly with increasing laser power of the optical trap.

7.2.2 Quadrant photodiode measurements

The linear regime of the focused Gaussian beam — where the potential well can be approximated by a harmonic potential — is exploited in QPD position detection. In this regime, the force exerted on a particle scales linear with the deviation of the particle from the trap center. As a consequence, the signal onto the QPD — a measure for the change in momentum flux which is directly related to the force exerted on a particle [6, 7] — is also linearly related to the deviation, enabling position detection.

When using a separate laser for QPD detection, the power of the detection laser is set low enough, so that trapping of the particle by the detection beam can be neglected compared to the trapping by the trapping beam. The use of a separate beam offers the advantage in that it can easily be used in combination with time-shared multiple traps. In addition, the detection laser can be made to underfill the objective to maximize the collection of light by the opposing condenser objective, while overfilling with the trapping beam yields a high gradient force. However, unlike the trapping beam, the detection laser has to be carefully aligned onto the particle, to ensure detection in the linear regime.

7.2.3 Detector sensitivity β

To use the QPD for position detection, the detector signal needs to be calibrated. This can be done in several ways, for example by moving a particle through the

detection spot with known step sizes using the trapping laser. Alternatively, when using the trapping laser also for detection, scanning the laser very fast over a known distance compared to the trapped particle gives the calibration factor [20].

To determine the detector sensitivity, we used a method which employs the Brownian motion of the particle in the trap [14]. The conversion factor from Volts to meters is expressed in the sensitivity β, and we find for the spectrum S_V measured in Volts:

$$S_V(f) = \beta^2 S_x(f). \tag{7.8}$$

The sensitivity β can be determined by multiplying the PSD (in V^2/Hz) with f^2, giving a plateau for $f \gg f_0$ (for example see Figure 7.3b). From the Equations (7.4) and (7.8), we find that the plateau value P_V, in V^2 Hz, is given by [14]:

$$P_V = \beta^2 \frac{k_b T}{\gamma_0 \pi^2}, \tag{7.9}$$

and thus, with Eq. (7.5): $\gamma_0 = 6\,\pi\,\eta\,r$ for a sphere, we find:

$$\beta = \left(\frac{6\pi^3 \eta r P_V}{k_b T} \right)^{1/2}, \tag{7.10}$$

with η the viscosity and r the radius of the particle.

A disadvantage of using the Brownian motion of the particle for calibration is the necessity to know the particle radius r and temperature T and viscosity η of the medium.

7.3 Experimental setup and methods

7.3.1 Counter-propagating optical tweezers setup

In the setup for combined counter-propagating trapping and independent QPD position detection (Figure 7.1), the TEM_{00} mode of an IR laser (Spectra-Physics, J201-BL-106C, diode-pumped Nd:YVO_4 EOM, 1064 nm, 4 Watt cw) was used for trapping. The beam was split at polarizing beam splitter cube *C2* to be deflected into an inverted and an upright objective by the dichroic mirrors $DM_{i,u}$ (Chroma Technology Corp., 620dcsxr), while the rotation of half-lambda zero-order wave plate *W2* determined the relative power in the two beam paths. In each path, the lenses $L3_{i,u}$ and $L4_{i,u}$ (all $f = 120$ mm) formed a telescope pair for manual control over the beams. The xyz-displacements of the lenses $L3_{i,u}$ — mounted on translation stages and placed at planes conjugate to the back focal planes of the objectives — translated into corresponding displacements of the foci of the beams inside the specimen.

For computer-controlled xy-positioning of the laser focus, a pair of orthogonal AODs (IntraAction, DTD-276HD6 2-axis deflector) was used, making the

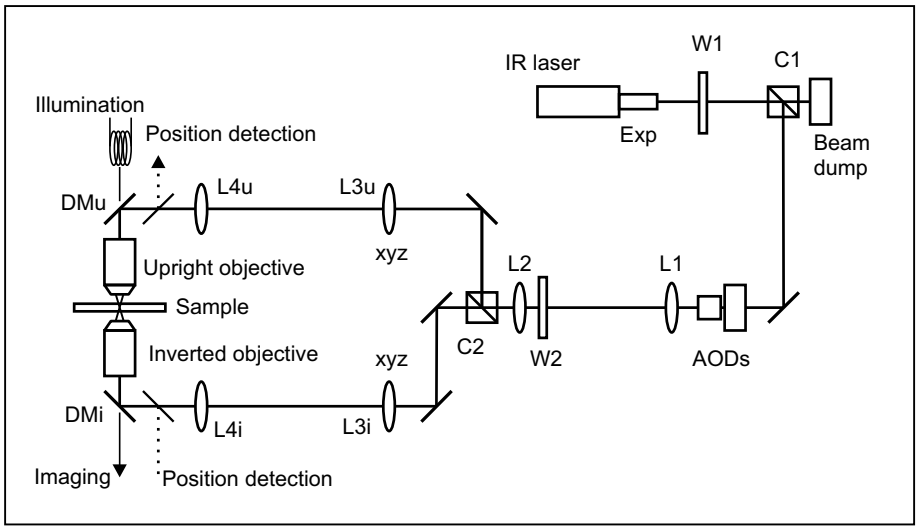

Fig. 7.1: Schematic diagram of the setup for combined counter-propagating trapping and independent quadrant photodiode (QPD) position detection. The QPD part is depicted in more detail in Figure 7.2. The IR laser beam is split at polarizing splitter cube C2, to create counter-propagating traps. AODs enable computer controlled dynamics of the traps and time-shared trapping.

creation of time-shared multiple traps possible. The AODs were placed, mounted on an aligner (NewFocus, 9071-M), in a plane conjugate to the back focal plane of the objectives, and were controlled using a *LabVIEW* program, an interface board (National Instruments, NI PCI-6534), and direct digital synthesizers (DDSs, Novatech Instruments Inc., DDS8m). The signals from the DDSs were amplified (IntraAction, DPA-502D).

The laser beam was expanded to overfill the exit pupil of the trapping objectives. Due to the limited aperture of the AODs, this was done in two steps; before the AODS by a beam expander (Melles Griot, 09LBZ103, 6×), and after the AODs ∼3.8× by the lens pair *L1* and *L2* (Melles Griot, achromat doublets, $f = 65$ mm and $f = 250$ mm, respectively), to a total $1/e^2$ beam waist of 9.6 mm. Any expansion after the AODs limits the lateral range of the AODs in the focal plane by an equal factor.

On the microscope (Leica, DM IRB), the inverted objective was fixed in a mounting block, while a second objective, in upright orientation, replaced the condenser. For alignment, the upright objective was mounted on an xyz-piezo stage (Thorlabs, MDT630), which had a range of 20 μm, in addition to a manual range of 3 mm, in all three directions.

To move the sample with respect to the objectives, an xyz-piezo stage (Physik Instrumente, P-517.3CL, $100\times100\times20\mu m^3$, capacitive sensor) was used.

For long-range travel, the piezo stage was mounted on a home-built stage, which employed two motorized actuators (Newport, 850G-LS, closed-loop, low speed) controlled by a computer board (NI PCI-7344, 4-axis servo/step motion controller).

For imaging, we used a digital charge coupled device (CCD) camera (Uniq Vision, UP-600), and a LabVIEW program that controlled both the camera and the piezo stage, as well as the motorized actuators. A pair of oil immersion objectives (Leica, 100×, 1.30-0.60 NA) and a pair of water immersion objectives (Leica, 63×, 1.2 NA) were available for trapping and imaging.

7.3.2 Quadrant photodiode position detection using a second laser beam

For independent position detection, a HeNe-laser (JDS Uniphase, 1137/P, 633 nm, 7 mW) was incorporated in the optical tweezers setup, together with a QPD (UDT, SPOT-9DMI, 10-mm-diameter active area). The red laser beam, with a $1/e^2$ beam waist of approximately 1 mm at the back focal plane of the objective, was split at polarizing beam splitter cube *C3* (Figure 7.2), at which the vertically polarized light was passed through towards the inverted objective, while the horizontal polarization was reflected into a beam dump. The orientation of half-lambda wave plate $W3$ determined the ratio of powers going into each beam path.

The vertically polarized beam was merged with the inverted trapping beam at dichroic beam combiner mirror BC_i (Chroma Technology Corp., z633bcm), after it passed a pair of telescope lenses ($L5_v$ and $L6_v$, both $f = 140$ mm), used for beam steering. $L5_v$ was positioned in a plane conjugate to the back focal plane of the inverted objective, and mounted on an xyz translational stage. Dichroic mirror DM_i deflected the beam into the inverted objective, which then focused the beam inside the specimen. After passing the upright objective, the beam was coupled out of the trapping laser path by BC_u and imaged onto QPD_v by lens $L7_v$. A bandpass filter (633 nm) was placed in front of the QPD to block ambient light.

The setup can readily be expanded to the use of two QPDs. In this scheme, the horizontal polarized beam is directed towards the upright objective, instead of into the beam dump (dashed beam path in Figure 7.2). The beam follows a similar path as the vertical polarized beam, yet in opposite direction, passing telescope pair $L5_h$ and $L6_h$ (both $f = 140$ mm). The beam is coupled into, and out of, the vertically polarized beam path at polarizing beam splitter cubes *C4* and *C5*, respectively, after which $L7_h$ images the beam onto QPD_h. While wave plate $W3$ determines the ratio of light going into each beam path, an additional waveplate (no drawn) combined with a beam splitter cube can be used for power control. Currently, only QPD_v is used for position detection.

The three signals from the QPD — the difference between the light intensity on the left and the right half (x), the difference between top and bottom signal

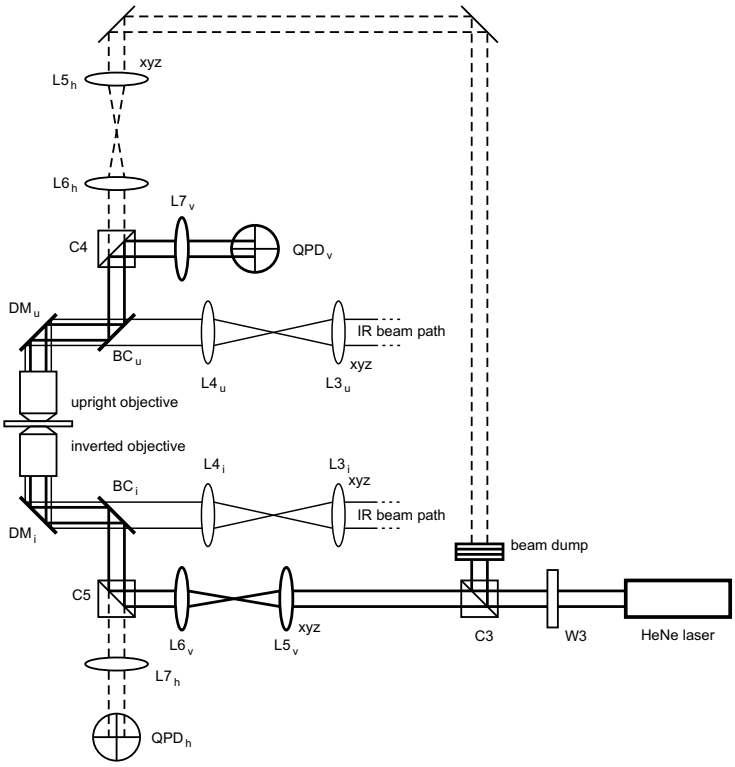

Fig. 7.2: Schematic diagram of the independent QPD position detection. A HeNe laser is split into two orthogonally polarized beams, of which the vertical polarization passes the sample traveling from the inverted to the upright objective to be imaged onto QPD_v. The setup can readily be expanded to the use of double position detection, with horizontal polarized beam (dashed beam path) passing the specimen in counter-propagating direction, to be imaged onto QPD_h.

(y), and the sum over all four quadrants — were first amplified and anti-alias filtered at 20 kHz, before being sampled by a data acquisition board (NI, PXI-6251). A LabVIEW program controlled the sampling, and was used to calculate the power spectra of the x- and y-signal (both divided by the sum signal and with a Hanning window applied to them). A Lorentzian was fitted to these normalized spectra to obtain f_0, from which κ was calculated.

7.4 Results and discussion

Depth dependence of trap stiffness

When using an oil immersion objective in an aqueous specimen, spherical aberrations due to the refractive-index mismatch affect the focus of the beam. This

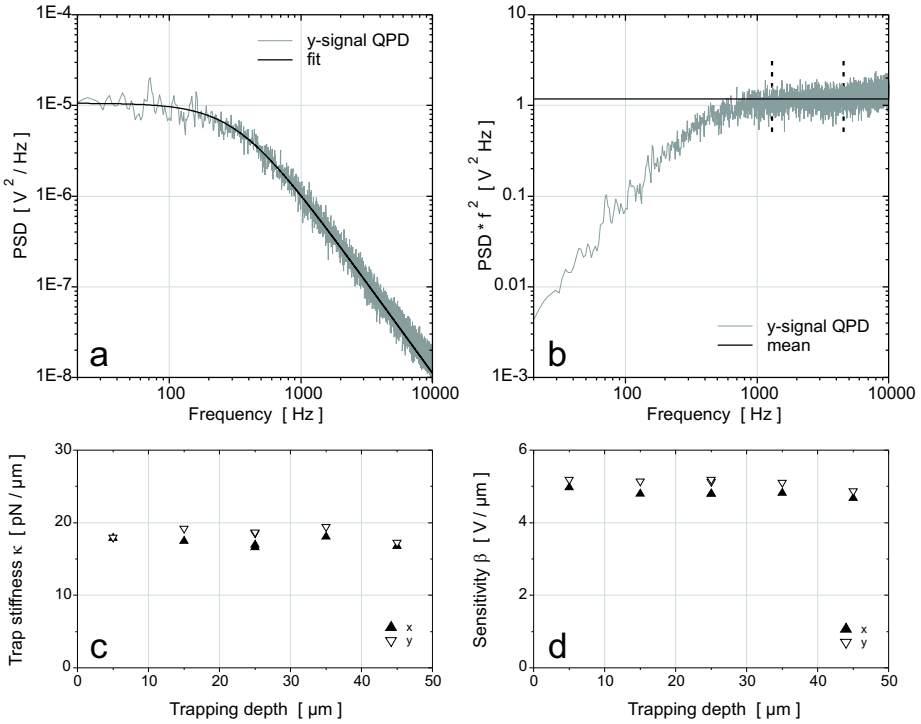

Fig. 7.3: Data for a 1.0-µm-diameter silica particle in water, trapped in inverted tweezers using a water immersion objective. (a) Power spectral density (PSD) for 420 mW at the back focal plane, and a Lorentzian fit to the curve with f_0 = 325 Hz. (b) PSD×f^2 curve, with plateau value P_V = 1.18 V^2 Hz, the mean of the plateau between the two dashed lines. (c) Trap stiffness κ and (d) the sensitivity obtained from the plateau value P_V, for the particle trapped at different depths in the 50-µm-thick sample. (a) and (b) are the data for the y-signal at 15 µm into the sample.

distortion increases with focus depth, causing the stiffness κ [21] and the sensitivity β [20] to decrease (see also Chapter 3).

We used water-immersion objectives when trapping in water to prevent spherical aberrations. As a check whether the ring on the objective to compensate for the thickness of the cover slide was set correctly, we measured the PSD for a 1.0-μm-diameter silica particle trapped in a single-beam gradient trap at several depths. We used the inverted objective for trapping, with a laser power of 420 mW at the back focal plane. Figure 7.3a shows the spectrum of the y-signal, measured at a focal depth of 15 μm. Also shown is the Lorentzian fit to the spectrum, giving a roll-off frequency f_0 of 325 Hz. With a particle radius of 0.5 μm and a viscosity $\eta = 1.0 \times 10^{-3}$, this yields, using Eq. (7.6), a stiffness κ_y of 19.2 pN/μm. In Figure 7.3b, the product of the PSD with

f^2 is plotted, together with the mean of the plateau value $P_V = 1.18$ V^2 Hz, which gives, with Eq. 7.10 and assuming T = 300 K, a detector sensitivity $\beta = 5.14$ V/μm. The stiffness and sensitivity are plotted in Figures 7.3c and d, respectively, for both the x- and y-direction for several depths in the 50-μm-thick sample. The average stiffness in the x-direction is $\kappa_x = 17.3$ pN/μm, while the average $\kappa_y = 18.5$ pN/μm. The average sensitivities are $\beta_x = 4.8$ V/μm and $\beta_y = 5.1$ V/μm. Both κ and β do not show a decrease with depth, indicating minimal spherical aberrations and a correct setting of the compensation ring of the water-immersion objective at 160 μm.

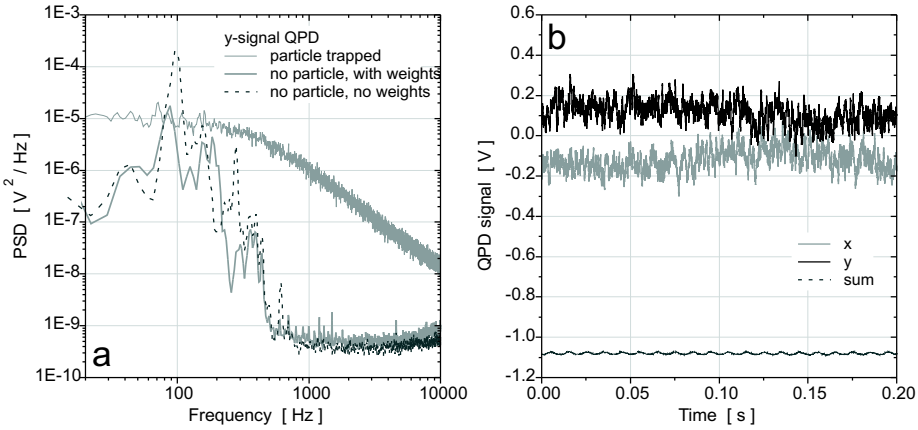

Fig. 7.4: (a) Power spectral density (PSD) curves without a particle in the trap, with and without weights applied to the upright objective holder. The weight clearly decrease the vibrational noise. Also plotted, for comparison, is the PSD from Figure 7.3a. (b) Quadrant photodiode signals (x, y, and sum) for a 1.0-μm-diameter silica particle in water, trapped in inverted tweezers using a water-immersion objective. In the sum signal, 100 Hz noise coming from the ambient tube lights, is visible.

Noise

Figure 7.4a shows PSDs obtained without a particle in the trap. For the lower PSD, weights were applied to the upright objective holder. As can be clearly seen, after removing the weights, the overall noise increased, while certain peaks shifted. This confirms that the noise, with its peak between 20 and 200 Hz, finds its origin in mechanical vibrations of the upright objective with respect to the inverted objective. For comparison, also the spectrum from Figure 7.3a is plotted. This was obtained with the weights applied to the objective holder. The spectrum has a plateau at the noise level; for decreasing plateau values, the noise will show up more. With the use of two high-NA objectives, the

QPD position detection was very sensitive to these vibrational displacements; a typical condenser lens has a large-diameter front lens, while the objective lens that we use as a condenser, has a small front lens of the same size as the inverted illumination objective. This makes it harder to collect the light with the condenser objective, which probably amplifies the effects of vibration.

In Figure 7.4b, the detector signals are plotted from which the spectrum in Figure 7.3a is obtained. The large low-frequency deviation in the x and y signals are due to air currents; the detection laser beam path was not closed off. The 100-Hz noise visible in the sum signal is due to ambient tube light, which came through the laser line bandpass filter in front of the QPD.

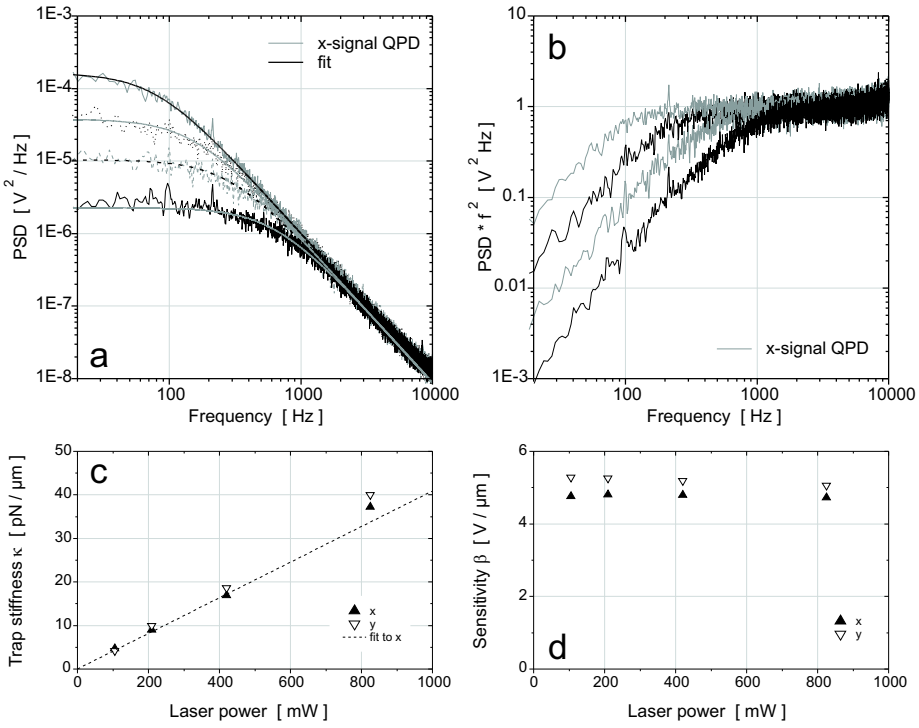

Fig. 7.5: Data for a 1.0-µm-diameter silica particle in water, trapped in inverted tweezers using a water immersion objective. (a) Power spectral density (PSD) curves for the x-signal, for 105, 210, 420, and 825mW at the back focal plane, and Lorentzian fits to the curves with f_0 = 79, 151, 286, and 628 Hz, respectively. (b) The corresponding PSD×f^2 curves. (c) Trap stiffness κ and (d) the sensitivity obtained from the plateau value P_V, for the four powers. In (c) the fit to the first three data points for x is shown (κ = 40.9 pN/µm/W).

Laser power dependence of trap stiffness

In Figure 7.5a, PSDs are plotted of the x-signal for a 1.0-μm-diameter silica particle in water, confined in a single-beam optical trap. The laser power at the back focal plane of the inverted water-immersion objective was varied, from 105, 210, and 420, to 825 mW. Figure 7.5b shows the corresponding PSD$\times f^2$ curves, from which the sensitivities were obtained. For the four powers, κ_x and κ_y are plotted in Figure 7.5c.

The trap stiffness κ is expected to increase linearly with laser power, and for a linear fit to all four data points, we find stiffnesses of 44.0 and 47.6 pN/μm/W, for x and y, respectively. When we fit only to the first three data points, however, we find 40.9 pN/μm/W for the x direction and 44.9 pN/μm/W for y. In Figure 7.5c, the fit to the first three data points is plotted for the x-direction. The fits are forced through zero.

For constant viscosity η, the roll-off frequency f_0 will show a linear dependence on the laser power (Eq. (7.6)). However, Peterman and colleagues [22] showed that the trapping laser heats the suspension, decreasing the viscosity, and consequently increasing f_0. Therefore, if heating is not taken into consideration, the trap stiffness will be overestimated and the detector sensitivity (Eq. (7.10)) underestimated. A higher trap stiffness for high laser power is in accordance with what we see in Figure 7.5c. However, at the highest laser power of 825 mW at the back focal plane of the objective we estimate the power of the truncated Gaussian beam after absorption by the objective to be no more than 200 mW in the laser focus. This is not enough to account for the 10% difference between measured and expected κ. In addition, we do not see a corresponding decrease in the detector sensitivity β (Figure 7.5d). We subscribe the deviation at higher laser power to the high noise level between 20 and 120 Hz in the PSD, which frustrated a good fit to the data. Because the plateau value at low frequencies decreases for increasing power, the noise is more dominant for high than for low trap stiffnesses.

QPD detection and counter-propagating trapping

For counter-propagating trapping, we used two opposing high-numerical aperture water-immersion objectives, and positioned the foci of the two beams in close proximity of each other (see Section 5.3 for the aligning method). This fixed the axial distance between the two objectives.

We used 1.2-μm-diameter TiO_2 particle dispersed in water. The particles had a thin silica shell, and could be trapped in single-beam gradient tweezers. Figure 7.6 shows the data for a particle trapped in counter-propagating tweezers for four powers (with sums of 52, 105, 210, and 412 mW at the back focal planes of the two water-immersion objectives; to partly compensate for a difference in transmittance, 30% of this power was sent to the upright objective and 70% to

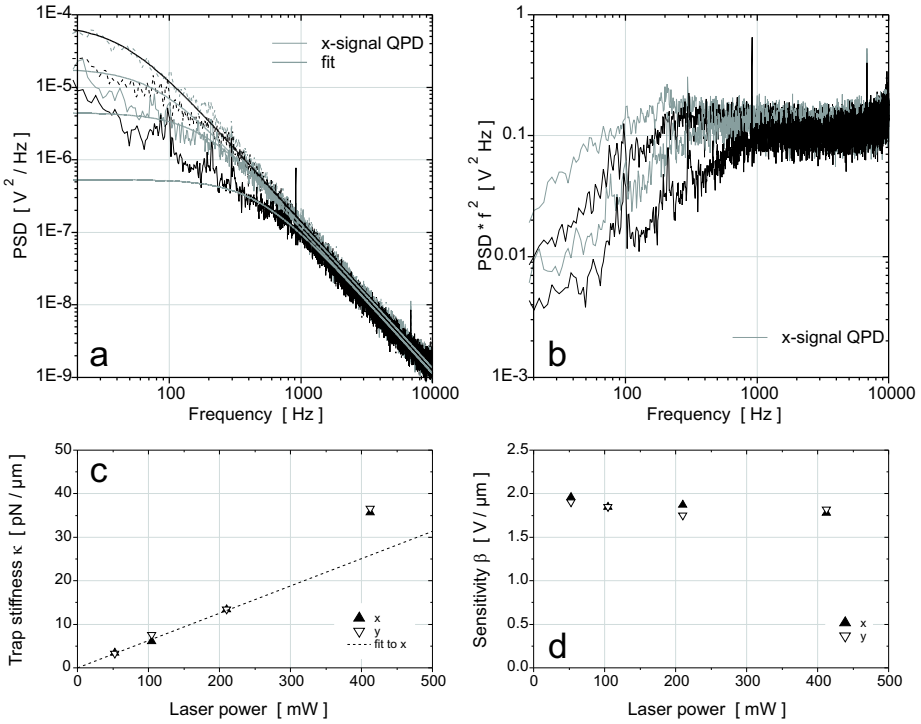

Fig. 7.6: (a) Power spectral density (PSD) curves for a 1.3-μm-diameter TiO_2 particle trapped in water using counter-propagating tweezers. The sums of the laser powers at the back focal planes of the two objectives were 52, 105, 210, and 412 mW. The highest power yields the lowest plateau value. (b) The corresponding PSD$\times f^2$ curves. (c) Trap stiffness κ and (d) the sensitivity obtained from the plateau value P_V, for the four powers. In (c) the fit to the first three data points for x is shown (κ = 62.6 pN/μm/W).

the inverted objective). In Figure 7.6a, the PSDs and the Lorentzian fits to them are plotted for the x-signal, while in Figure 7.6b the corresponding PSD$\times f^2$ curves are shown. The obtained κ_x and κ_y, and the sensitivities are given in the Figures 7.6c and d, respectively. A linear curve, forced through zero, was fitted to the first three data points of Figures 7.6c, giving for the x-direction a slope of 62.6 pN/μm/W, and for the y-direction 65.7 pN/μm/W. The deviation of 40% for the highest laser power is due to a bad Lorentzian fit, as can be clearly seen in Figure 7.6a. The low detector sensitivity is subscribed to the fact that due to the scattering of the particles, not all light is captured by the upright objective; after adjustment of the focus-to-focus distance between the objectives, the plateau value P_V increased to 1 V^2/Hz (not shown), approximately the same level as found for the 1.0-μm-diameter silica particle (Figure 7.5b).

7.5 Conclusions and outlook

We have demonstrated an optical tweezers setup, in which counter-propagating trapping using two high-NA objectives is combined with QPD position detection, enabling force measurements on particles in dual-beam optical tweezers. The use of a separate laser makes position detection on particles in time-shared traps possible. By using two water-immersion objectives, spherical aberrations were prevented, which followed from the constant trap stiffness and detector sensitivity for increasing focal depth. The trap stiffness increased, as expected, linearly with increasing laser power. However, for high laser power, mechanically induced noise frustrated a good Lorentzian fit to the PSD. For high trap stiffness and low sensitivity, the plateau at low frequencies in the PSD drops below the noise level, inhibiting the fitting of a Lorentzian and obtaining the correct trap stiffness. This mechanically induced noise originates for a large part from vibrations of the upper objective and will be improved by better fixation of the objective holder. Due to the small front lens of the condenser objective compared to a conventional condenser, collecting the detection light is more sensitive to the alignment of the objectives, and thus to vibrational noise of the objectives.

In the future, we will expand the setup with a second QPD, with counter-propagating beam directions for the two orthogonally polarized detection laser beams. Crosstalk between the two signals, often a problem with the use of two QPDs, is expected to be very limited with opposing beam directions and cross-polarizations. Double position detection can, for example, be used to measure pair interactions between two particles, or hydrodynamic interactions by cross-correlating the signals from both QPDs [23, 24]. Also, position detection can be done from both sides on the same particle, to identify drift and noise in the signal. Alternatively, the second position detection beam can be directly imaged onto the QPD, to identify the drift in xyz between the two objectives. This can be compensated for by moving the upper objective with the piezo stage on which it is mounted.

At the moment the setup is used in preliminary work to measure high forces exerted in dividing bacteria. In this Chapter, we limited ourselves to characterizing the performance of the counter-propagating tweezers setup combined with independent QPD position detection. In Chapter 8 we will discuss quantitative trap stiffness measurements, including experiments with high-refractive index particles that could not be trapped in single-beam gradient tweezers.

Acknowledgements

I thank Gertjan Verhoeven for help with building the setup, Ahmet Demirörs for synthesis of the 1.3-μm-diameter TiO_2 particles, J.S. Schütz-Widoniak for the

1.1-μm-diameter TiO_2 particles, Jacob P. Hoogenboom for the SiO_2 particles, and Johan Herscheid for programming.

BIBLIOGRAPHY

[1] A. Ashkin, K. Schütze, J. M. Dziedzic, U. Euteneuer, and M. Schliwa. Force generation of organelle transport measured in vivo by an infrared laser trap. *Nature*, 348:346–348, 1990.

[2] L. P. Ghislain, N. A. Switz, and W. W. Webb. Measurement of small forces using an optical trap. *Rev. Sci. Instr.*, 65(9):2762–2768, 1994.

[3] K. C. Neuman and S. M. Block. Optical trapping. *Rev. Sci. Instrum.*, 75(9):2787–2809, 2004.

[4] M. D. Wang, H. Yin, R. Landick, J. Gelles, and S. M. Block. Stretching DNA with optical tweezers. *Biophys. J.*, 72(3):1335–1346, 1997.

[5] A. Meyer, A. Marshall, B. G. Bush, and E. M. Furst. Laser tweezer microrheology of a colloidal suspension. *J. of Microrheology*, 50(1):77–92, 2006.

[6] W. Grange, S. Husale, H.-J. Güntherodt, and M. Hegner. Optical tweezers system measuring the change in light momentum flux. *Rev. Sci. Instrum.*, 73(6):2308–2316, 2002.

[7] S. B. Smith, Y. Cui, and C. Bustamante. Optical-trap force transducer that operates by direct measurement of light momentum. *Methods in Enzymology*, 361:134–162, 2003.

[8] K. Visscher, S. P. Gross, and S. M. Block. Construction of multiple-beam optical traps with nanometer-resolution position sensing. *IEEE J. Sel. Top. Quant. Electronics*, 2(4):1066–1076, 1996.

[9] L. I. McCann, M. Dykman, and B. Golding. Thermally activated transitions in a bistable three-dimensional optical trap. *Nature*, 402:785–787, 1999.

[10] K. Berg-Sørensen and H. Flyvbjerg. Power spectrum analysis for optical tweezers. *Rev. Sci. Instr.*, 75(3):594–612, 2004.

[11] W. Wang, A. E. Chiou, G. J. Sonek, and M. W. Berns. Self-aligned dual-beam optical laser trap using photorefractive phase conjugation. *J. Opt. Soc. Am. B*, 14(4):697–704, 1997.

[12] W. H. Wright, G. J. Sonek, and M. W. Berns. Parametric study of the forces on microspheres held by optical tweezers. *Appl. Opt.*, 33(9):1735–1748, 1994.

[13] J. C. Crocker and D. G. Grier. Methods of digital video microscopy for colloidal studies. *J. Colloid Interface Sci.*, 179:298–310, 1996.

[14] M. W. Allersma, F. Gittes, M. J. deCastro, R. J. Stewart, and C. F. Schmidt. Two-dimensional tracking of ncd motility by back focal plane interferometry. *Biophys. J.*, 74:1074–1085, 1998.

[15] F. Gittes and C. F. Schmidt. Interference model for back-focal-plane displacement detection in optical tweezers. *Opt. Lett.*, 23(1):7–9, 1998.

[16] F. Gittes and C. F. Schmidt. *Signals and noise in micromechanical measurements*, volume 55, pages 129–156. Edited by M. P. Sheetz (Academic, San Diego), 1998.

[17] L. Nugent-Glandorf and T. T. Perkins. Measuring 0.1-nm motion in 1 ms in an optical microscope with differential back-focal-plane detection. *Opt. Lett.*,

29(22):2611–2613, 2004.

[18] E. J. G. Peterman, M. A. van Dijk, L. C. Kapitein, and C. F. Schmidt. Extending the bandwidth of optical-tweezers interferometry. *Rev. Sci. Instrum.*, 74(7):3246–3249, 2003.

[19] G. E. Uhlenbeck and L. S. Ornstein. On the theory of the Brownian motion. *Phys. Rev.*, 36:823–841, 1930.

[20] K. C. Vermeulen, J. van Mameren, G. J. M. Stienen, E. J. G. Peterman, G. J. L. Wuite, and C. F. Schmidt. Calibrating bead displacements in optical tweezers using acousto-optic deflectors. *Rev. Sci. Instrum.*, 77(1):013407, 2006.

[21] P. C. Ke and M. Gu. Characterization of trapping force in the presence of spherical aberration. *J. Mod. Opt.*, 45(10):2159–2168, 1998.

[22] E. J. G. Peterman, F. Gittes, and C. F. Schmidt. Laser-induced heating in optical traps. *Biophys. J.*, 84(2):1308–1316, 2003.

[23] S. Henderson, S. Mitchell, and P. Bartlett. Position correlation microscopy: probing single particle dynamics in colloidal suspensions. *Colloids and Surfaces A*, 190:81–88, 2001.

[24] S. Henderson, S. Mitchell, and P. Bartlett. Direct measurements of colloidal friction coefficients. *Phys. Rev. E*, 64(6):061403, 2001.

8. FORCES EXERTED ON HIGH-REFRACTIVE INDEX PARTICLES IN COUNTER-PROPAGATING OPTICAL TWEEZERS — MEASUREMENTS AND CALCULATIONS

Counter-propagating optical tweezers offer the possibility to stably trap high-refractive index particles that cannot be manipulated using single-beam gradient tweezers. Due to their high index contrast, high forces can be exerted on these particles. In this Chapter, we demonstrate the increase in lateral trap stiffness for high-index titania particles compared to silica particles under the same conditions. In addition, calculations are given for the axial and lateral stiffnesses. We investigated, experimentally and with calculations, the influence of particle size, trapping laser beam width, and alignment, on the trap stiffness, using polystyrene, silica, titania, and gold particles.

8.1 Introduction

The possibility to measure picoNewton-level forces is one of the most exploited features of optical tweezers, applied in various fields. The technique is used in colloid physics [1–3], to study the mechanical properties of (bio-) polymers – such as DNA [4] and microtubules [5] – and measure forces exerted by molecular motors [6, 7]. In these applications, typically, single-beam optical tweezers combined with silica or polystyrene (PS) particles are used, and the maximum forces are limited to ∼100 pN.

Due to a larger refractive-index difference with the surrounding medium, high-refractive index particles, such as titania, or metal particle, such as silver, hold the promise of providing a higher trap stiffness, and thus to be able to exert higher forces than lower-index particles under the same conditions. This expected higher trap efficiency, a measure for the trapping force per laser power, is useful when the available laser power is limited, or when laser-induced damage plays a role, for example in biophysical experiments on living materials [8, 9].

For particles with a refractive index n_p higher than the index n_m of the surrounding medium, the large intensity gradient in a tightly focused laser beam provides the necessary force to balance the destabilizing scattering force [10]. In the Rayleigh regime, an increase in n_p or in the radius R of a particle, yields an increase in both these force components. The dependence on R and on $m = n_p/n_m$, however, is stronger for the scattering force ($\sim R^6[m^2\text{-}1]^2/[m^2\text{+}2]^2$) than for the gradient force ($\sim R^3[m^2\text{-}1]/[m^2\text{+}2]$). This limits the size and index of particles that can be trapped in a single-beam gradient trap, and with this, a limit is set to the trapping force of single-beam optical tweezers. By using a second, opposing, trapping beam, counter-propagating traps [11, 12] can be created in which the destabilizing scattering forces are cancelled, and high-refractive index particles can be trapped that cannot be confined in a single-beam gradient trap. As a rough estimate of the enhancement of trap stiffness we can expect, we use the Rayleigh theory and find, for a high-refractive index titania particle ($n = 2.4$) compared to an equally-large polystyrene (PS) particle ($n = 1.57$) in water ($n = 1.33$), an increase of 2.6× in gradient force.

Exact calculations of the optical forces, however, are not straightforward, as the sizes of trapped objects are typically in the range of the wavelength λ of the trapping laser light used. For dielectric particles with a diameter d much larger than the wavelength ($d \gg \lambda$), geometric optics (GO) apply [13–17], while for $d \ll \lambda$, the Rayleigh scattering theory can be used [18]. For $d \simeq \lambda$, however, neither GO nor the Rayleigh theory are sufficient to describe the forces in 3D on a dielectric particle in a tightly-focused laser beam. To calculate trapping forces in the intermediate regime, several approaches have been explored [19–23]. Exact partial-wave (Lorenz-Mie) expansions are reported for the axial force component [24], and for the three-dimensional case [25]. Here, a full so-called

Mie solution of plane waves interacting with a (metallo-)dielectric particle is used, in addition to a description of the tightly focused laser beam.

The ability to perform reliable calculations enhances the possibility to tune the experimental setup and optimize the desired properties, for example in choosing the microscope objectives, the trapping laser wavelength, and the particles and medium used, to achieve high forces, a high trap stiffness, and/or a high detector sensitivity.

In this Chapter, we describe experiments in which we trapped high-refractive index particles in counter-propagating tweezers, and determined the enhancement of trap stiffness by obtaining the roll-off frequency from the power spectral density curve of the quadrant photodiode (QPD) signal. The particles used varied from silica and polystyrene particles that could be confined in 3D in a single-beam trap, to high-refractive index titania particles and gold particles that we were only able to trap in counter-propagating tweezers. We use high-numerical aperture (NA) objectives, and overfill the back aperture of these objectives, to maximize the forces exerted on the particles and compare the results of these measurements with calculations based on the approximation given by Maia Neto and Nussenzveig [24] and Mazolli *et al.* [25]. In addition, we use calculations to gain an understanding of the effects of experimental parameters — such as the axial distance between the two trapping beams, the refractive-index difference, and the objectives used — on the trapping position, and the lateral and axial trap stiffness of a particle in optical tweezers.

8.2 Experimental setup and methods

8.2.1 Calculation of forces in optical tweezers

The force F exerted by a laser beam onto a particle is proportional to the power P of the laser beam. This is expressed by the trap efficiency Q of the system:

$$Q = \frac{c}{n_m}\frac{F}{P}, \tag{8.1}$$

where c is the speed of light and n_m the index of refraction of the medium.

To calculate the trap efficiency Q in three dimensions for a particle trapped in optical tweezers, we used the explicit partial-wave Mie expansion given by Mazolli *et al.* [25], which was first derived for the axial direction by Maia Neto and Nussenzveig [24]. In their approach, the laser beam is represented as a superposition of electromagnetic plane waves, which correctly describes a focused beam with large opening angle. The scattering of each of these plane-wave components by the (metallo-)dielectric sphere is taken into account, and analytical results are derived. The parameters that are used in the calculations are the wavelength λ of the trapping beam, the refractive index of the medium n_m and of the particle n_p, the radius R of the particle, the opening angle θ_0 of the beam

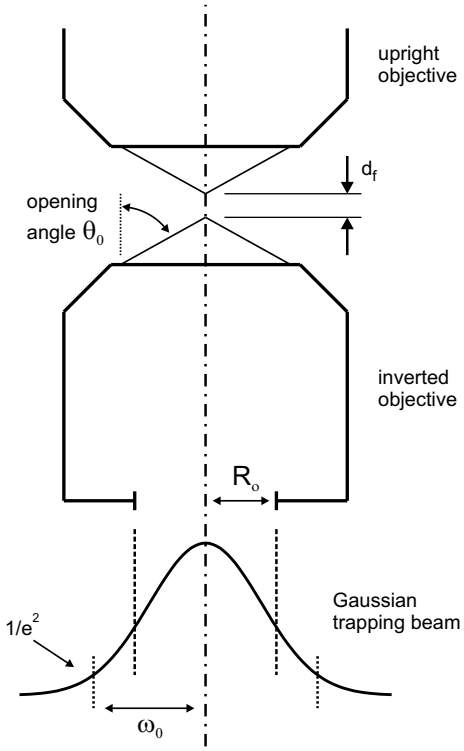

Fig. 8.1: Parameters used in the calculations. A Gaussian trapping beam, with a $1/e^2$-beam waist ω_0, is truncated by the opening at the back of the objective with radius R_o. The beam is focused with opening angle θ_0, and d_f is the distance between the two foci.

in the medium, and γ, a measure for the truncation of the Gaussian trapping beam at the objective. For γ we find (see Appendix, Section (8.5)):

$$\gamma = (n_m R_o)/(\mathrm{NA}\omega_0), \tag{8.2}$$

with R_o the radius of the opening at the back of the objective, NA the numerical aperture, and ω_0 the $1/e^2$-beam waist of the beam (see Figure 8.1). The opening angle θ_0 of the focused beam is given by:

$$\theta_0 = \arcsin\left(\frac{\mathrm{NA}}{n_m}\right). \tag{8.3}$$

The trap stiffness κ is defined as the force per displacement of the trapped particle at the trapping position, which, for one direction, reads as:

$$\kappa_x = F_x/x. \tag{8.4}$$

Because our two counter-propagating beams are orthogonal polarized, no interference is expected, and the calculation results for the two individual beam can be added to obtain the calculated force for the counter-propagating tweezers. In addition, a circular polarized beam is assumed in the calculations, while in our experiments we used linear polarized beams. For circular polarized light the lateral trap stiffness does not depend on the lateral direction ($\kappa_x = \kappa_y$). For a linear polarized beam, the trap stiffness in the direction perpendicular to the polarization is larger compared to the stiffness in the parallel direction [26]. This difference, however, is limited for particles with sizes comparable to the wavelength [26], and the approximation of circular polarized light can be used.

Spherical aberrations due to a refractive index mismatch between the immersion fluid of the objective and the medium in which the particle is dispersed, are not taken into account (see also Chapter 3). Moreover, a dependence of the transmittance of the objective on the radial distance to the optical axis, as shown by Viana *et al.* [27], is not taken into consideration in these calculations as well; a uniform transmittance is assumed. These issues will contribute to the discrepancy between experimental results and calculations.

To investigate how the trap stiffness is affected by the size and the refractive index of a particle, and by the shape of the trapping beam, we will focus on the differences in force and stiffness between different configurations, rather than comparing calculated and measured absolute forces.

8.2.2 Experimental setup

An infrared laser (Spectra-Physics, 1064 nm, 4 Watt cw) was split at a polarizing beam splitter cube and sent to two opposing high-NA objectives to create counter-propagating tweezers. The setup is described in more detail in Chapter 7. A separate HeNe detection laser (JDS Uniphase, 633 nm, 7 mW), combined with a QPD (UDT, SPOT-9DMI) was used to obtain a power spectral density (PSD) curve of the positional signal of a particle in the tweezers. By fitting a Lorentzian to this curve, the roll-off frequency f_0 was found [28]. From f_0, the trap stiffness κ for a spherical particle was calculated with:

$$\kappa = 12\pi^2 \eta R f_0, \tag{8.5}$$

with η the viscosity of the medium and R the particle radius.

When trapping in water ($n_m = 1.33$), two water-immersion objectives (Leica, 63× 1.2 NA) were used. With Eq. (8.3) we find $\theta_0 = 64.5°$. The water-immersion objectives have an R_o of 4.7 mm, and with the $1/e^2$-radius of 4.8 mm for the trapping beam, this yields a γ of 1.09 (Eq. (8.2)). For these two objectives, a large difference in trap stiffness was observed for comparable laser powers. This is attributed to a difference in transmittance between the objectives.

For one experiment, two oil-immersion objectives (Leica, 100× 1.4 NA) were

used to trap in ethanol ($n_m = 1.36$). This was done with the setup described in Section 2.2, for which the trapping beam had a $1/e^2$-radius of 2.8 mm. The objectives had an opening with $R_o = 3.4$ mm. However, because the NA of the objective exceeded the refractive index of the medium, total internal reflection occurred (see also Chapter 3), which makes the use of Eq. (8.2) invalid. We estimated the effective NA to be 1.3. By scaling R_o with the same factor, we then found $\gamma = (1.36 \times 3.157)/(1.3 \times 2.8) = 1.18$, and $\theta_0 = 72.9°$. On this setup, the QPD position detection was done using the fraction ($\sim$1%) of the IR trapping beam that leaked through the dichroic mirror. The QPD was placed at the front camera port of the microscope. Using the trapping beam for detection has an advantage in that the laser is always aligned with the particle. However, with the use of IR laser light in combination with the QPDs, the PSD is underestimated at high frequencies [29], because the response time of the QPD is decreased for IR light.

8.2.3 Colloidal dispersions

We used a dispersion of 1.1-μm-diameter titania particles [30] and 1.4-μm-diameter SiO_2 particles in ethanol ($n = 1.36$). The synthesis of the silica particles is described elsewhere [31–33]. The titania particles had a refractive index n of approximately 2.4. In addition, we used a mixture of 2.17-μm-diameter and 4.1-μm-diameter polystyrene (PS) particles (Spherotech Inc., SVP-20-5 and SVP-40-5, respectively) dispersed in water ($n = 1.33$). The PS particles ($n = 1.57$) were streptavidin-coated, which was not expected to influence our measurements. The 200-nm-diameter gold colloids in water were obtained from Ted Pella, Inc.

The sample cells were prepared by sealing two cover slides (Menzel No. 1) together with candle wax. For sturdiness, some sample cells were glued together on two sides using UV-curing glue, before they were filled and sealed off with candle wax.

8.3 Results and discussion

8.3.1 Refractive-index dependence of the trap stiffness

To investigate the increase in trap stiffness for increasing refractive-index contrast, we used a dilute dispersion of 1.1-μm-diameter TiO_2 particles ($n = 2.4$) and 1.4-μm-diameter SiO_2 ($n = 1.45$) in ethanol. Because the titania particles could not be confined in a single-beam gradient trap, we used counter-propagating tweezers in these measurements. The powers inside the traps were 22, 44, 88, and, only for the titania particle, 176 mW. In Figure 8.2a, the corresponding PSDs are given; for clarity, only one curve (44 mW) is plotted for the silica particle. For this estimated power of 44 mW in the focal region, the

sum of the powers before entering the objectives was 110 mW. At this power, f_0 was 499 Hz for the 1.1-μm-diameter TiO_2 particle, and with $\eta = 1.2\times10^3$ Ns/m^2 for ethanol, this yields a stiffness $\kappa_x = 39$ pN/μm. The trap stiffness increased linearly with increasing laser power. Because of the large amount of (mechanical) noise in the curves for the 1.4-μm-diameter SiO_2 particle, we fitted the Lorentzians manually. Assuming for the three curves an increase in stiffness linear with laser power, we found at 44 mW an f_0 of approximately 115 Hz, corresponding to $\kappa_x = 11.4$ pN/μm, thus a factor 3.4 lower stiffness than for the smaller titania particle.

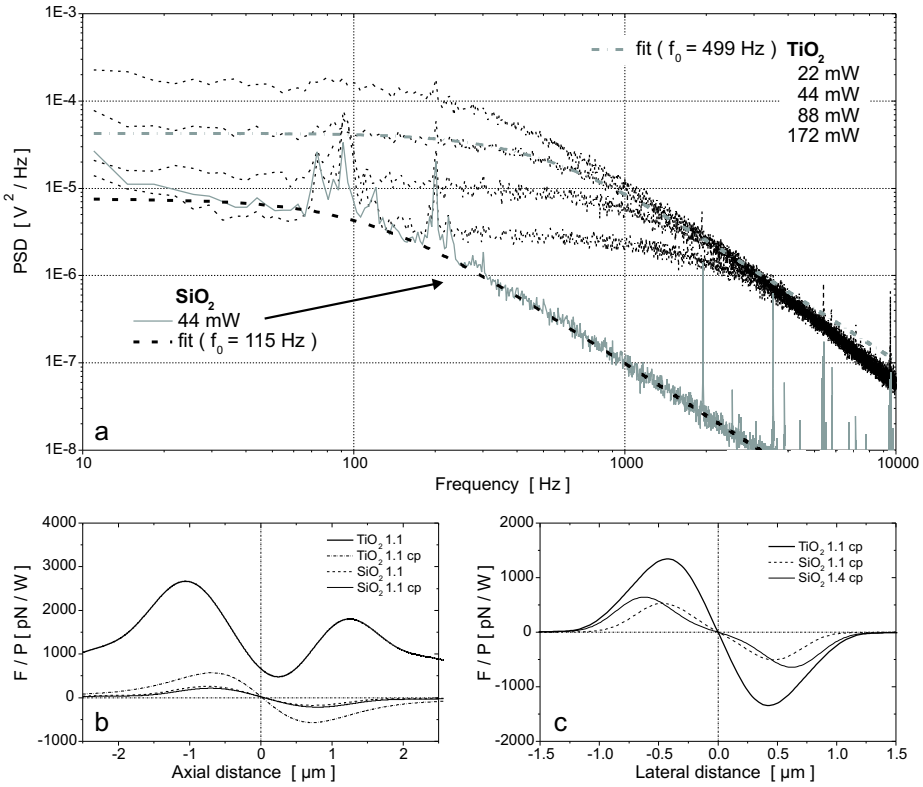

Fig. 8.2: Measured and calculated data for 1.1-μm-diameter TiO_2 and 1.4-μm-diameter SiO_2 particles. (a) Measured power spectral density (PSD) curves for TiO_2 and SiO_2 in counter-propagating (cp) traps, from which, for P = 44 mW in the sample, the trap stiffnesses $\kappa_x = 39$ pN/μm (TiO_2) and 11.4 pN/μm (SiO_2) were obtained. (b) Calculated axial trapping force F_z. (c) Calculated lateral trapping force F_{xy}.

Figure 8.2b shows the calculated axial trapping force per W laser power, for 1.1-μm-diameter TiO_2 and SiO_2 particles in single-beam and in counter-propagating traps. Stable trapping occurs at the position where F = 0 and the curve has a negative slope. In a single-beam gradient trap, a 1.1-μm-diameter

silica particle will be trapped near the laser focus, whereas for a titania particle, no stable trapping occurs. For the silica particle, we find that the curve for dual-beam trapping does not differ much from the curve for single-beam trapping, which is in accordance with the small role played by the scattering force due to a small refractive index contrast between silica and ethanol. For the TiO_2 particle in the dual-beam trap, however, we now find a stable trapping position. In Figure 8.2c, the calculated lateral trapping force per W laser power is plotted for a 1.1-μm-diameter TiO_2 particle and for silica particles (1.1 and 1.4 μm in diameter) in counter-propagating traps.

Tab. 8.1: Comparison of the calculated and the measured trap stiffnesses $\kappa_{x,y}$ and κ_z (in pN/μm/W), between 1.1-μm-diameter TiO_2 and SiO_2 particles, and between 1.1-μm-diameter TiO_2 and 1.4-μm-diameter SiO_2 particles. All results for counter-propagating trapping mode in ethanol.

Particle	*measured* $\kappa_{x,y}$	*calculated* $\kappa_{x,y}$	*calculated* κ_z
TiO_2 1.1 μm	355	4844	1354
SiO_2 1.4 μm	104	688	250
Factor	3.4×	7.0×	5.4×
SiO_2 1.1 μm	n.a.	1176	455
Factor	n.a.	4.1×	3.0×

The calculated and measured stiffnesses are given in Table 8.1. We measured a 3.4× higher trap lateral stiffness for the titania particle compared to the larger silica particle. The calculated enhancement is 7.0× in the lateral direction and 5.4× in the axial direction. Comparing with an equally-sized silica particle we find a calculated enhancement of 4.1× and 3.0× for the lateral and axial trap stiffness, respectively. Note that the trap stiffness is larger for 1.1-μm silica particle than for the 1.4-μm one. In the next Section we will further discuss the complex size dependence of the trap stiffness.

When comparing the absolute values between the measurement and the calculations, we see large differences. The spherical aberrations — due to the refractive index mismatch between the immersion oil/glass ($n = 1.52$) and the ethanol ($n = 1.36$) — affect the stiffness, and are not taken into account in the calculations. In addition, the absorption of light by the objective is not taken into consideration either. A relatively low transmittance at the edge of the objective, as reported by Viana *et al.* [27], will decrease the trap stiffness even further. Due to these effects, the calculations overestimate the trap stiffness in axial and radial direction.

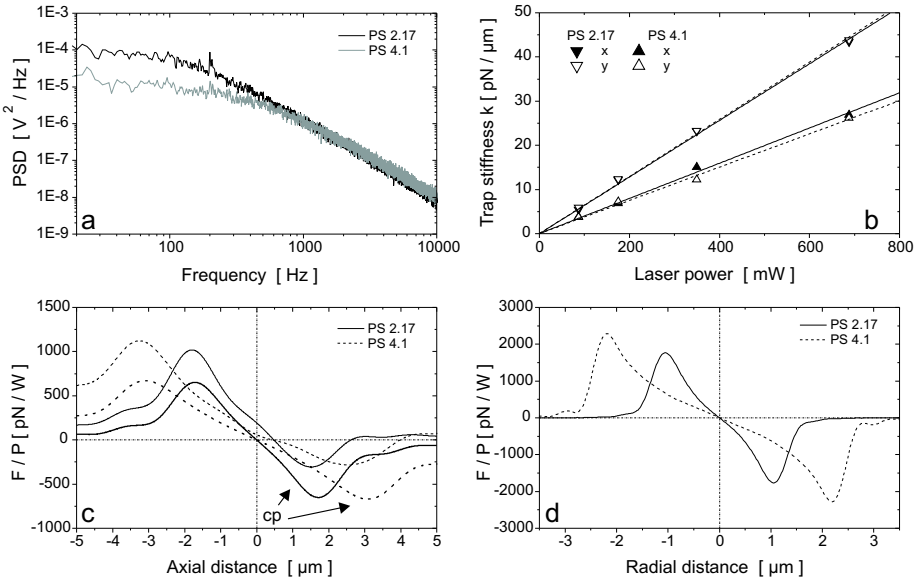

Fig. 8.3: Measured and calculated data for 2.17-μm-diameter and 4.1-μm-diameter polystyrene (PS) particles in water, trapped in counter-propagating tweezers. (a) The measured power spectral density (PSD) curves for the x-direction with 1.65 W total laser power (2.17 μm in black, 4.1 μm in gray). (b) Measured trap stiffnesses κ_x and κ_y at four laser powers, for both sizes PS particles. Linear fits are forced through zero. (c) Calculated axial trap efficiency Q_z on the beam axis for both particles. (d) Calculated radial trap efficiency Q_x at the trapping position $z = 0$ μm.

8.3.2 Size dependence of the trap stiffness

To illustrate the dependence of the trap stiffness on the size of the trapped particle, we used a dispersion of 2.17-μm-diameter and 4.1-μm-diameter PS in water. (See also, however, the results of the calculations for the silica particles in the previous Section.) Two water-immersion objectives were used to create counter-propagating traps, with laser powers of 90, 175, 350, and 690 mW (this being the sum of the powers of the two beams before entering the objectives).

Figure 8.3a shows the PSDs for the two PS particles for a total laser power of 690 mW. From the PSDs, the roll-off frequency f_0 was obtained, after which Eq. (8.5) yielded the lateral trap stiffnesses $\kappa_{x,y}$, which are plotted in Figure 8.3b. Linear fits, forced through zero, gave $\kappa_x = 64$ and $\kappa_y = 65$ pN/μm/W for the 2.17-μm-diameter particle and $\kappa_x = 40$ and $\kappa_y = 38$ pN/μm/W for the 4.1-μm particle; a factor 1.6 and 1.7 difference in the x- and y-direction, respectively.

Figure 8.3c shows calculations of the axial trapping force F_z for single-beam and counter-propagating trapping. The trap stiffness is 362 and 185 pN/μm/W

for the 2.17-μm and the 4.1-μm-diameter particle, respectively; a factor 2.0 difference. The calculated lateral trapping forces are given in Figure 8.3d. We find 1119 pN/μm/W and 609 pN/μm/W, for the 2.17-μm and the 4.1-μm-diameter particle, respectively; a factor 1.8 difference, and comparable to the measured 1.6× and 1.7× for the x- and y-direction.

For small particle sizes, the trap stiffness increases with the diameter of the particle [13]. The highest trap stiffness is expected for particles with a diameter comparable to the expected lateral extent of the focus, $\sim$0.8 μm [26], while for larger particles, the stiffness decreases for increasing diameter. Our results for the 2.17-μm and 4.1-μm-diameter PS particles — both considerably larger than our laser focus, and clearly not in the Rayleigh regime — are in accordance with this, just like the results for the 1.1-μm and 1.4-μm-diameter silica particles in the previous Section.

The large absolute difference between the measurements and calculations can (partly) be accounted for by the objective transmittance, which is not considered in the calculations. Spherical aberrations are not expected to play a significant role, because water-immersion objectives were used to trap in water.

8.3.3 Trap alignment dependence of the trap stiffness

To create counter-propagating dual-beam optical tweezers, the two laser beams are aligned with respect to each other. We investigated the dependence of the trap stiffness on the alignment of the two beams in the axial (z) direction, by trapping a 2.17-μm-diameter PS particle in counter-propagating tweezers and displacing the foci with respect to each other along the beam axis.

We started with the foci of the two beams approximately coinciding, and then changed the distance d_f between the foci by moving the inverted objective upwards in steps of -2 μm. At each position, we obtained PSDs and from these, determined the lateral trap stiffness $\kappa_{x,y}$ (Figure 8.4a). The stiffness first increased for $d_f = -2$ μm and then slightly decreased ($d_f = -4$ μm). The particle was trapped in between the two foci, which was checked in the camera image by alternatingly blocking one of the beams and seeing the particle jump to one of the foci. For $d_f = -6$ and -8 μm, the particle was trapped close to one of the beam foci, and $\kappa_{x,y}$ was strongly reduced. Qualitatively, these results are in agreement with calculations. In Figure 8.4b the calculated axial and lateral trap stiffness are plotted as a function of the distance d_f between the foci, for a 2.17-μm-diameter PS particle in water. For the solid lines, the particle is trapped in between the two foci, while the dashed parts on either side of the curves indicate trapping near one of the foci. At $d_f = -3$ μm, we see a sudden drop in the lateral trap stiffness, when the particle can no longer be trapped in between the foci.

For relatively small deviations away from $d_f = 0$ μm, the lateral stiffness does not change much. Related to this is the independence of the lateral trap

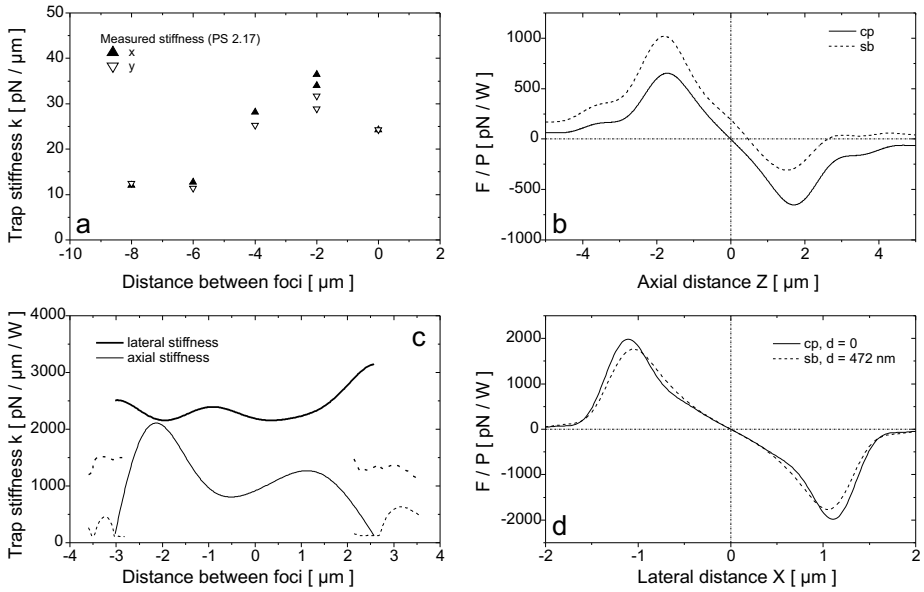

Fig. 8.4: Measured and calculated data for a 2.17-μm-diameter PS particle in water. (a) Measured lateral trap stiffness for varied distance d_f between the foci. Negative values indicated that the inverted focus was located above the upright focus. (b) Calculated dependence of the axial and lateral trap stiffnesses on d_f. The dashed parts in the curve indicate the stiffness when the particle is not trapped in between the two foci, but near or at one of the two foci (for d_f far from 0). (c) Calculated axial trapping force. (d) Calculated lateral trapping force for single-beam (sb) and counter-propagating (cp) trapping, at the axial trapping position (0 μm for cp and 0.47 μm for sb).

stiffness for this particle on whether a single-beam trap is used or counter-propagating tweezers, even though the particle is trapped at a considerable distance from the focus when trapped in single-beam tweezers. In Figure 8.4d, the calculated lateral force perpendicular to the beam axis is plotted for a 2.17-μm-diameter PS particle in counter-propagating tweezers (trapping at $z = 0$ μm) and in a single-beam gradient trap ($z = 0.47$ μm). For high-refractive index titania particle (1.1 μm in diameter) we find similar results, in that for small misalignments along the beam axis, the trap stiffness does not differ much. For a misalignment of 0.45 μm we calculated a difference of 2% in stiffness for a titania particle in water (data not shown).

For counter-propagating trapping with coinciding foci, also the axial trap stiffness is not significantly different as compared to single-beam optical trapping (Fig. 8.4c). Changing the distance d_f between the foci, though, does increase the axial stiffness for both positive and negative d_f (Fig. 8.4b). The axial force (Fig. 8.4c) does not have its steepest part at $d_f = 0$ μm, and by sliding the beams with respect to each other, trapping can take place with high

trap stiffness.

The exact shape of the trap stiffness dependence on d_f, is affected by the size and index of the particle and by the trapping beams. However, Figure 8.4 indicates that by tuning the parameters of the setup, features like the axial trap stiffness can be optimized.

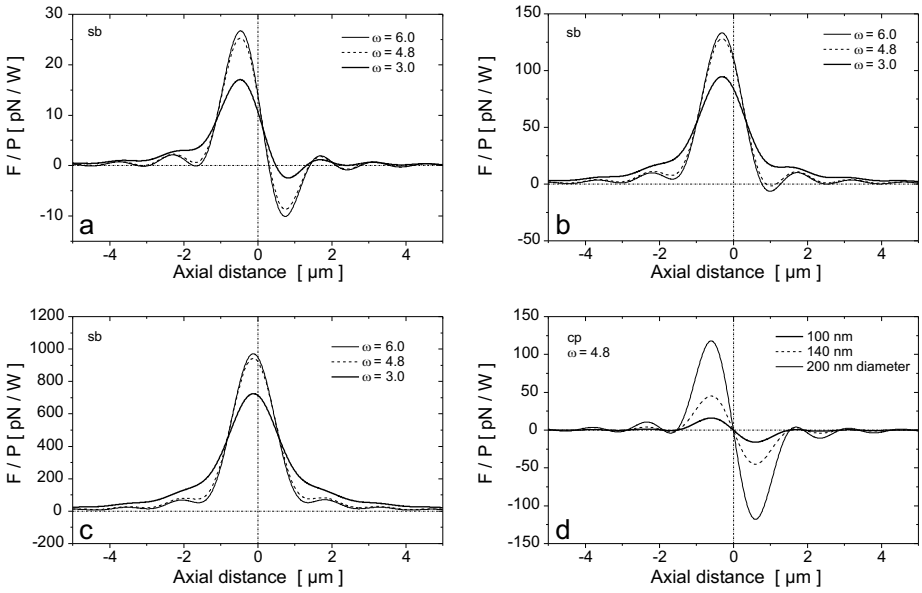

Fig. 8.5: (a–c) Calculated axial trapping force F_z along the beam axis for gold particles in a single-beam (sb) gradient trap. Results for three beam waists are shown: $\omega_0 = 3.0$ mm ($\gamma = 1.74$), $\omega_0 = 4.8$ mm ($\gamma = 1.09$), and $\omega_0 = 6.0$ mm ($\gamma = 0.87$), for particles with diameters of (a) 100 nm, (b) 140 nm, and (c) 200 nm. In (d) the axial trapping force is given for the three particles in counter-propagating (cp) tweezers ($\omega_0 = 4.8$ mm). The trap stiffnesses κ_z are 43, 121, and 317 pN/μm/W, for the 100-nm, 140-nm, and 200-nm-diameter particle, respectively.

8.3.4 Numerical aperture dependence of the trap stiffness

Recently, Hansen and colleagues [34] demonstrated the stable 3D trapping of large (254 nm diameter) gold particles in a single-beam gradient trap. They used oil- and water-immersion objectives, and stressed the importance of only slightly overfilling the back aperture of the objective, and not loosing the tails of the Gaussian beam at any other optics.

The high effective NA of a trapping beam, necessary to create a large intensity gradient in the axial beam direction, does not only depend on the NA of the objective lens, but also on the filling of the exit pupil (EP) by the Gaussian laser beam. The filling of the EP is expressed in the parameter γ (see Appendix,

Section 8.5). When overfilling (the $1/e^2$-beam waist larger than the radius of the opening at the back of the objective), less laser power enters the objective. However, the intensity at the edge of the EP is increased as compared to the maximum intensity, increasing γ. For underfilling of the objective, the effective NA of the trapping beam and γ are decreased.

To investigate the dependence of the effective NA on the trapping of gold particles, we calculated the axial trapping force for several configurations. Figure 8.5 shows calculation for gold particles of various sizes in a single-beam gradient trap, for three $1/e^2$-beam waists ω_0. We used the parameters valid for our experimental setup with water-immersion objectives ($\omega_0 = 4.8$ mm, $\gamma = 1.09$), and for underfilling ($\omega_0 = 3.0$ mm, $\gamma = 1.74$) and overfilling ($\omega_0 = 6.0$ mm, $\gamma = 0.87$) of the objective. The opening angle θ_0 was 64.5°.

In Figure 8.5a, the results for a 100-nm-diameter Au particle show a stable axial trapping position for all three ω_0 values. For a 140-nm-diameter gold particle (Figure 8.5b), however, no trapping position can be found for $\omega_0 = 3.0$ mm. In Figure 8.5c, the calculations show no stable axial trapping of a 200-nm-diameter Au particle for either of the three beams, contrary to the experimental results of Hansen *et al.* [34]. In general, the calculations show a better trappability for a higher effective NA due to more overfilling.

We attempted to trap 200-nm-diameter gold particles, dispersed in water, using a single-beam gradient trap. We did not succeed, neither with an oil-immersion objective, nor with a water-immersion objective. The lenses and laser beam used are comparable with our tweezers setup, and we have no explanation for the difference in trapping ability.

We were able to trap the 200-nm-diameter gold particles in counter-propagating optical tweezers, with water-immersion objectives as well as with oil-immersion. We used a laser power of 100 mW , measured before entering the objectives. The calculated trapping forces in counter-propagating traps using water-immersion objectives, are plotted for the three sizes of gold particles in Figure 8.5d. All three particles have a stable trapping position at the position of the overlapping foci. The trap stiffnesses are 43, 121, and 317 pN/μm/W for the 100-nm, 140-nm, and 200-nm-diameter particles, respectively. Compared to the result for a 200-nm-diameter PS particle under the same conditions ($\kappa_z = 36$ pN/μm/W, data not shown), this is a factor >8 enhancement of the trap stiffness.

By using counter-propagating tweezers to trap gold particles, a lower laser power is needed to obtain the same trap stiffness as compared to single-beam tweezers. Recently, Seol and colleagues [35] demonstrated local heating of 266 °C/W, for a 100-nm-diameter Au particle in water, using a 1064-nm laser beam. Therefore, the counter-propagating trapping of gold particles with low laser power can be advantageous to limit laser heating.

8.4 Conclusions and outlook

We have experimentally demonstrated a >3× increase in lateral trap stiffness for high-refractive index 1.1-μm-diameter titania particles as compared to 1.4-μm-diameter silica particles. Due to their high index, these titania particles could not be trapped in single-beam gradient traps. In addition, we calculated the stiffness dependence of a 2.17-μm-diameter PS particle and a 1.1-μm-diameter titania particle in counter-propagating tweezers on the distance d_f between the two foci, showing that for small misalignments along the beam axis, the changes are moderate. The limited change in the lateral trap stiffness is also seen when comparing trapping in single-beam and in counter-propagating beam traps for a 2.17-μm-diameter PS particle. This indicates that, when trapping with high-NA objectives, most improvement in trap stiffness is to be expected from the counter-propagating trapping of high-index particles that cannot be confined in single-beam gradient tweezers.

We reported the trapping of 200-nm-diameter gold particles in counter-propagating tweezers, but were not able to confine these particles in a single-beam gradient trap. Calculations show the dependence of the trappability of different sizes of gold particles on the effective NA of the trapping beam; when overfilling more, gold particles of larger sizes can be trapped. The calculated trap stiffness of gold particles in counter-propagating tweezers indicate a factor >8 enhancement as compared to a PS particle, for a diameter of 200 nm. When trapping gold particles, local heating has to be taken into consideration.

The absolute difference between calculated and measured stiffnesses are large. Apart from spherical aberrations due to a refractive index mismatch between the medium and the immersion fluid, the calculations do not take the transmittance of the objective into account. The fact that our two water-immersion objectives show considerable difference in trap stiffness for comparable circumstances, is an indication of the importance of (individual) objective lens properties.

In conclusion, we showed different aspects of the dependence of the axial and lateral trap stiffness on particle size, refractive index difference, focus shape and axial alignment of counter-propagating dual-beam traps. By tuning the parameters, the setup configuration can be optimized, for example in maximum axial or lateral stiffness, for the desired application. Accurate calculations of the forces on particles in optical tweezers are an important tool in the understanding, and tuning, of optical trapping.

Maximizing the trapping stiffness finds its use in bio-physical experiments where high forces are expected. We also plan on investigating the possibilities of using silicon particles. A 1-μm-diameter Si (n=3) particle, for example, has an expected lateral trap stiffness of 6.2 pN/μm/mW, compared to 1.0 pN/μm/mW for an equal-sized PS particle. The Si particles can be coated with silica, and

subsequently functionalized.

Acknowledgements

I would like to thank Peter van Oostrum for the radial force calculations, Alexander Moroz for the program to calculate the axial forces, and Gertjan Verhoeven for useful discussions.

8.5 Appendix — Determining the parameters γ and ω_0

The parameters that are used in the calculations of Neto and Nussenzveig [24] are the wavelength of the laser beam λ, the radius of the particle r, the refractive index of the particle n_p and of the medium n_m. Usually, the Gaussian (TEM_{00}) transverse laser mode is used for optical trapping. In the calculations, the trapping beam is parameterized by γ, a measure for the form of the truncated Gaussian beam that enters the objective and is focused inside the sample, and by θ_0, the opening angle of this focused beam inside the sample.

To determine γ, we look at the radial intensity I of a Gaussian beam, which varies as [36]:

$$I(r) = I_0 \exp(-2r^2/\omega_0^2), \tag{8.6}$$

where I_0 is the intensity on the axis, and r is the radial coordinate. The beam waist ω_0 is the radius of the beam at the $1/e^2$ -point. For a beam truncated by a centered circular aperture with radius R, the power P is given by:

$$P = \int_0^R 2\pi I_0 \exp(-2r^2/\omega_0^2) r dr, \tag{8.7}$$

yielding:

$$P = P_{total}(1 - \exp(-2R^2/\omega_0^2)), \tag{8.8}$$

with P_{total} the power of the full Gaussian beam. The fraction A of the total beam power that enters through the lens aperture is therefore:

$$A = 1 - \exp(-2R_o^2/\omega_0^2), \tag{8.9}$$

with R_o the radius of the opening at the back of the objective.

In an optical tweezers setup, the trapping laser enters at the back of the objective. Inside, the light is focused onto the back aperture at the back focal plane (BFP), to be then further focused inside the sample. This back aperture is known as the exit pupil (EP) with radius R_{EP}, and the beam entering the objective is focused onto it by a factor of, approximately, R_{EP}/R_o. The beam at the EP will have a beam waist ω_{EP} given by:

$$\omega_{EP} = (R_{EP}/R_o)\omega_0, \tag{8.10}$$

and for 8.9 we can now write:

$$A = 1 - \exp(-2R_{EP}^2/\omega_{EP}^2). \tag{8.11}$$

The radius R_{EP} is given by:

$$R_{EP} = \mathrm{NA} f, \tag{8.12}$$

in which the focal length f is the ratio of the reference focal length, or tube length, L to the magnification of the microscope objective M:

$$f = L/M, \tag{8.13}$$

while the numerical aperture NA can be written as:

$$\mathrm{NA} = n_m \sin\theta_0, \tag{8.14}$$

where n_m is the refractive index of the medium, and θ_0 is the opening angle of the focused beam. This gives for Eq. (8.11):

$$A = 1 - \exp(-2(n_m(L/M)/\omega_{EP})^2 \sin^2\theta_0). \tag{8.15}$$

Comparing this to the relation given by Neto *et al.*:

$$A_{Neto} = 1 - \exp(-2\gamma^2 \sin^2\theta_0), \tag{8.16}$$

we find for γ:

$$\gamma = n_m(L/M)/\omega_{EP}. \tag{8.17}$$

Thus, for γ, defined by Neto *et al.* as "the ratio of the objective focal length to the beam waist", it should be noted that the focal length is $n_m L/M$, and that the beam waist is defined at the position of the EP.
Combining Eqs. (8.10), (8.12), (8.13), and (8.17), we can write:

$$\gamma = (n_m R_o)/(\mathrm{NA}\omega_0). \tag{8.18}$$

From Eq. 8.18, we see that not only the NA of the objective influences γ, and thus the trapping efficiency, but also the radius R_o of the opening at the back of the objective. To illustrate this, we look at the calculated trapping efficiency Q for silica core-shell particles, with a 772-nm-diameter PS core ($n_p = 1.6$, size parameter β is 3.305) in a medium with $n_m = 1.45$ [37]. For four objectives (see Table 8.2), we calculate γ and θ_0 for a fixed beam width ω_0, and use this to determine the axial trapping efficiency Q. This is done for a Leica DM IRB microscope, which has a reference focal length L of 200 mm. In Figure 8.6 the axial trapping efficiency is plotted for all four objectives. We see that even for the two 1.4-NA objectives, the efficiency differs, and that for the 63× objective, the trap stiffness κ is a factor 0.75 that of the 100× objective.

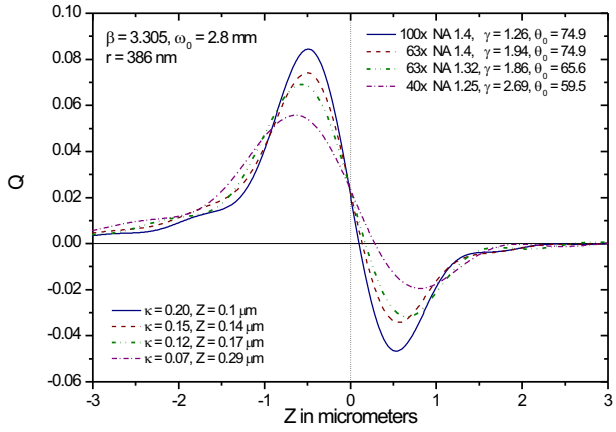

Fig. 8.6: Graphs

When the NA of an objective exceeds the refractive index of the medium (NA $> n_m$), the outer rays, will undergo total internal reflection (see also Section 3). This has to be taken in consideration when applying Eqs. (8.14) and (8.18). Merely taking NA $= n_m$ will not be representative for the rays in the specimen. In these cases, the focus is distorted by spherical aberrations — which are not taken into account by Mazolli *et al.* [25] — and an approximation of the NA should be made when applying the theory.

Tab. 8.2: Calculated γ and θ_0 for the oil immersion objectives used, with L=200 mm, fixed beam width ω_0=2.8 and n_m=1.45, for given NA, M, calculated R_{EP}, and measured R_o.

Objective	*NA*	*M*	R_{EP}	R_o	γ	θ_0
PL APO 100× 1.40 – 0.7	1.4	100×	2.80	3.4	1.26	74.9
PL APO 63× 1.40	1.4	63×	4.44	5.25	1.94	74.9
HCX PL APO 63× 1.32 – 0.6	1.32	63×	4.19	4.75	1.86	65.6
HCX PL APO 40× 1.25 – 0.75	1.25	40×	6.25	6.5	2.69	59.5

BIBLIOGRAPHY

[1] D. G. Grier. Optical tweezers in colloid and interface science. *Curr. Opin. Colloid Interface Sci.*, 2:264–270, 1997.

[2] A. R. Clapp and R. B. Dickinson. Direct measurement of static and dynamic forces between a colloidal particle and a flat surface using a single-beam gradient optical trap and evanescent wave light scattering. *Langmuir*, 17(7):2182–2191, 2001.

[3] D. G. Grier. A revolution in optical manipulation. *Nature*, 424:810–816, 2003.

[4] M. D. Wang, H. Yin, R. Landick, J. Gelles, and S. M. Block. Stretching DNA with optical tweezers. *Biophys. J.*, 72(3):1335–1346, 1997.

[5] J. W. J. Kerssemakers, M. E. Janson, A. van der Horst, and M. Dogterom. Optical trap setup for measuring microtubule pushing forces. *Appl. Phys. Lett.*, 83(21):4441–4443, 2003.

[6] A. Ashkin, K. Schütze, J. M. Dziedzic, U. Euteneuer, and M. Schliwa. Force generation of organelle transport measured in vivo by an infrared laser trap. *Nature*, 348:346–348, 1990.

[7] K. Svoboda, C. F. Schmidt, B. J. Schnapp, and S. M. Block. Direct observation of kinesin stepping by optical trapping interferometry. *Nature*, 365:721–727, 1993.

[8] M. J. Lang and S. M. Block. Laser-based optical tweezers. *Am. J. Phys.*, 71(3):201–215, 2003.

[9] K. C. Neuman and S. M. Block. Optical trapping. *Rev. Sci. Instrum.*, 75(9):2787–2809, 2004.

[10] A. Ashkin. Observation of a single-beam gradient force optical trap for dielectric particles. *Opt. Lett.*, 11(5):288–290, 1986.

[11] W. Grange, S. Husale, H.-J. Güntherodt, and M. Hegner. Optical tweezers system measuring the change in light momentum flux. *Rev. Sci. Instrum.*, 73(6):2308–2316, 2002.

[12] S. B. Smith, Y. Cui, and C. Bustamante. Optical-trap force transducer that operates by direct measurement of light momentum. *Methods in Enzymology*, 361:134–162, 2003.

[13] A. Ashkin. Forces of a single-beam gradient laser trap on a dielectric sphere in the ray optics regime. *Biophys. J.*, 61(2):569–582, 1992.

[14] W. H. Wright, G. J. Sonek, and M. W. Berns. Parametric study of the forces on microspheres held by optical tweezers. *Appl. Opt.*, 33(9):1735–1748, 1994.

[15] T. Wohland, A. Rosin, and E. H. K. Stelzer. Theoretical determination of the influence of the polarization on forces exerted by optical tweezers. *Optik*, 102(4):181–190, 1996.

[16] R. Gussgard, T. Lindmo, and I. Brevik. Calculation of the trapping force in a strongly focused laser beam. *J. Opt. Soc. Am. B*, 9(10):1922–1930, 1992.

[17] R. C. Gauthier and M. Ashman. Simulated dynamic behavior of single and multiple spheres in the trap region of focused laser beams. *Appl. Opt.*, 37(27):6421–

6431, 1998.

[18] P. C. Chaumet and M. Nieto-Vesperinas. Time-averaged total force on a dipolar sphere in an electromagnetic field. *Opt. Lett.*, 25(15):1065–1067, 2000.

[19] Y. Harada and T. Asakura. Radiation forces on a dielectric sphere in the Rayleigh scattering regime. *Opt. Commun.*, 124:529–541, 1996.

[20] J. A. Lock. Calculation of the radiation trapping force for laser tweezers by use of generalized Lorenz-Mie theory. I. Localized model description of an on-axis tightly focused laser beam with spherical aberration. *Appl. Opt.*, 43(12):2532–2544, 2004.

[21] J. A. Lock. Calculation of the radiation trapping force for laser tweezers by use of generalized Lorenz-Mie theory. II. On-axis trapping force. *Appl. Opt.*, 43(12):2545–2554, 2004.

[22] A. Rohrbach and E. H. K. Stelzer. Optical trapping of dielectric particles in arbitrary fields. *J. Opt. Soc. Am. A*, 18(4):839–853, 2001.

[23] A. Rohrbach and E. H. K. Stelzer. Trapping forces, force constants, and potential depths for dielectric spheres in the presence of spherical aberrations. *Appl. Opt.*, 41(13):2494–2507, 2002.

[24] P. A. Maia Neto and H. M. Nussenzveig. Theory of optical tweezers. *Europhys. Lett.*, 50(5):702–708, 2000.

[25] A. Mazolli, P. A. Maia Neto, and H. M. Nussenzveig. Theory of trapping forces in optical tweezers. *Proc. R. Soc. Lond. A*, 459:3021–3041, 2003.

[26] A. Rohrbach. Stiffness of optical traps: Quantitative agreement between experiment and electromagnetic theory. *Phys. Rev. Lett.*, 95(16):168102, 2005.

[27] N. B. Viana, M. S. Rocha, O. N. Mesquita, A. Mazolli, and P. A. Maia Neto. Characterization of objective transmittance for optical tweezers. *Appl. Opt.*, 45(18):4263–4269, 2006.

[28] M. W. Allersma, F. Gittes, M. J. deCastro, R. J. Stewart, and C. F. Schmidt. Two-dimensional tracking of ncd motility by back focal plane interferometry. *Biophys. J.*, 74:1074–1085, 1998.

[29] E. J. G. Peterman, M. A. van Dijk, L. C. Kapitein, and C. F. Schmidt. Extending the bandwidth of optical-tweezers interferometry. *Rev. Sci. Instrum.*, 74(7):3246–3249, 2003.

[30] S. Eiden-Assmann, J. Widoniak, and G. Maret. Synthesis and characterization of porous and nonporous monodisperse colloidal tio_2 particles. *Chem. Mater.*, 16(1):6–11, 2004.

[31] A. van Blaaderen and A. Vrij. Synthesis and characterization of colloidal dispersions of fluorescent, monodisperse silica spheres. *Langmuir*, 8(12):2921–2931, 1992.

[32] N. A. M. Verhaegh and A. van Blaaderen. Dispersions of rhodamine-labeled silica spheres: synthesis, characterization, and fluorescence confocal scanning laser microscopy. *Langmuir*, 10(5):1427–1438, 1994.

[33] H. Giesche. Synthesis of monodispersed silica powders II. Controlled growth reaction and continuous production process. *J. Eur. Ceram. Soc.*, 14(3):205–214, 1994.

[34] P. M. Hansen, V. K. Bhatia, N. Harrit, and L. Oddershede. Expanding the optical trapping range of gold nanoparticles. *Nanoletters*, 5(10):1937–1942, 2005.

[35] Y. Seol, A. E. Carpenter, and T. T. Perkins. Gold nanoparticles: enhanced optical trapping and sensitivity coupled with significant heating. *Opt. Lett.*, 31(16):2429–2431, 2006.

[36] N. R. Barbeau. Power deposited by a Gaussian beam on a decentered circular aperture. *Applied Optics*, 34(28):6443–6445, 1995.

[37] D. L. J. Vossen, A. van der Horst, M. Dogterom, and A. van Blaaderen. Optical tweezers and confocal microscopy for simultaneous three-dimensional manipulation and imaging in concentrated colloidal dispersions. *Rev. Sci. Instrum.*, 75(9):2960–2970, 2004.

SUMMARY

This thesis deals with various aspects of the optical trapping of high-refractive index particles. With a tightly-focused single-beam laser trap, also called *optical tweezers*, particles of a few nanometers up to several micrometers in size can be trapped and manipulated. The size and refractive index of such colloidal particles are of influence on the optical forces exerted on them in the trap. A higher refractive-index difference between a particle and the surrounding medium will increase the forces. The destabilizing *scattering force*, however, increases more than the *gradient force*. As a consequence, particles with a certain refractive index cannot be trapped in a single-beam gradient trap, and a limit is set to the force that can be exerted.

We demonstrated an experimental setup with two opposing high-numerical aperture objectives. By splitting the laser beam, we created counter-propagating tweezers in which the *scattering forces* in the axial direction were canceled and high-refractive index and metallic particles could be trapped. In Chapter 4 of this thesis, we used the counter-propagating trapping to pattern surfaces with high-refractive index particles. The sample cell was mounted on a high-accuracy piezo stage combined with a long-range stage and motorized actuators. Because we used microscopy image analysis of the patterned structure to accurately find back the starting position and compensate for drift of the sample, we could move far away from the patterning region. This enabled us to select particles from a separate reservoir of a mixture of (high-index) particles, and, one-by-one, position them at the chosen locations.

In Chapter 5, we created multiple counter-propagating traps by time-sharing the laser beam using acousto-optic deflectors. We trapped an array of high-refractive index particles, and by changing the positions addressed by the acousto-optic deflectors, were able to move those particles individually. In Chapter 6, such a dynamic array of counter-propagating tweezers was used to trap high-refractive index ZnO nanorods in three dimensions. The rods could not be held in single-beam line-tweezers. We demonstrate full translational and in-plane rotational control over the rods. The manipulation of such semi-conducting nanowires can be used to pattern surfaces and create more complex structures.

The forces exterted with counter-propagating tweezers are further investigated in the Chapters 7 and 8. In Chapter 7, a setup is presented in which counter-propagating trapping with two high-numerical aperture objectives was

combined with quadrant photodiode position detection. This enabled force measurements employing high-index particles, and the use of a separate laser beam for detection made position detection on particles in time-shared optical traps possible. The enhancement of trap stiffness that can be expected for the use of high-index particles was demonstrated and calculated in Chapter 8. Partial-wave Lorenz-Mie expansion calculations were used to calculate the forces in three dimensions on particles in the tightly-focused Gaussian laser beam.

In addition to counter-propagating trapping, we demonstrate the use of two opposing high-numerical aperture objectives to combine trapping of particles with the upright objective with simultaneous 3D fluorescent confocal imaging using the inverted objective. Particles with a high-index core were trapped inside a bulk of index-matched particles to induce colloidal crystallization. The effects of the trapped structure on the surrounding particles were imaged in 3D. When there is a mismatch in the refractive index between the objective immersion fluid and the medium in which we trap, the laser focus is distorted. In Chapter 3 we look at the origin of these spherical aberrations, and discuss the consequences for both trapping and imaging.

SAMENVATTING

Licht is in staat om een kracht uit te oefenen. Als er een verschil in brekingsindex is tussen een deeltje en het medium eromheen – bijvoorbeeld voor een glasbolletje in water – dan worden de lichtstralen die door het bolletje heen gaan afgebogen. Met dit afbuigen zijn krachten gemoeid: het deeltje oefent een kracht uit op de lichtstralen, en de lichtstralen oefenen een kracht uit op het deeltje.

In 1969 realiseerde Arthur Ashkin zich dat de kracht die een enkel lichtdeeltje – een foton – uitoefent heel klein is, maar dat met een laserbundel de kracht van alle fotonen samen groot genoeg kan zijn om een klein deeltje vast te pakken. In 1970 liet hij zien dat dit inderdaad het geval is, onder andere door met twee laserbundels kleine waterdruppeltjes in de lucht beet te pakken. In 1986 gebruikten Ashkin en collega's voor het eerst een enkele, sterk gefocuseerde laserbundel om deeltjes van enkele nanometers tot een paar micrometer groot te manipuleren, en dit is wat we nu *optical tweezers*, een optisch pincet, of een *optical trap*, een optische val, noemen.

Als de brekingsindex van een deeltje groter is dan die van het omringende medium, dan wordt het deeltje door de zogenoemde *gradient*-kracht altijd in de richting geduwd waar de intensiteit van het licht hoger is. In een sterk gefocuseerde laserbundel in een microscoop ondervindt een dergelijk deeltje dus altijd een kracht gericht naar het focus van de laser, omdat daar de intensiteit hoger is. De kracht ten gevolge van de verstrooiing van het licht duwt het deeltje echter vooral in de richting die het licht van de laserbundel opgaat.

Voor een groter verschil in brekingsindex tussen het deeltje en het omringende medium zijn ook deze optische krachten groter. De destabiliserende *verstrooiings*-kracht wordt echter sneller groter dan de *gradient*-kracht, wat maakt dat deeltjes met een bepaalde grootte en brekingsindex niet kunnen worden gevangen met een enkele laserbundel. Als een gevolg hiervan is er ook een limiet aan de kracht die met de laserbundel kan worden uitgeoefend.

In dit proefschrift worden verschillende aspecten van het vastpakken van hoge-brekingsindex-deeltjes behandeld. Wij demonstreren een experimentele opstelling waarin twee microscoopobjectieven tegenover elkaar zijn geplaatst. Door de laserbundel te splitsen pakken we de deeltjes van twee kanten vast en worden de verstrooiingskrachten in de richting van de bundel opgeheven. Op deze wijze konden ook deeltjes met een hoge brekingsindex en metaaldeeltjes

worden vastgehouden.

In Hoofdstuk 4 van dit proefschrift hebben we dit vasthouden met twee tegengesteldgerichte bundels gebruikt om patronen op oppervlakken te maken met deeltjes met een hoge brekingsindex. Het monster was vastgemaakt op een piezo-translatietafel, voor verplaatsingen met een hoge nauwkeurigheid, terwijl een tweede tafel met motors werd gebruikt voor de verplaatsingen over langere afstand. Doordat we het microscoopbeeld gebruikten om heel nauwkeurig de beginpositie terug te vinden konden we het monster over grote afstanden vanaf de positie waar we plakten verplaatsen. Hierdoor konden we deeltjes selecteren uit een verzameling van verschillende deeltjes, en ze een voor een op de gekozen posities plaatsen.

In Hoofdstuk 5, hebben we meerdere optische vallen van twee kanten gemaakt door de laserbundel in de tijd te verdelen met behulp van acoustisch-optische deflectoren. We hebben een reeks van deeltjes met een hoge brekingsindex vastgehouden en deze deeltjes ten opzichte van elkaar verplaatst. In Hoofdstuk 6 werd een dergelijke dynamische reeks van optische vallen gebruikt om een zinkoxide staafje met een hoge brekingsindex vast te houden in drie dimensies. Wij laten zien dat de staafjes op deze wijze kunnen worden verplaatst in alle richtingen en geroteerd in het focusvlak van het objectief. De staafjes konden niet worden vastgehouden met een laserbundel van een kant. De manipulatie van halfgeleider nanodraden kan worden gebruikt om patronen op oppervlakken en complexere structuren te maken.

De krachten die worden uitgeoefend met een optisch pincet van twee kanten worden verder onderzocht in de Hoofdstukken 7 en 8. In Hoofdstuk 7 presenteren we een opstelling waar we het vasthouden van twee kanten combineren met positiedetectie met behulp van een kwadranten-fotodiode. Hiermee kon de positie van deeltjes met een hoge brekingsindex worden bepaald. Doordat we een aparte laser gebruikten voor de positiebepaling kon dit gecombineerd worden met het in de tijd verdelen van de laserbundel van het pincet. De toename van de kracht die verwacht kan worden met het gebruik van deeltjes met een hoge index hebben we onderzocht en berekend in Hoofdstuk 8.

Behalve voor het vasthouden van deeltjes van twee kanten, hebben we de configuratie van twee objectieven tegenover elkaar ook gebruikt om met het bovenste objectief deeltjes vast te houden en tegelijkertijd met het andere objectief beelden op te nemen in drie dimensies met confocale fluorescentie microscopie. In Hoofdstuk 2 laten we zien dat deeltjes met een hoge-index kern konden worden vastgepakt in een verzameling van deeltjes waarvan de brekingsindex gelijk was aan die van de omringende vloeistof. Op deze laaste deeltjes werden geen optische krachten uitgeoefend omdat er geen verschil in brekingsindex was. De effecten van de vastgehouden deeltjes op de deeltjes eromheen konden worden afgebeeld in drie dimensies. Als er een verschil in brekingsindex is tussen de immersievloeistof van het objectief en het medium waarin we werken, dan wordt

het focus van de laserbundel verstoord. In Hoofdstuk 3 bekijken we de oorsprong van deze sferische aberraties en bespreken we de gevolgen hiervan voor het afbeelden en voor het vasthouden van deeltjes met een laserbundel.

DANKWOORD

In the years working as a PhD student, many people have contributed to my work and well being. De Soft Condensed Matter groep in Utrecht, de Bio-Assembly and Organization groep op AMOLF, en zeker ook AMOLF als instituut hebben een prettige werkomgeving gevormd. Het kunnen doen van mijn werk in twee verschillende groepen aan twee verschillende instituten heeft veel toegevoegd, en ik wil Marileen en Alfons bedanken voor deze mogelijkheid en voor de begeleiding van mijn promotieonderzoek. Het vertrouwen dat ik gekregen heb heeft geleid tot dit proefschrift, en ik heb ondervonden dat er niets gaat boven een combinatie van enthousiasme en nuchterheid, boven zelf laten doen gecombineerd met nooit te beroerd om in het lab te komen kijken hoe goed (of hoe niet) iets werkt en waarom. Dank.

Koen, het was erg goed om de eerste vier maanden bij jou in het lab door te brengen. Dank daarvoor, en ook voor de kopjes koffie in Tucson in de jaren daarna!

Veel dank ook aan mijn twee grootste mede-*optical trappers*: Dirk en Gertjan. Dirk, het waren goede tijden met IEP! Gertjan, het was heel prettig werken, en ik heb alle vertrouwen in de volgende stappen die je met MADELIEF gaat maken!

De meeste tijd heb ik in Utrecht doorgebracht, in a very nice group of people to work with! Yu Ling and Dannis, het was erg prettig en gezellig om met jullie een kamer te delen. Mirjam, Didi, Yu Ling, Job, Maria, en alle anderen van de groep, het was leuk! Andy, thank you for the many many hours trying to make things stick or not stick, depending on the surface. Verder wil ik Peter bedanken voor het doen van de vele berekeningen, en Hans voor de technische ondersteuning. Peter, zorg goed voor IEP!

Op AMOLF wil ik iedereen bedanken van de tekenkamer, de bibliotheek, het magazijn, de receptie, E&I, de kantine, etcetera. Een heel fijn instituut! Speciaal bedankt: Dirkjan voor de vele tekeningen, de mensen van de werkplaats voor alle onderdelen, en Johan voor de vele programma's, programmaonderdelen en aanpassingen op programma's. Bela, dank voor de inspirerende gesprekken.

Inspiratie vond ik zeker ook bij Marco. Marco, de jaren bij het NKI waren een goede, en leuke, aanloop voor me, en ik wil je bedanken voor alle steun die je me in de afgelopen jaren gegeven hebt!

Iris en Jac, hoe zouden de afgelopen jaren er zonder jullie twee er hebben

uitgezien? (Saai!) Dank voor de gesprekken, het voor me koken, het lezen, de steun en het toeverlaat zijn. Altijd heel erg fijn!

Ik wil met name ook bedanken: Roeland, Sijo, Nicolette, Beata, Mariette, en in het algemeen: alle vrienden die mij na het afgelopen jaar nog in hun agenda hebben staan. Dank voor de steun en oppeppende woorden.

En naturlijk mijn familie: Sander, Natalie, Ivo en Lieke, en mijn ouders, die me altijd mijn eigen weg hebben laten gaan en me daarin steunden.

And then, of course, Tesa, thank you for all the reading and listening, the good times and support. You have been truly great!

CURRICULUM VITAE

Astrid van der Horst werd geboren in Amsterdam, op 30 maart 1972. Na het behalen van het VWO diploma in 1990 te Venlo, en twee jaar studie aan de Technische Universiteit Delft, studeerde zij vier jaar aan de Hogere Technische School (HTS) in Rijswijk. Deze studie omvatte stages bij het FOM-Nationaal Instituut voor Kernfysica en Hoge Energie Fysica (NIKHEF), het Rotterdamse kankerinstituut Daniel den Hoed Kliniek, en het Kamerlingh Onnes Laboratorium van de Universiteit Leiden.

Na het behalen van de graad van natuurkundig ingenieur in 1996, begon Astrid met haar baan als onderzoeksmedewerker op de afdeling radiotherapie van het Nederlandse Kanker Instituut/Antoni van Leeuwenhoekhuis (NKI-AvL) in Amsterdam. Van 1999 to 2001 werkte ze als onderzoekstechnicus in het FOM-Instituut voor Atoom en Molecuul Fysica (AMOLF) in Amsterdam. In 2001 vormde een periode van vier maanden in het lab van Koen Visscher aan de University of Arizona het begin van Astrid's promotie. Haar promotiewerk heeft Astrid gedaan in twee groepen – de *Bio-assembly and Organization* groep van Marileen Dogterom op AMOLF en de *Soft Condensed Matter* groep van Alfons van Blaaderen aan de Universiteit van Utrecht.

Na het behalen van haar graad van doctor zal Astrid als postdoctoraal onderzoeker werken aan de Simon Fraser University in Vancouver, Canada. Haar interesses omvatten *optical tweezers*, krachtmetingen, en de biofysische toepassingen hiervan.

Astrid van der Horst was born in Amsterdam on the 30th of March in 1972. After obtaining her high school diploma in 1990 in Venlo, and two years of study at the Technical University Delft, she studied at the Technical School in Rijswijk. The study included work periods at the FOM-National Institute for Nuclear Physics and High-Energy Physics (NIKHEF), the Daniel den Hoed Cancer Institute in Rotterdam, and the Kamerlingh Onnes Laboratory at Leiden University.

After obtaining her Bachelor degree as an engineer in physics in 1996, Astrid began working as a research assistent at the Radiotherapy department of the Netherlands Cancer Institute - Antoni van Leeuwenhoek Hospital (NKI-AvL) in Amsterdam. Between 1999 and 2001, she worked at the FOM-Institute for Atomic and Molecular Physics (AMOLF) as a research technician. In 2001, after beginning her Ph.D. program at AMOLF in two groups – Bio-assembly and Organization *at AMOLF headed up by Marileen Dogterom and* Soft Condensed Matter *at Utrecht University lead by Alfons van Blaaderen – she spent a four month period in the United States at the University of Arizona in Koen Visscher's lab.*

Upon receiving her Ph.D., Astrid will work as a post-doctoral fellow at the Simon Fraser University in Vancouver, Canada. Her research interests include optical tweezers, force measurements, and their biophysical applications.

LIST OF PUBLICATIONS

Publications related to the work in this thesis

A. van der Horst, *et al.* **Forces exerted on high-refractive index particles in counter-propagating optical tweezers — Measurements and calculations**, in preparation (Chapter 8)

A. van der Horst, *et al.* **Three-dimensional optical trapping and manipulation of high-refractive index nanorods in line optical tweezers**, in preparation (Chapter 6)

A. van der Horst, A. Moroz, A. van Blaaderen, and M. Dogterom. **Dynamic arrays of high-refractive index particles trapped using dual-beam optical tweezers**, to be resubmitted (Chapter 5 and 8)

A. van der Horst, D.L.J. Vossen, K. Visscher, M. Dogterom, and A. van Blaaderen. **Manipulation and imaging of particles with optical tweezers and confocal microscopy**, Microscopy and Analysis, 19(2): 15–17 (UK), 2005

D.L.J. Vossen*, A. van der Horst*, M. Dogterom, and A. van Blaaderen. **Optical tweezers and confocal microscopy for simultaneous three-dimensional manipulation and imaging in concentrated colloidal dispersions**, Review of Scientific Instruments, 75(9): 2960–2970, 2004 (Chapter 2),
* these authors contributed equally to this work

J.W.J. Kerssemakers, M.E. Janson, A. van der Horst, and M. Dogterom. **Optical trap setup for measuring microtubule pushing forces**, Applied Physics Letters, 83(21): 4441–4443, 2003

A. van Blaaderen, J.P. Hoogenboom, D.L.J. Vossen, A. Yethiraj, A. van der Horst, K. Visscher, and M. Dogterom. **Colloidal epitaxy: Playing with the boundary conditions of colloidal crystallization**, Faraday Discussions, 123: 107–119, 2003

M. Dogterom, M.E. Janson, C. Faivre-Moskalenko, A. van der Horst, J.W.J. Kerssemakers, C. Tanase, and B.M. Mulder. **Force generation by polymerizing microtubules**, Applied Physics A - Materials Science and Processing, 75(2): 331–336, 2002

Other publications

L.J. Bos, C. Danciu, C.W. Cheng, M.J.P. Brugmans, A. van der Horst, A. Minken, and B.J. Mijnheer. **Interinstitutional variations of sensitometric curves of radiographic dosimetric films**, Medical Physics, 29(8): 1772–1780, 2002

E.M.F. Damen, M.J.P. Brugmans, A. van der Horst, L.J. Bos, J.V. Lebesque, B.J. Mijnheer, D.L. McShan, B.A. Fraass, and M.L. Kessler. **Planning, computer optimization, and dosimetric verification of a segmented irradiation technique for prostate cancer**, International Journal of Radiation Oncology Biology Physics, 49(4): 1183–1195, 2001

C.W. Hurkmans, J.H. Borger, L.J. Bos, A. van der Horst, B.R. Pieters, J.V. Lebesque, and B.J. Mijnheer. **Cardiac and lung complication probabilities after breast cancer irradiation**, Radiotherapy and Oncology, 55(2): 145–151, 2000

M.J.P. Brugmans, A. van der Horst, J.V. Lebesque, B.J. Mijnheer. **Beam intensity modulation to reduce the field sizes for conformal irradiation of lung tumors: A dosimetric study**, International Journal of Radiation Oncology Biology Physics, 43(4): 893–904, 1999

M.J.P. Brugmans, A. van der Horst, J.V. Lebesque, B.J. Mijnheer. **Dosimetric verification of the 95% isodose surface for a conformal irradiation technique**, International Journal of Radiation Oncology Biology Physics, 25(4): 424–434, 1998

The work presented in this thesis was performed in the following two research groups:

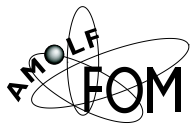

Bio-assembly and Organization
lead by prof. dr. Marileen Dogterom *

FOM-Institute for Atomic and Molecular Physics (AMOLF)
Kruislaan 407, 1098 SJ Amsterdam, the Netherlands

www.amolf.nl

* Prof. dr. Marileen Dogterom holds an affiliated professorship at Leiden University

Soft Condensed Matter
lead by prof. dr. Alfons van Blaaderen

Utrecht University
Princetonplein 1, 3584 CC Utrecht, the Netherlands

www.colloid.nl